AVERTISSEMENT

Ce document est le fruit d'un long travail approuvé par le jury de soutenance et mis à disposition de l'ensemble de la communauté universitaire élargie.

Il est soumis à la propriété intellectuelle de l'auteur. Ceci implique une obligation de citation et de référencement lors de l'utilisation de ce document.

D'autre part, toute contrefaçon, plagiat, reproduction illicite encourt une poursuite pénale.

Contact : ddoc-theses-contact@univ-lorraine.fr

LIENS

Code de la Propriété Intellectuelle. articles L 122. 4
Code de la Propriété Intellectuelle. articles L 335.2- L 335.10
http://www.cfcopies.com/V2/leg/leg_droi.php
http://www.culture.gouv.fr/culture/infos-pratiques/droits/protection.htm

UNIVERSITÉ DE LORRAINE

INSTITUT JEAN LAMOUR

CNRS

Thèse

présentée en vue de l'obtention du grade de

Docteur de l'Université de Lorraine

en Physique

par

Shuibao QI

soutenue le 25 octobre 2018

Métamatériaux et Métasurfaces Acoustiques pour la Collecte d'Energie

Composition du jury

Rapporteurs

M. Bahram Djafari-Rouhani	Professeur Emérite, Université de Lille
M. Vincent Tournat	Directeur de Recherches CNRS, Université du Maine

Examinateurs

Mme. Miso Kim	Professeur, Korea Research Institute of Standards and Science (Corée du Sud)
M. Nico Declercq	Professeur, Georgia Tech Lorraine
M. Jean-François Ganghoffer	Professeur, Université de Lorraine
M. Badreddine Assouar	Chargé de Recherches CNRS (Directeur de thèse)

Invité

M. Yong Li	Professeur de Recherches, Tongji University (Chine)

Institut Jean Lamour, UMR CNRS 7198
Campus Artem, 2 allée André Guinier, BP: 50840, 54011, Nancy Cedex, France.

Keywords: acoustic metamaterial, energy harvesting, acoustic waves, piezoelectric materials, acoustic metasurfaces

Mots clés : métamatériaux acoustique, la collecte d'energie, ondes acoustiques, matériaux piézoélectriques, métasurfaces acoustiques

I humbly and affectionately dedicate this work

to the memory of my father Mr. ***Yongkuan QI****,*

to my beloved mother, Mrs. ***Xiying YANG****,*
brothers, ***Yingxiong QI*** *and* ***Mubao QI****,*
sister, ***Xiaoyan QI****,*
nephews and nieces,

to all my friends.

Acoustic Metamaterials and Metasurfaces for Energy Harvesting

Abstract

Phononic crystals (PCs) and acoustic metamaterials (AMMs), well-known as artificially engineered materials, demonstrate anomalous properties and fascinating capabilities in various kinds of wave manipulations, which have breached the classical barriers and significantly broaden the horizon of the whole acoustics field. As a novel category of AMMs, acoustic metasurfaces share the functionalities of AMMs in exotic yet compelling wave tailoring. Inspired by these extraordinary capabilities, innovative concepts of scavenging acoustic energy with AMMs are primarily conceived and sufficiently explored in this thesis. Generally, a planar AMM acoustic energy harvesting (AEH) system and acoustic metasurfaces AEH systems are theoretically and numerically proposed and analyzed in this dissertation. At first, taking advantage of the properties of band gap and wave localization of defect mode, the AEH system based on planar AMM composed of a defected AMM and a structured piezoelectric material has been proposed and sufficiently analyzed. Secondly, subwavelength ($\lambda/8$) and ultrathin ($\lambda/15$) metasurfaces with various lateral configurations, composed of labyrinthine and Helmholtz-like elements, respectively, are designed and analyzed to effectively realize the acoustic focusing and AEH. This thesis provides new paradigms of AEH with AMMs and acoustic metasurfaces, which would contribute to the industries of micro electronic devices and noise abatement as well.

Keywords: acoustic metamaterial, energy harvesting, acoustic waves, piezoelectric materials, acoustic metasurfaces

Métamatériaux et Métasurfaces Acoustiques pour la Collecte d'Energie

Résumé

Artificiels structurés, présentent des propriétés inédites et des aptitudes uniques pour la manipulation d'ondes en général. L'avènement de ces nouveaux matériaux a permis de dépasser les limites classiques dans tout le domaine de l'acoustique-physique, et d'élargir l'horizon des recherches fondamentales. Plus récemment, une nouvelle classe de structures artificielles, les métasurfaces acoustiques, présentant une valeur ajoutée par rapport aux métamatériaux, avec des avantages en termes de flexibilité, de finesse et de légèreté de structures, a émergé. Inspirés par ces propriétés et fonctionnalités sans précédent, des concepts innovants pour la collecte d'énergie acoustique avec ces deux types de structures artificielles ont été réalisés dans le cadre de cette thèse. Tout d'abord, nous avons développé un concept à base d'un métamatériau en plaque en se basant sur le de l'approche de bande interdite et des modes de défaut permis par le mécanisme de Bragg. Dans la deuxième partie de cette thèse, des métasurfaces d'épaisseur sublongueur d'onde et ultra-minces composées d'unités labyrinthiques ou de résonateurs de Helmholtz ont été conçues et étudiées pour s'atteler à la focalisation et au confinement de l'énergie acoustique. Cette thèse propose un nouveau paradigme de collecte d'énergie des ondes acoustiques à base des métamatériaux et métasurfaces. La collecte de cette énergie acoustique renouvelable, très abondante et actuellement perdue, pourrait particulièrement être utile pour l'industrie de l'aéronautique, de l'automobile, du spatial, de l'urbanisme.

Mots clés : métamatériaux acoustique, la collecte d'energie, ondes acoustiques, matériaux piézoélectriques, métasurfaces acoustiques

Institut Jean Lamour
Campus Artem, 2 allée André Guinier – BP: 50840 – 54011, Nancy Cedex – France

Acknowledgement

At first, I would like to express my sincere gratitude to my dissertation defense jury members, Prof. Bahram Djafari-Rouhani, Prof. Vincent Tournat, Prof. Miso Kim, Prof. Nico Declercq and Prof. Jean-François Ganghoffer, for the review of the manuscript and attendance to my defense. Their professional comments, suggestions and discussions ameliorate and perfect the manuscript overall.

In the next, I profoundly appreciate my respected advisor, Prof. Badreddine Assouar, for his helpful and rigorous supervision. His insightful science instinct, enthusiasm in research and professional discipline have greatly impressed me and he sets a very good example for me to follow. This dissertation cannot be completed without his professional guidance and continuous patience. As a supervisor, he guided me into a new research field and provided me the necessary chances to learn and try different ideas. As a friend, he shared me his research experience and provided constructive advice for my future career.

Moreover, I wholeheartedly acknowledge the group members, Dr. Yong Li, Dr. Oudich Mourad and Dr. Joo Huan Oh, for their warm-hearted assistances and meaningful discussions, which helped me out of the technical difficulties and inspired me for better ideas and solutions in research. Special thanks are given to Dr. Yong Li for his attendance to my defense. I am very glad to have chance to meet other researchers and students of the 405 group, Didier Rouxel, Omar Elmazria, etc. I appreciate their company and encouragement during these three years.

After that, I also would like to present my heartfelt appreciation to the friends I have met in Nancy, who make my life colorful and unforgettable in this cozy town. Special thanks are given to Jingjiao Liu, Sami Ghadfi, Longeron François, Yujie Zheng, etc., with whom I spent many pleasant moments. I want to bring my thanks to my close friends, Huidong Gao, Tianlu Chen, Eddie Lau, Zhuozhen Lu, Yun Yang, Shimin Huang, Yunfeng Liu, Xinshu Fu, Xinhui Liu, etc., for their continuous encouragement and kind wishes.

Finally, I would like to thank my family, especially my mother, for their unconditional love and full supports all the time, which are the endless power source for me to explore and appreciate the unknown and enchanting world.

Acronyms

A | B | D | E | F | G | H | I | L | M | O | P | Q | S | Z

A

AEH acoustic energy harvesting. 3
AMMs acoustic metamaterials. 2
AMSs acoustic metasurfaces. 3

B

BG band gap. 6

D

DMR decorated membrane resonator. 31

E

EAT extraordinary acoustic transmission. 7

F

FEM finite element method. 52
FWHM full width at half maximum. 114

G

GIM gradient-index metasurface. 28

H

HR Helmholtz resonator. 11
HWTR half wavelength tube resonator. 38

I

IoT internet of things. 1

L

LEM lumped element model. 37
LRPC locally resonant phononic crystal. 8

M

MEMS microelectromechanical system. 1

O

OAM orbital angular momentum. 28

P

PCs phononic crystals. 2
PML perfectly matched layer. 70
PT parity time. 13
PVDF Piezoelectric polyvinylidene fluoride. 38

Q

QWTR quarter wavelength tube resonator. 38

S

SD Schröeder diffuser. 24
SPL sound pressure level. 35
STL sound transmission loss. 44

Z

ZIM zero-index-metasurface. 28

Contents

List of Tables

List of Figures

General Introduction

Energy harvesting can be generally defined as gathering and transforming various forms of ambient energy such as sunlight, wind, hydro water, heat, mechanical vibration, biochemical effect, etc., into popular electrical energy, primarily. Medium to large scale hydropower plants, wind turbines, photovoltaic systems, geothermal harvesters are relatively mature and commercially available, which will be beyond our research scope in this dissertation. The micro to medium scale energy harvesting concepts and designs possible for powering miniature electronic systems, however, will be covered with details.

With the enormous advances and proliferation of microelectronic autonomous devices, such as wireless sensors, internet of things (IoT) and microelectromechanical system (MEMS), various kinds of innovative ambient energy harvesters, emerging recently to power these low power devices based on different mechanisms and applications, have intrigued increasing attention from academia to industry. These energy harvesting designs can be readily implemented into the standalone devices as alternative power supplies with long lifetimes and high reliability, thus potentially circumventing the traditional battery-related disadvantages, e.g., the requirements of periodical replacement or recharging, disposal issues, etc. Mechanical motion and vibration, solar radiation, man-made radio signals, thermal gradients, static electricity and other ambient energy sources abundantly exist in various environments, which are renewable, harvestable and otherwise wasted energy sources favorable for microelectronic devices due to their low power property. The solar and thermoelectric devices for energy harvesting are relatively mature and widely commercialized. Mechanical energy based power generation devices have made impressive progress and currently concentrated on the challenges of broadband, high conversion efficiency and

universally applicable implementations. Piezoelectric, electrostatic, electromagnetic and magnetostrictive conversion methods have been extensively explored and investigated to transform mechanical energy into electricity. Because of the high power density, almost unlimited lifetime, simple implementation, and well-established manufacturing techniques, piezoelectric based methods are extensively applied for vibration and motion energy harvesting. Nonlinear energy harvesters have been proposed recently to favor the scavenging of natural broadband mechanical motion and vibration. Other piezoelectric energy harvesting designs based on piezoelectric mono cantilever, bimorph, arrays and other structural configurations are widely investigated and facilitated for specific applications.

Even though the piezoelectric mechanical energy conversion method is vigorously advancing with a promising future, rather than further contribute to its development, this dissertation will lay emphasis on mechanical energy confinement and subsequently apply the currently mature and highly efficient piezoelectric models and designs to our energy harvesting systems for the mechanical to electrical energy conversion. As a kind of clean, ubiquitous and renewable form of mechanical energy, fluidic or structural acoustic waves may act as a promising sustainable power source for microelectronic devices due to the dual benefits of energy harvesting and noise abatement, simultaneously. Even though acoustic waves abundantly exist in industrial, public and domestic environments, sound energy generally needs to be confined or localized before it can be effectively harvested and converted into electric energy trough piezoelectric methods, due to its intrinsic drawback of low power density. Intuitively, classical Helmholtz and other chamber resonators have been applied to enhance the acoustic confinement and subsequently realize AEH. However, the strategy based on resonators suffers from the defects of the bulky structures and uncontrolled wave field, thus hampering the applicable energy harvesting.

In a drastically different context, innovative engineered materials, such as phononic crystals (PCs) and acoustic metamaterials (AMMs), emerging recently with rich physics and plenty of extraordinary capabilities in various wave manipulations, have intrigued compelling interest among scientists and engineers for all kinds of acoustic and elastic wave engineering applications. Metamaterial-

based acoustic wave manipulations show great potential in effective acoustic energy confinement and noise control. Based on the mechanisms of the Bragg scattering and local resonance, the acoustic band gaps (BGs) of PCs and AMMs could be tuned or designed to realize acoustic energy confinement and harvesting. As a novel branch of metamaterials, acoustic metasurfaces (AMSs) demonstrate sub-wavelength or ultrathin features, and thus possess additional capabilities and flexibilities in sound wave manipulations, which provide more degrees of freedom in AEH. As identified in the title of this thesis "Acoustic Metamaterials and Metasurfaces for Energy Harvesting", the main task of this dissertation will be focused on acoustic energy harvesting (AEH) with specific acoustic metamaterials and metasurfaces. Phononic metamaterials and acoustic metasurfaces based acoustic energy harvesting concepts and designs are separately reported and demonstrated in respective chapters.

The state of the art and literature review on acoustic metamaterials, metasurfaces, and elastic/acoustic energy harvesting are provided in Chap. 1. Because metamaterials and energy harvesting aspects are different fields containing numerous divisions, chapter 1 will review most relevant literatures on acoustic metamaterials favoring sound wave localization or confinement and on acoustic energy conversion designs, rather than exhaustively refer to all the literatures in the two fields. The implementation and results of AEH based on planar metasurface are initially presented in the dissertation. Chap. 2 mainly deals with stub-plate metamaterials for acoustic energy confinement. Theoretical and numerical AEH designs are elucidated from the aspects of structural and acoustic borne analysis. Acoustic energy conversion models based on piezoelectric methods are also introduced and discussed in Chap. 2. The design and demonstrations of AEH based on metasurfaces are composed of two chapters, i.e., Chap. 3 and Chap. 4. Labyrinthine metasurfaces based AEH systems are designed and demonstrated in Chap. 3. More specifically, based on the concept of coiling up space and generalized Snell's law, two-dimensional (2D) acoustic metasurfaces constructed by labyrinthine elements with various configurations for AEH are proposed and sufficiently explored. Helmholtz-like elements with thinner thickness based on locally resonant mechanism are designed and applied to construct the ultrathin acoustic metasurface in Chap. 4. Moreover, the pre-

viously proposed acoustic metasurfaces composed of labyrinthine elements for acoustic focusing are further extended from two-dimensional (2D) design into three-dimensional (3D) situation, and the results are compared with those of the ultrathin metasurface in the same chapter. In the chapter of general conclusion and perspective, the designs and results on AEH are reviewed and summarized, and related perspectives are discussed and outlooked on future research and applications.

Il faut avoir la qualité morale; il faut s'entendre franchement avec des autres; il faut avoir des comportements courtois.

Montesquieu

Chapter 1

State of the art

Contents

Acoustic metamaterials and phononic crystals for wave manipulations, and the design evolutions of acoustic energy harvesting (AEH) are sufficiently reviewed and presented in this chapter. Planar acoustic metamaterials and metasurfaces for wave guiding and localization are emphasized, and AEH based on various design concepts are demonstrated and discussed.

1.1 Metamaterials and metasurfaces

Metamaterials are artificial materials with unusual properties that are not readily available in naturally occurring materials. The prefix *meta* from Greek means beyond, and thus metamaterials implicit beyond conventional materials. Metamaterials are designed with composite materials to achieve desired effective

properties. Modern metamaterials were firstly proposed in the field of electromagnetism and optics. In 1968, Victor Veselago theoretically conceived[1] electromagnetic media with negative dielectric permittivity ϵ and magnetic permeability μ, which could enable special lenses due to negative refractive index. The hypothesized materials with negative ϵ and μ were realized by John Pendry and coworkers[2] thirty years later. Inspired by the pioneering work of Victor Veselago and John Pendry, plenty of metamaterials with various exotic capabilities unavailable from natural materials have been proposed, which contribute to the flourish of the classical wave fields.

1.1.1 Phononic crystals and acoustic metamaterials

Phononic crystals

Crystals are solid materials periodically constructed by constituent inclusions in a homogeneous matrix. In 1987, Yablonovitch and Sajeev John [3, 4] proposed the concepts of photonic crystals, which opened new horizon in light manipulations. The concept was introduced to the acoustic field[5], which contributed to the emergence of phononic crystals and their vigorous development[6, 7]. Similar and analogous to photonic crystals, phononic crystals are composed of periodically arrayed sound scatters (inclusions). Acoustic incident waves are interacted with the periodic sound atoms (sound scatters), and waves of specific frequencies and momenta can propagate in the periodic structure, while others are forbidden to transmit in the periodic structure. These phenomena are governed by the Bloch theorem, from which the energy band structure of the PCs in the corresponding Brillouin zone can be derived. The frequency bands that prohibit the sound wave propagation along one or more directions are referred to acoustic band gaps (ABGs). Figure 1 illustrates a simple example of 1D elastic PC and its wave propagation features. The band structure with an obvious band gap and the corresponding wave transmission class (TC) curve are shown in Fig. 1.1(a) and Fig. 1.1(b), respectively. The PC supports wave propagation beyond the BG (Fig. 1.1(c)), while forbids its propagation within the band gap (Fig. 1.1(d)). Phononic crystals can be periodically constructed in one (1D), two (2D) or three dimensions (3D), and the periodicity of the inclusions defines the

Brillouin zone. Absolute band gaps[8] mean that the wave with any polarization and any incident angle is forbidden to propagate in 1D to 3D PCs.

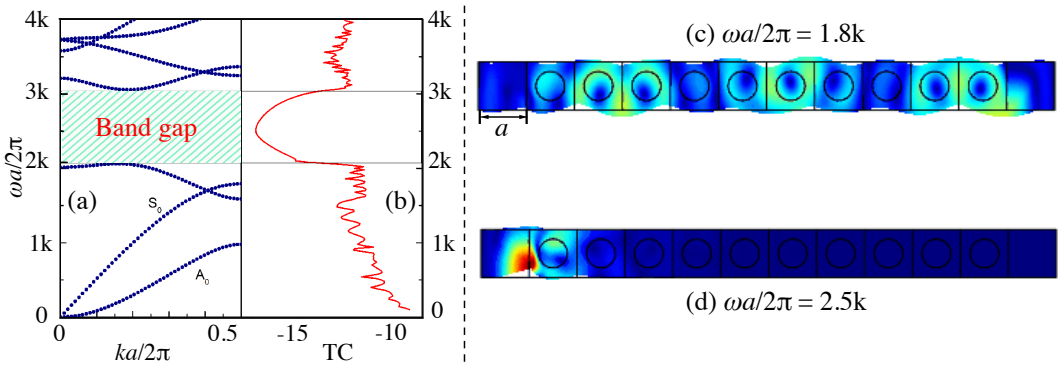

Figure 1.1 – A typical example of 1D PC and its band gap feature. (a) Band structure with a band gap. (b) Transmission class (TC). (c) and (d) are the mode shapes of wave propagation beyond (1.8k) and within (2.5k) the band gap.

Band gaps are one of the utmost important and classical features of PCs, and other desirable properties relevant with BGs could be acquired by introducing localized modes inside the BGs. The localized modes, also named defect modes, can be obtained by creating point or linear defect[9] such as cavities and waveguide lines inside the perfect PCs. The defect modes possess a decaying wave function away from the defects[10, 11], which enables the wave confinements and guiding in defected PCs. More specifically, these defects can be produced by removing or changing the inclusions of the PCs, according to the required imperfection shapes. Taking advantage of BGs and defect modes, PCs can be used to realize various wave manipulations such as wave isolation[12], confinement[13], guiding[13–15] and filtering[16, 17] at the level of wavelength. Besides the band gaps, wave propagations in the pass bands of PCs also exhibit compelling potentials in exotic wave manipulations, including extraordinary acoustic transmission (EAT)[18], negative refraction[19], and acoustic collimation[20]. The experimental isolation of graphene and realization of Dirac cones (two circular cones connected at their extremities) with linear dispersions shed light on the current development of PCs. Analogue to Zitterbewegung transport of acoustic waves, phononic graphene and Dirac-quasiparticle related behaviors were reported[21–23] recently. Similar to topology in photonics[24], the topological

phases of matter and geometry were transferred to realize and characterize the phonon conductivity within pass band of innovative phononic systems[25–27].

The phononic band structures and dispersion curves that dominate the acoustic behaviors of PCs are determined by the physical characteristics of the constituent materials (density and elastic constants) and geometrical parameters (crystal lattices, inclusions arrangements, shape and filling factor of inclusions)[28]. Generally, the opening of a BG is caused by the destructive interference of the scattered waves from the periodic inclusions. In ordinary PCs, according to the Bragg mechanism, the first BG occurs at a frequency about c/a, where c is sound velocity and a is the lattice constant (periodicity). Propagating waves of the matrix can be coupled with Localized modes of the inclusions to form a hybridization gap[29] and modify the band structures as well. Through coating the hard lead inclusions with soft rubber, spectral gaps with a lattice constant two orders of magnitude smaller than the relevant wavelength were achieved[30], which brought about the first locally resonant phononic crystal (LRPC). Based on local resonances, LRPCs go beyond the Bragg scattering limits of ordinary PCs and improve the efficiency for wave manipulations in low frequency bands. The introduction of local resonances in phononic media initiated the well-known acoustic metamaterials (AMMs) and witnessed the rapid subsequent development[31–36]. AMMs own the advantage of sub-wavelength property and are not necessarily periodical in constitution, which outperform classical PCs in smaller dimensions and additional degrees of freedom in acoustic/elastic wave manipulations.

Acoustic metamaterials

Acoustic metamaterials are artificially engineered materials with exotic yet fascinating features, e.g., negative properties (mass and bulk modulus), which could favor a series of desirable acoustic wave manipulations. Acoustic and electromagnetic waves share classical wave properties to some extent, and thus the concepts of metamaterials and photonic crystals in electromagnetic and optics fields can be analogously introduced in the realm of acoustics as acoustic metamaterials and phononic crystals. As counterparts of permittivity ϵ and

inverse of permeability μ^{-1} in acoustic field, the two fundamental parameters of acoustic metamaterials and phononic crystals that can influence acoustic wave propagations are effective density ρ_{eff} and bulk modulus κ_{eff}. The general understanding of these two parameters can be readily demonstrated in Fig. 1.2. As shown in Fig. 1.2(a), material with negative ρ_{eff} demonstrates that the acceleration $\boldsymbol{a}$ of the material is opposite to the exerting force $\boldsymbol{F}$. Bulk modulus κ depicts the compressibility of material and can be generally defined as[37]:

$$\kappa = -V\frac{\Delta p}{\Delta V}, \tag{1.1}$$

where p is pressure, V is volume, and $\Delta p/\Delta V$ denotes the change of pressure with respect to volume variation. For natural materials, the volume will be decreased when experiencing a positive pressure. Therefore, ΔV is negative, and thus κ renders positive. On the contrary, the volume of the material with negative effective bulk modulus κ_{eff} expands under the positively applied pressure, and the resulting volume difference $\Delta V = V_2 - V_1$ turns positive, which is illustrated in Fig. 1.2(b).

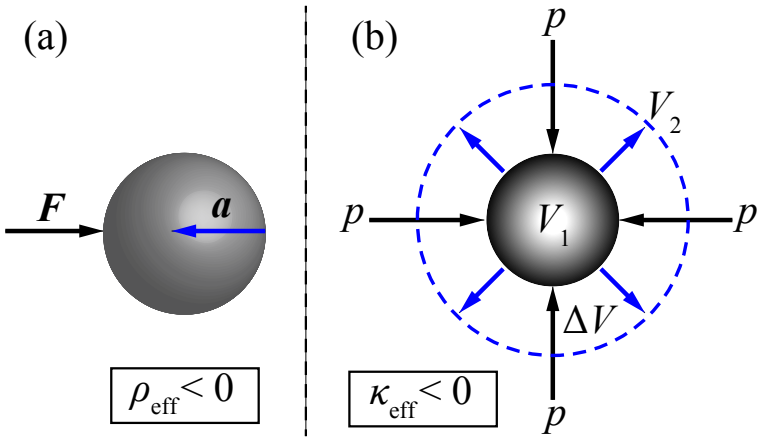

Figure 1.2 – Schematic illustration of negative effective (a) density and (b) bulk modulus.

The use of ρ_{eff} and κ_{eff}, rather than impedance of complex designs, greatly favors the development and interpretation of exotic properties of phononic crystals and acoustic metamaterials. Other essential acoustic variables and the

resulting phenomena could be closely correlated with these two parameters.

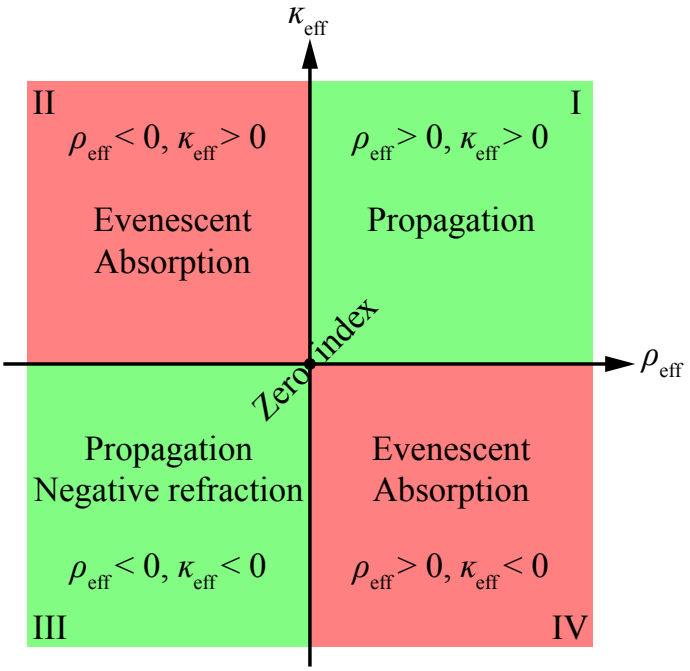

Figure 1.3 – Schematic illustration of negative effective (a) density and (b) bulk modulus.

Figure 1.3 briefly provides the acoustic behaviors of materials under four various ρ_{eff} and κ_{eff} combinations. In Fig. 1.3, Quad. I demonstrates naturally occurring materials, and Quands. II-IV the materials with negative properties. Considering the adiabatic process, the phase velocity v_p can be represented by ρ_{eff} and κ_{eff} as $v_p = \sqrt{\kappa_{eff}/\rho_{eff}}$. The phase velocity v_p would be imaginary if either quantity is negative (i.e., Quads. II and IV), which induces the exponential wave decay and forbids the transmission, resulting in the band gaps of PCs and AMMs. When both ρ_{eff} and κ_{eff} are negative (i.e., Quad. III), phase velocity v_p would regain real value, which underpins the wave propagation. While in this situation, phase and energy velocities propagate in opposite directions, which could lead to backward propagation and negative refraction. Materials with double-negative constitutive properties in Fig. 1.3 (Quad. III) are defined as negative index materials (NIMs). When both bulk modulus and mass density approach zero, i.e, zero index, the phase velocity become infinite, which makes

cloaking and unidirectional transmission possible[35]. Materials with negative parameters illustrated in Quads. II-IV of Fig. 1.3 have been theoretically and experimentally realized in the past decades.

The concepts of band folding effect[19], local resonance[30] and coiling up space[38] could be applied to achieve negative parameters of PCs and AMMs. Different from ordinary PCs with lattice constant comparable to the work wavelength, deep sub-wavelength AMM[30] with local resonance constructed by periodically arrayed hard inclusions coated with soft rubber in a 3D matrix (Fig. 1.4(a)) demonstrates the capability to break the classical mass law in sound isolation. Local resonances induced by AMMs can cause strong frequency dispersions of the dynamic mass density and bulk modulus of AMMs, which could lead to the effective negative values at the resonances. The AMM can be regarded as a spring-mass system, where the hard inclusion cores (mass) connect with the rigid matrix by the coated rubber (spring). In this system, the mass accelerates out of phase of the applying force on the matrix, i.e., the directions of acceleration and force are antiparallel, at the resonant frequencies, thus leading to the negative effective mass (Fig. 1.4(a)). This category of resonance is defined as dipolar resonance, which demonstrates asymmetric motions and controls the effective mass density[39]. Another locally resonant phononic system[40] constructed by metal plate deposited with rubber pillars demonstrated strong anisotropy of effective mass, and the negative mass density is acquired at the resonance frequencies of the opening of the band gaps. Tensioned membranes were served as the moving mass with negative inertia[41, 42] can be applied to realize dipolar resonances and negative mass. The dynamic mass density strongly disperse with positive and negative values, and the negative mass appears[42, 43] below the critical frequency.

Contrary to natural materials with positive compressibility, AMMs with negative modulus experience an expansion with positive applied pressure. The famous acoustic element, i.e., Helmholtz resonator (HR), could be a good candidate to realize negative bulk modulus, due to that its cavity serves as a dynamic volume source above the resonant frequency. The first AMM with negative bulk modulus was experimentally achieved with an array of Helmholtz resonators (HRs) connecting to a waveguide tube in series[44], which is illustrated in Fig.

1.4(c). Because of the coupled resonance of the HRs, the volume inside the waveguide channel oscillates out of phase with the pressure, thus giving rise to negative effective bulk modulus. Parallel to dipolar from the asymmetric compressive/expansive (breathing) motions for the effective mass density modulating, the mono-polar resonance induced by symmetric breathing motions contributes to the bulk modulus modulating. The design of rubber spheres suspended in water[39] can realize dynamic bulk modulus, and the rubber spheres could oscillate out of phase at the mono-polar resonant frequency, i.e., expand under compressive pressure and shrink under stretch pressure.

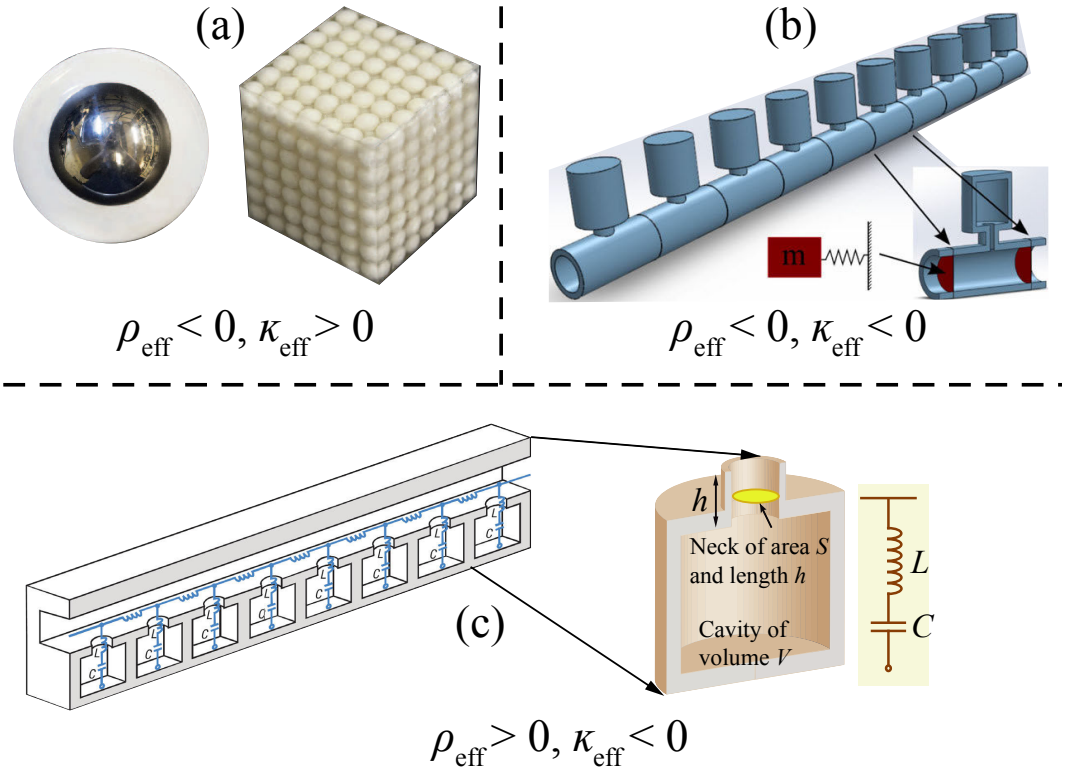

Figure 1.4 – Sketch illustration of several exemplary acoustic metamaterials with negative effective properties. (a) Negative density[30, 35]. (b) Negative bulk modulus and density[45, 46].(c) Negative bulk modulus[44].

Negative index materials can be achieved by combining individual structures with two different negative properties or one integrated material with both dipolar and mono-polar resonances within an overlapped range of resonant

frequencies. Helmholtz resonators with dynamic bulk modulus and membranes with dynamic mass are combined to construct a double-negative metamateial[45]. As illustrated in Fig. 1.4(b), HRs are connected to a waveguide channel to construct the negative index material. In Fig. 1.4(b), the orifice of the HRs could be controlled to obtain zero resonant frequency, and the mass between two HRs can be regarded as a mass constrained by a spring, which acts as a high pass filter[46]. Therefore, negative density and bulk modulus can be simultaneously achieved by properly selecting the resonance frequencies. Except the HRs and membrane structures based on the dipolar and mono-polar resonance mechanisms, the concept of coiling up space could also provide a means to acquire negative refraction index[38, 47]. Below the band gap of the coiling up space structure, there exists a frequency region where both negative effective mass density and bulk modulus can be achieved simultaneously. Both effective refraction index and impedance are dispersive in the frequency range, and thus increasing the relative refractive index by coiling up space alone could realize negative index, rather than overlap two different kinds of resonances to create double negativity[38]. Double negativities can provide negative refraction indexes, which are essential for super focusing, subwavelength or deep subwavelength lensing, and abnormal diffraction.

Metamaterials with negative properties have illustrated fascinating capabilities in unconventional wave manipulations, which enable various wave engineering applications. Beyond the negative properties, other research hotspots of acoustic metamaterials[34], such as transformation acoustics for cloaking[48–50] and acoustic illusion, active acoustic metamaterials for parity time (PT) symmetry[51–53] and nonreciprocity[54], and acoustic metasurfaces[55, 56] for device miniaturization and loss reduction, have also been being explored recently.

Acoustic transformations were priorly demonstrated by analogy with electromagnetics, and the specific coordinate transformation can be realized by creating a wide range of acoustic properties, like controllable inhomogeneity and anisotropy, of the media. Inertial and pentamode metafluids[57, 58] are two distinct materials to realize controllable anisotropy and inhomogeneity. Inertial metafluids possess single and scalar bulk modulus, yet a tensor density that leads to directionally varying material properties, i.e., anisotropy; pentamode

metafluids have decaying shear stiffness and thus a tensor bulk modulus, which contributes to spatially varying material properties, i.e., inhomogeneity. The acoustic transformation concept realized by these two kinds of metafluids can be applied to achieve complex wave manipulations, including acoustic cloaking. Inertial metafluids can be constructed by arranging solid inclusions in a host fluid. Experimental implementations of inertial metafluids for cloaking have been first reported due to the simple fabrications. Scatters are asymmetrically deposited in a natural fluid to yield anisotropic effective mass. The concept of metamaterials was applied to construct metafluids through creating meta-atoms with different properties required by transformation design process.

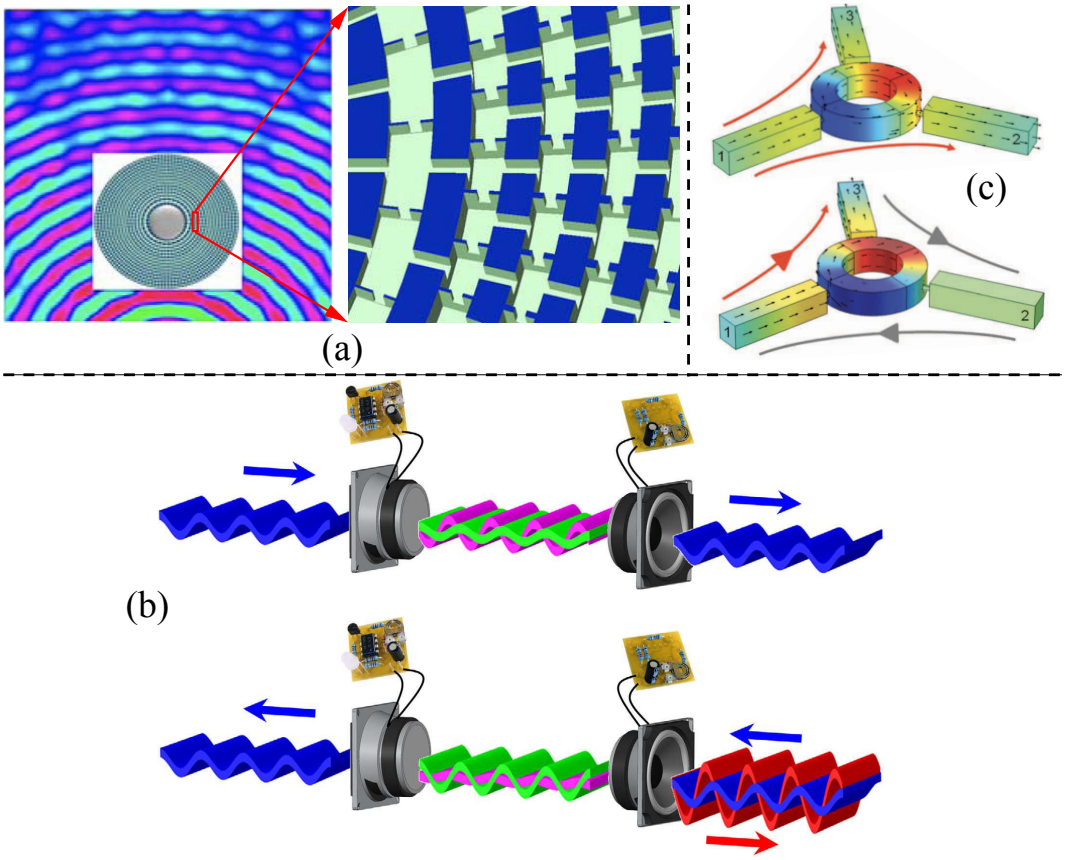

Figure 1.5 – Transformation and active acoustic metamaterials. (a) 2D cloak under water[48]. (b) A parity-time-symmetric invisible acoustic sensor[52]. (c) A non-reciprocal acoustic circulator[54].

A planar structure composed of a network of subwavelength cavities connected by narrow channels is immersed within a thin layer of water to experimentally construct the matefluid and realize acoustic cloaking in 2D situation[48], which is illustrated in Fig. 1.5(a). In addition to inertial metafluids, pentamode metafluids can be alternatively applied to design transformation acoustics devices with larger flexibilities. The pentamode metafluid constructed by interconnected microstructures[59, 60] with highly anisotropic bulk modulus have been reported to achieve acoustic cloaking. In addition to acoustic cloaking, the transformation acoustics can also be applied to achieve illusion acoustics for object concealing[61], and to realize bifunctional lenses[62] as well.

The concepts and applications of acoustic cloaking have intrigued the prospect of active acoustic metamaterials, which are the current research frontiers in the meta-field. Active, nonlinear, and parity-time properties of novel acoustic metamaterials could provide additional degrees of freedom in wave manipulations and facilitate their applicabilities in real situation. Most of the passive metamaterials aforementioned are frequency-dependent and based on various kinds of resonances, which unavoidably result in wave energy dissipation and thus reduce the overall efficiency. Active acoustic metamaterials with active components can be used to control the gain and loss. As one intriguing subset of active metamaterials, parity-time-symmetric acoustic metamaterial can tune the imaginary part of the refractive index by actively injecting or absorbing energy[52, 53]. As illustrated in Fig. 1.5(b) , one loudspeaker in the left is connected to an electric circuit with passive impedance to absorb impinging acoustic wave, and the second one connected to an active circuit to realize time-reversed[52] image of the left loudspeaker. This PT metamaterial element appears transparent without reflection or shadow when the acoustic incidence from the left side, while opaque with high reflection under the incidence from the right side[52], as shown in Fig. 1.5(b). Non-reciprocal acoustic metamaterials can be also a branch of active metamaterials. Wave propagation in conventional way is symmetrical and time reversible, which is reciprocity, a fundamental property for many wave phenomena. Exotic and special capabilities, such as unidirectional wave propagation, source isolation, etc., could be achieved by non-reciprocal metamaterials. One common method to break reciprocity of wave propagation is to introduce

moving fluid media[37]. As shown in Fig. 1.5(c), a sub-wavelength acoustic circulator with three waveguide ports was proposed to achieve non-reciprocity[54]. In Fig. 1.5(c), the resonant device is radially symmetric, and the input sound at port 1 splits equally into port 2 and 3 at the resonant frequency (see the upper subfigure) when the device is filled with a static medium. However, when filled with rotating air fluid, the acoustic waves from port 1 are routed to port 2 and isolated for port 3 over 40 dB, which breaks the symmetry in transmission, as shown in the lower subfigure of Fig. 1.5(c). Nonlinear effects can be also applied to realize non-reciprocity[63, 64]. These compact devices can be utilized as the meta-atoms to construct more complex topological metamaterials[34], which could provide new degrees of freedom in sound wave manipulations.

As a new research hotspot and a novel branch of acoustic metamaterial, acoustic metasurface has aroused broad attention recently, due to its planar (sub wavelength or deep sub-wavelength) property, easy fabrication, and flexibility in wave manipulations. Since acoustic metasurface is another focus of this dissertation, great details on acoustic metasurfaces will be introduced and discussed in the following section.

1.1.2 Acoustic metasurfaces

As 2D equivalents of metamaterials, metasurfaces with sub-wavelength thickness were originally named as metafilms or metascreens and initially proposed[65, 66] in eletromagnetic fields. Metasurfaces could replace metamaterials in many wave engineering applications due to their smaller and less lossy structures. Moreover, metasurfaces can achieve controllable smart surfaces and miniaturized cavity resonators for novel wave-guiding, compact and wide-angle absorption, impedance-matching, etc[67].

As illustrated in Fig. 1.6, artificial composite materials can be categorized into three regions according to their geometric sizes comparing with wave frequency or wavelength[67]. In Region (I), for the metasurfaces with 2D lattice of scatterers, wavelength is much larger than the periodicity of scatterers consisting the metasurfaces. Region (I) can be regarded as quasistatic region, and thus classical mixing formulas are used determine equivalent effective properties of

the media. In Region (II), when the wavelength decreases but still larger than the periodicity of the medium, the individual scatterers can resonate with proper designs. Metamateials and metasurfaces that take advantages of individual resonance of scatterers fall into Region (II). The wavelength further decreases to be comparable or smaller than the periodicity of the medium, and the medium can no longer be regarded as effective medium. Instead of local resonators, resonances with lattice periodicity play a role in Region (III), where Floquet-Bloch mode expansion approach is applied to analyze the propagating properties of the composite, which corresponds to the aforementioned photonic or phononic crystal.

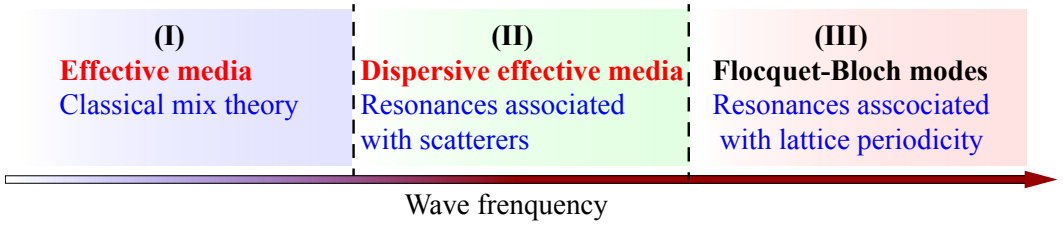

Figure 1.6 – Three characteristic regions for metamaterials[67].

With introducing Fresnel equations and generalizing Snell's law that govern wave propagation in the interface of two homogenous media, the pioneering work[68] has initiated an innovative and practical means to realize optical metasurfaces. Snell's law can be generalized to theoretically define the phase profile along the interface for desired wave reflection or refraction, and the prescribed phase profile could be subsequently discretized and realized by individual elements that could cover 0 - 2π phase shifts[68]. As shown in Fig. 1.6, the phase discontinuities along the interface can be achieved by artificially introducing additional phase distribution $\Phi(x)$ along the interface of two media, (I) and (II). Generalized Snell's law[68] for diffraction,

$$n_t \sin(\theta_t) - n_i \sin(\theta_i) = \frac{\lambda_0}{2\pi} \frac{d\Phi(x)}{dx} \tag{1.2}$$

and reflection,

$$\sin(\theta_r) - \sin(\theta_i) = \frac{\lambda_0}{2\pi n_i} \frac{d\Phi(x)}{dx} \tag{1.3}$$

can be deduced by applying Fermat's principle, where n_i, n_t, θ_i, θ_r, and θ_t are the refractive indexes of media (I) and (II), incident, reflected and refracted angles, respectively. In practice, such manually introduced phase distributions capable of defining phase discontinuities on propagating waves can be implemented by a monolayer of individual phase shift elements, which refers to the metasurface in Fig. 1.7.

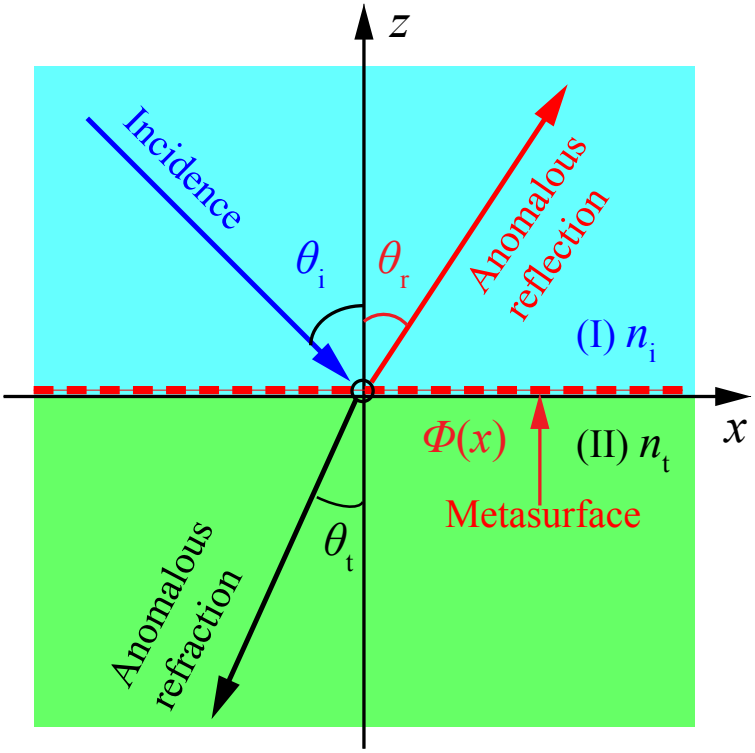

Figure 1.7 – Schematic diagram of generalized Snell's law.

Inspired by the pioneering work on optical metasurface[68], acoustic metasurfaces have been being extensively explored and become hotspots very recently. Acoustic metasurfaces can be defined as planar materials of subwavelength thickness capable of providing local phase shifts over a 2π span for arbitrary wave tailoring or extraordinary sound absorption. Even though both acoustic and elec-

tromagnetic waves follow Snell's law, acoustic metasurfaces cannot be readily achieved by directly transforming the concept of optics. In acoustics, there is no direct counterpart of plasmonic resonance induced by metallic antennas, which is crucial for optical metasurfaces in providing 0 to 2π phase shift. On the other hand, the application of plasmonic resonance in optical metasurface inevitably circumscribes the further downscaling of their thickness to deep subwavelength, which, however, is essential for acoustic metasurfaces in manipulating sound waves that have much larger and broader wavelength distributions, compared to visible optic waves. Naturally occurring materials can hardly possess adequate phase shifts and maintain thin properties, simultaneously.

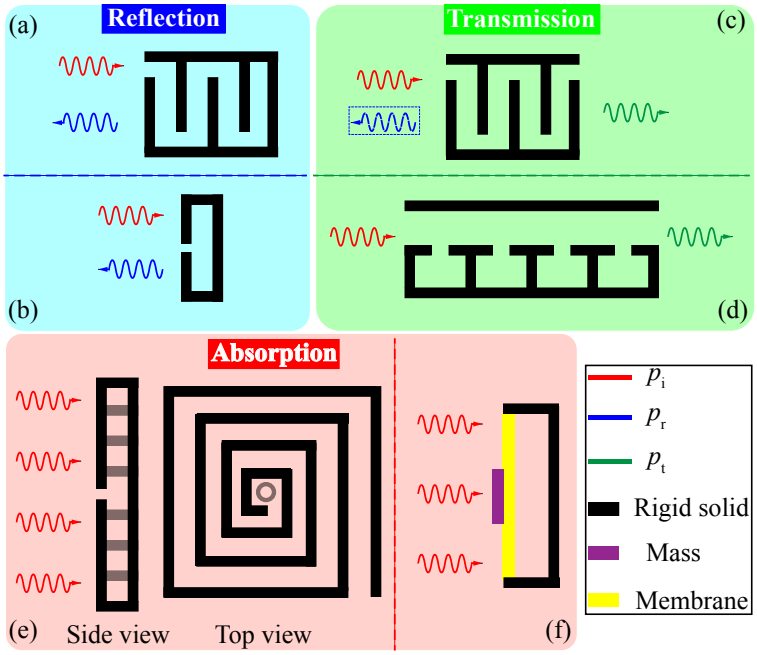

Figure 1.8 – Schematic diagram of typical conceptional designs for acoustic metasurfaces. (a) Labyrinthine element of space coiling and (b) Helmholtz-like element with local resonance for phase shift in reflected wave manipulation. (c) Coiling-up-space element and (d) arrayed HRs for transmitted wave control. (e) Space coiling element with perforated plate and (f) decorated membrane with hybrid resonance.

The design concepts precedently applied in PCs and AMMs for miniaturization, i.e., coiling up space[38], hybrid and local resonances[44, 45] achieved by

acoustic path elongating channels (zigzag, meandering, detouring), HRs, channel connected with HR arrays and HR with membranes, have been considered to devise acoustic metasurfaces. Because of the subwavelength or deep subwavelength features, most of the investigations on acoustic metasurfaces generally emphasize on their unique behaviors and capabilities in wave refraction, transmission or absorption, rather than internal wave propagating details which can be the research importance of PCs and AMMs. As far as acoustic wave manipulations are concerned, the phases for wavefront tailoring, and the amplitudes of the reflected or transmitted waves are the two essential parameters. The phases of reflected and transmitted waves could be tuned by coiling-up-space elements illustrated in Figs. 1.8(a) and 1.8(c), respectively, which can control the refractive indexes of the resulting metasurfaces by slowing down the waves to various degrees as required. For coiling up designs, the key point is to manipulate the effective lengths of acoustic path, and thus the geometries of the elements in Figs. 1.8(a) and 1.8(c) need to be varied to obtain such path with different lengths, i.e., various effective refractive indexes. In addition to the concept of coiling up space, local resonances and hybrid resonances of HR element and channel with arrayed HRs illustrated in Fig. 1.8(b) and 1.8(d) can also induce sufficient phase shifts of reflected and transmitted waves, respectively. In order to achieve effective and efficient reflection and transmission tailoring, the amplitudes of the reflected and transmitted waves should be maximized by properly configuring the element geometries to minimize the airborne dissipation caused by thermoviscous effects. For the acoustic metasurfaces in acoustic absorption, however, the amplitudes of both reflection and transmission should be minimized and most of the acoustic energy should be dissipated within the thin structures. Ultrathin acoustic metasurface element in Fig. 1.8(e) constructed by a perforated panel and a space-coiled channel with hybrid resonances can be used to achieve perfect absorption under low frequency range. Moreover, another ultrathin acoustic metasurface structure composed of the decorated membrane and a reflecting surface, between which a gas is sealed (Fig. 1.8(f)), can induce hybrid resonance and achieve total sound absorption at low frequencies.

Figure 1.8 just provides mainly typical conceptual and exemplary design elements to realize space coiling, local and hybrid resonances that could be applied

to achieve acoustic metasurfaces for controllable wave reflection, transmission and absorption. Many transformative structures and designs derived or inspired from those shown in Fig. 1.8 to construct acoustic metasurfaces for specific applications have been proposed very recently[69, 70].

Acoustic metasurfaces for reflected wave manipulations

As a kind of scalar wave, sound waves can be guided freely in artificial structures without cut-off frequencies, which enables the sound path control and the phase manipulation of acoustic waves by introducing labyrinthine designs[47, 61, 71–73]. For the reflected wave manipulation, as elucidated in Fig. 1.7, the reflected waves can be tailored by modulating the phase distribution in the interface boundary. Figure 1.9 demonstrates an exemplary metasurface for reflected acoustic wave focusing with generalized Snell's law, where both theoretical and experimental results are provided[74]. To achieve the focusing at the position (f_x, f_y), the phase profile along the boundary should be theoretically designed as Fig. 1.9(b) to realize the wavefront shown as an arc in Fig. 1.9 (a). The analytical result in Fig. 1.9(c) achieved by the theoretical boundary design shows good reflected wave focusing.

For the experimental part, eight labyrinthine elements in Fig. 1.9(d) with various sound paths and the resulting full 0 - 2π phase shifts were applied to construct the acoustic metasurface and implement the theoretical phase profile in the boundary for the previously designed reflected wave focusing. With an acoustic field scanning platform in Fig. 1.9(d), the experimental focusing result was obtained in Fig. 1.9(e), and both theoretical and experimental results reach a good consensus.

In addition to the reflected wave focusing illustrated in Fig. 1.9, negative reflection[75], retroreflection[76], acoustic surface wave conversion[77], arbitrary reflective beam forming[74], reflected acoustic lensing[77], sound reflective diffusion[56, 78] can also be achieved by various reflective acoustic metasurfaces. According to the aforementioned generalized Snell's law, for any predefined incident angle, the reflected angle can be arbitrarily assigned through modulating the phase along the reflective interface.

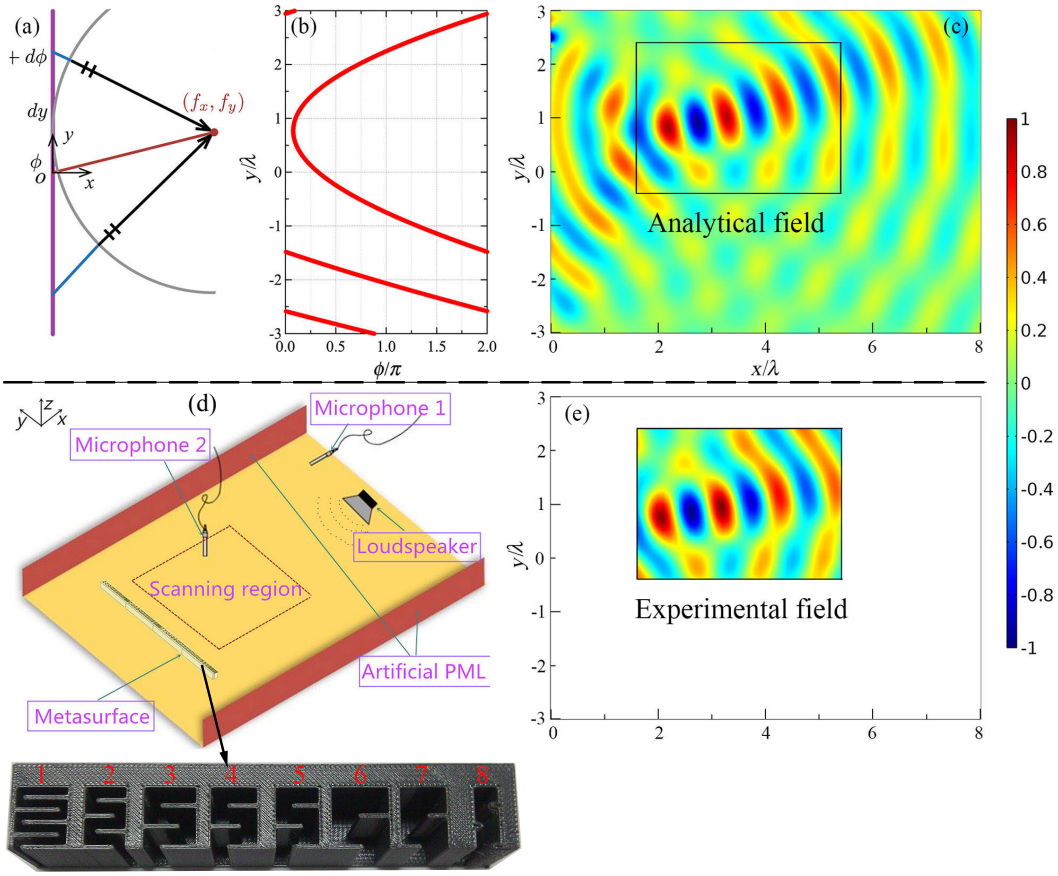

Figure 1.9 – An acoustic metasurface based on coiling-up-space elements for reflected wave manipulation[74]. (a) Schematic boundary design for the focusing at predefined position. (b) Theoretical phase profile along the interface required for the reflected wave focusing at designed position. (c) Analytical result of the designed focusing field. (d) Experimental setup for the reflective metasurface system. (e) Experimental result of the reflection focusing field.

Two incident beams with different angles are readily redirected by an acoustic metasurface to realize negative reflections[75] in Fig. 1.10(a). The incident and reflected angles can be designed to be identical[76], which means that the incident wave can be reflected back along the anti-parallel direction, as shown in Fig. 1.10(b). When the reflected angle is set to be $\pi/2$, i.e., parallel to the metasurface interface, the incident propagating waves are converted into acoustic surface waves in Fig. 1.10(c). More sophisticated and arbitrarily reflective beam forming can be theoretically and experimentally realized by

designing the phase distribution and the resulting metasurface in the boundary. A particular half-circle (radius r) trajectory formed by acoustic metasurface with phase distribution $\phi(y) = -k_0(y - 2r\sqrt{y/r})$ is illustrated in Fig. 1.10(d), and the reflected beam can be applied to detour obstacles[74]. Acoustic imaging can be one important application of reflective acoustic wave manipulations. A flat acoustic axicon realized by an acoustic metasurface[77], and a non-diffractive Bessel beam with a long length can be observed in Fig. 1.10(e).

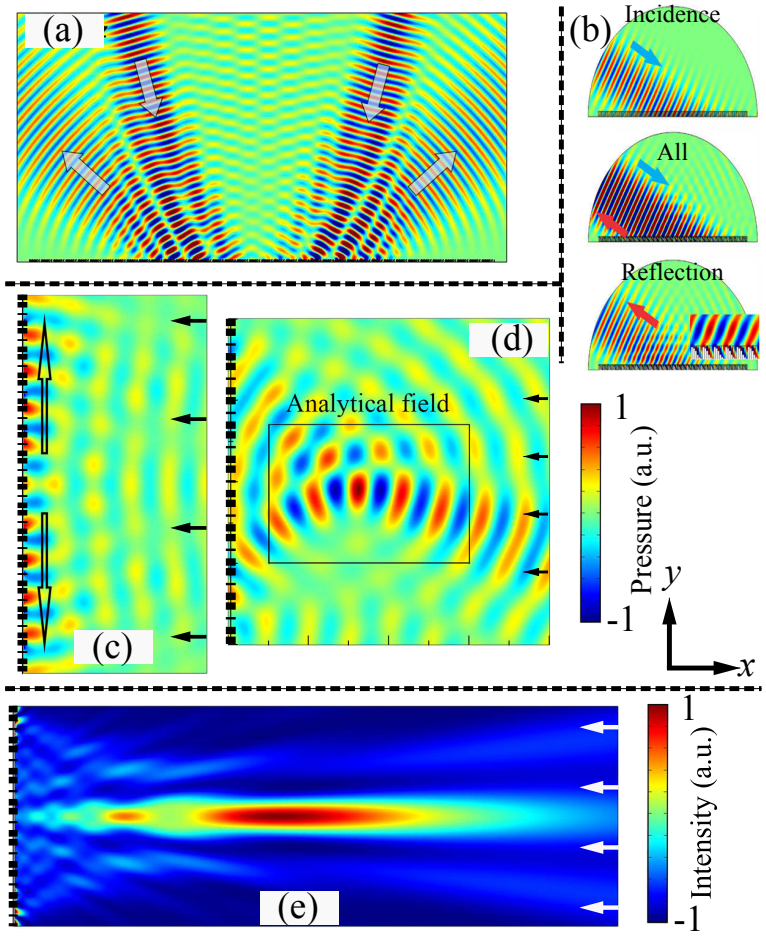

Figure 1.10 – Reflected wave manipulations with acoustic metasurfaces. (a) Negative reflection[75]. (b) Retroreflection[76]. (c) Surface acoustic wave conversion[77]. (d) Arbitrary reflection[74]. (e) Reflected acoustic lens[77].

As previously illustrated in Fig. 1.8, besides the concept of coiling up space, other physical mechanisms, such as local resonance[56] and hybrid reso-

nance[79], can also be applied to implement meta-atoms/elements for desired reflective phase shift. Through applying generalized Snell's law of reflection, planar acoustic surfaces constructed by Helmholtz resonators have been reported[80] to generate ordinary and extraordinary reflections. Meanwhile, a metasurface composed of grooves, for reflective wave field tailoring, has been theoretically and experimentally proposed[81] to tackle the common issue of bandwidth limitations in labyrinthine elements.

Different from the idea of elongating sound paths with coiling-up-space structures for phase shifting, local resonances take advantage of drastic phase variations around the resonating status of the structural elements. Generally, the thickness of the metasurfaces based on the coiling-up-space concept can be designed in the order of sub-wavelength, with negligible dissipations. The metasurfaces consisting of locally resonant elements can further reduce their thickness to deep-sub-wavelength order, maintaining high reflection ratio.

Excelling in wavefront manipulations, acoustic metsurfaces with exotic capabilities and sufficiently reduced thickness have demonstrated great potentials in advanced and even revolutionary wave applications. The broadly commercialized Schröeder diffuser (SD) could be alternatively realized by one order thinner acoustic metasurfaces[56]. Metasurface-based Schröeder diffuser (MSD) can be implemented by a 2D array of Helmholtz-like locally resonating elements to provide the phase distribution (2D quadratic residue sequence) in the interface required by conventional Schröeder diffuser[56]. Helmholtz-like elements can be good candidates to achieve local resonance and the resulting phase shift. As shown in Fig. 1.11(a), a small and successive modification in the neck width of the Helmholtz-like element can continuously and completely tune the phase shift to 2π range. The MSD and the experimental system for reflected diffusion are demonstrated in Fig. 1.11(b) and (c), respectively. Figures 1.11(d)-(f) illustrate the far-field scattering pattern, the scattered acoustic filed distributions in $x-y$ plane, and the scattering field directivity, of the MSD, respectively. Viewing from Figs 1.11(d)-(f), the MSD demonstrates high sound scattering performance on par with the conventional SD, in spite of one order thinner, which validates its promising application in architectural acoustics and beyond.

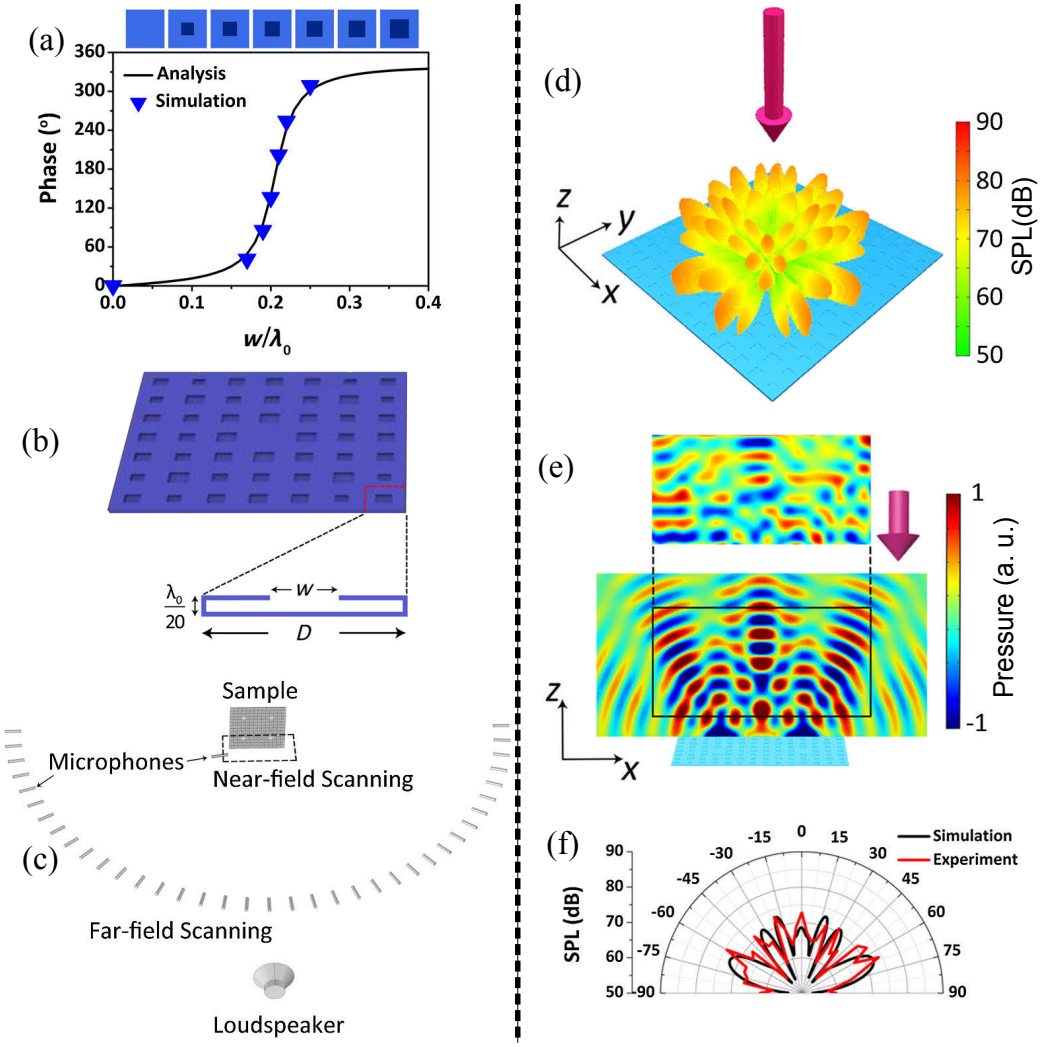

Figure 1.11 – An acoustic metasurface Schröeder diffuser (MSD)[56]. (a)Helmholtz-like elements and phase shift profile with respect to the width w. (b) Acoustic metasurface Schröeder diffuser composed of Helmholtz-like resonating elements. (c) Experimental setup for the reflective metasurface system. (d) The simulated 3D far-field scattering pattern of the MSD with normal incidence. (e) The measured (upper) and simulated (lower) scattered acoustic field distributions of the MSD in $x-y$ plane. (f) The simulated and measured scattering field directivity of the MSD.

Acoustic metasurfaces for transmissive wave manipulations

As another major branch of wavefront engineering, wave manipulations in transmissive field realized by acoustic metasurfaces share almost all the parallel applications, such as beam steering, beam forming, focusing, lensing, propagating to surface wave conversion, etc., which are previously introduced in reflective field. Similar to the reflective cases, delicate phase modulation along the interface in Fig. 1.7 remains to be essential in achieving transmissive wave steering. However, impedance matching of the transmissive metasurfaces with the ambient media, not necessarily required in reflective situations, should be carefully considered to ensure sufficient transmission of acoustic energy for effective application potential in practice. Therefore, in addition to the capability of phase shifting for desired wavefront tailoring, the candidate elements to construct the transmissive metasurfaces should also take into account the impedance matching.

Because of straightforward manner, the coiling-up-space concept to tune the length of sound path and the relative phase still prevails in the design of non-resonating elements for individual transmitted phase shift[35, 82, 83]. Labyrinthine elements proved promising candidates in achieving phase gradient in the interface through elongating the wave propagation length with their rigid coiled channels, demonstrating low acoustic absorption over a wide range of frequency[38]. Nevertheless, the impedance of typical labyrinthine elements cannot well match that of the surrounding medium, e.g., the air. In order to manage the impedance matching, delicately processed coiling-up-space structures, such as tapered labyrinthine element[84], horn-like coiling-up-space elements[69, 70], spatially varied coiling-slit elements[85], filled-up space coiling designs[47], space coiling structure with impedance matching layers[86], etc., have been extensively proposed.

Tapered structural designs have been broadly used in conventional musical instruments and loudspeakers to improve impedance matching and bandwidth through their gradually varying cross-section area. Labyrinthine elements illustrated in Fig1.12 (a) are tapered as spiral geometries to achieve desirable transmissive phase shifts with 2π range and sufficient impedance matching,

simultaneously. With designing the phase gradient along the interface according to the generalized Snell's law (Eq.1.2), various kinds of predefined transmitted wave controls can be theoretically accomplished. Subsequently, the theoretical phase distributions for various wave manipulations can be discretized and further implemented by an array of elements with individual phase shits, i.e., acoustic transmissive metasurfaces. An exemplary metasurface composed of these tapered labyrinthine elements for typical negative refraction is provided in Fig. 1.12(a)[82]. With the predefined phase design and these tapered elements, focusing, propagating to evanescent wave conversion, and other wave steering applications can be also realized[82].

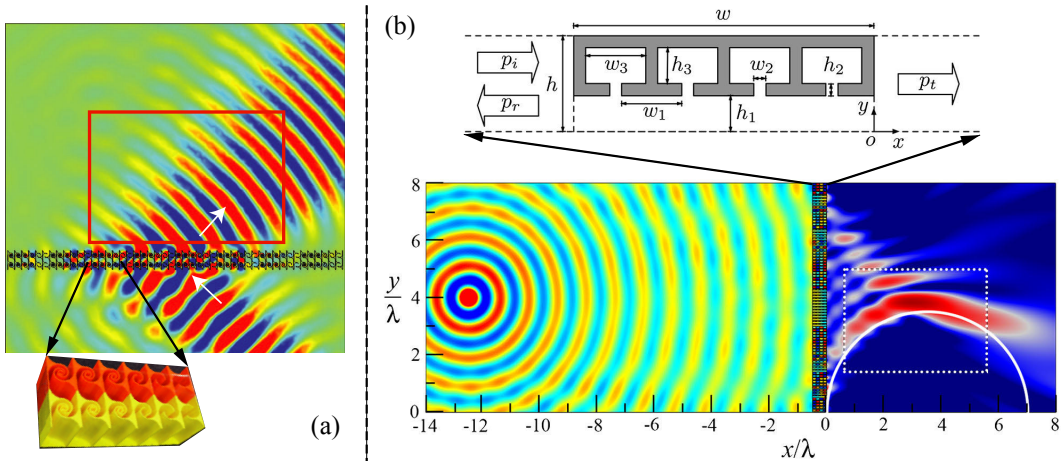

Figure 1.12 – Two acoustic transmissive metasurfaces. (a)Negative refraction realized by the metasurface composed of tapered labyrinthine elements[82]. (b) Self-bending beam achieved by the metasurface constructed by hybrid resonating Helmholtz cavities[87].

In addition to the general concept of coiling up space, hybrid resonances produced by integrated cavity resonators and channels are another popular method to acquire a complete 2π phase shift of transmitted waves. As illustrated in Fig. 1.12(b), a typical subwavelength element with hybrid resonance is composed of four Helmholtz resonators connected in series to a straight pipe for phase shift and impedance matching in the same time. The Helmholtz resonators are targeted for the phase shift of transmissive waves, while the straight pipe provides Fabry-Perot resonance and impedance matching of the whole

element. The hybrid resonance, i.e., the coupling resonance between the pipe and the Helmholtz resonators, ensures the nearly total transmission as adjusting the width h_1 of the pipe for gradual propagating phase shift, simultaneously. Metasurfaces composed of such hybrid elements possess high spatial resolution and can form complex beam steering applications, e.g., self-bending beam in nonparaxial approximation in Fig. 1.12(b), where the challenge lies in the abrupt and huge phase variation in the predefined phase profile.

Besides the primarily proposed anomalous refractive beam tailoring, the recent research hotspots of transmissive metasurfaces include (a) asymmetric acoustic transmission, (b) vortex beam forming and (c) acoustic holograph. Governed by the well-known reciprocity principle, acoustic waves demonstrate symmetrical propagation behaviors from both sides of the medium, irrelevant of sound impinging directions. In general, asymmetric acoustic transmission allows different wave propagation phenomena with opposite incident direction. Vortex acoustic beam mean its acoustic field possessing spiral phase dislocations and orbital angular momentum (OAM)[88], which can transfer and deliver energy and matters. Acoustic holograph is an acoustic imaging and communication technology which can record and reconstruct acoustic information[89].

Beyond the context of acoustic metasurfaces, asymmetric sound transmission have been extensively achieved with lossless passive or active systems[54, 64, 90–92], which, however, display the deficiencies of bulky size, inflexible control and complicated designs, in general. In the scope of acoustic metasurfaces, one method to realize asymmetric sound transmission is to integrate a near zero-index-metasurface (ZIM) with a gradient-index metasurface (GIM)[93, 94], where the normal incident waves with the direction from GIM to ZIM are deflected by GIM and totally reflected by NIM due to the near zero critical angle, while passing through both metasurfaces from the opposite direction, i.e., from ZIM to GIM. Conventionally minimized or avoided for high performances[95], losses ubiquitously present in the process of wave propagation have been, however, favorably harnessed and explored to achieve new physics and the corresponding phenomena[52, 96, 97].

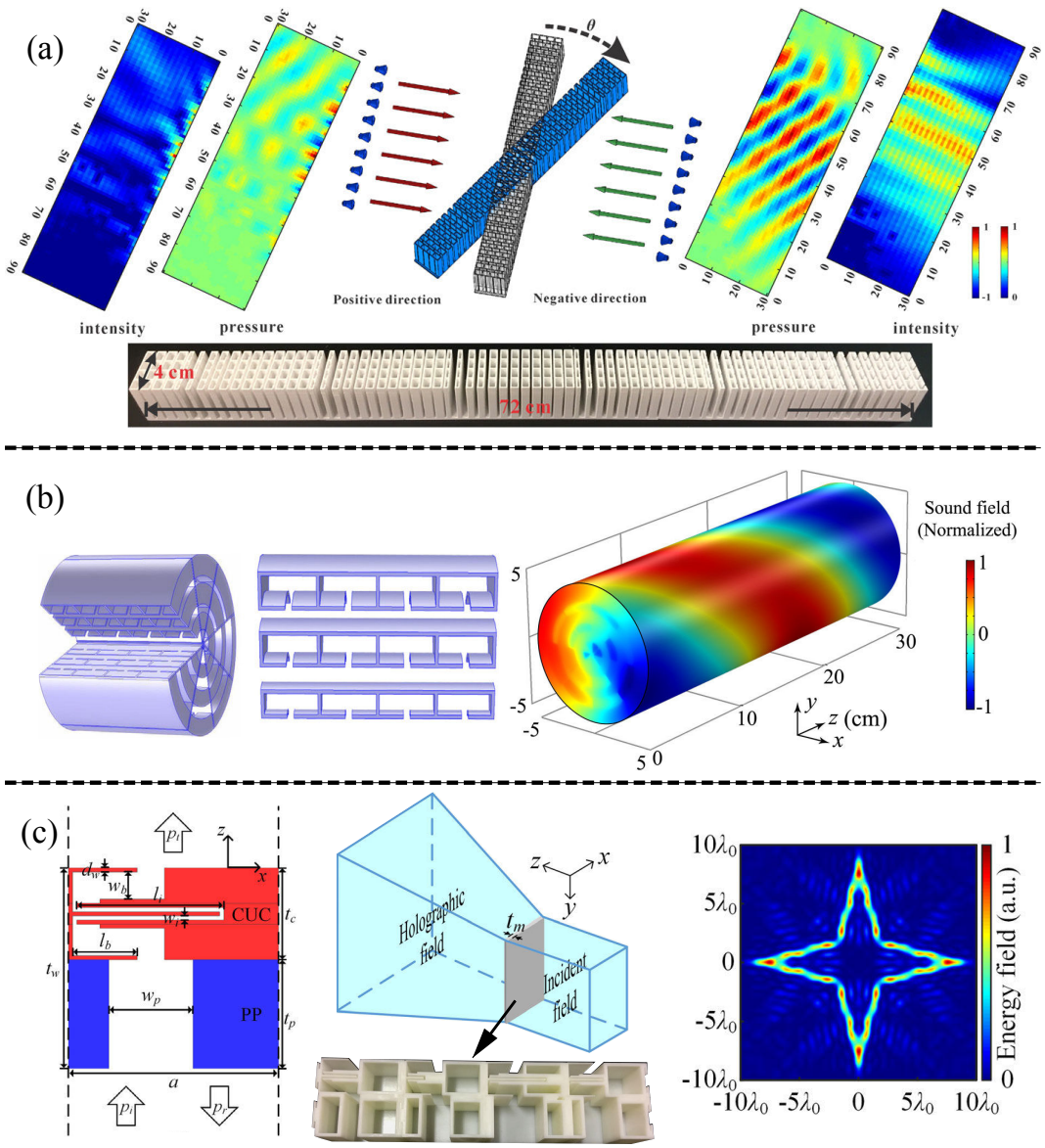

Figure 1.13 – Transmissive metasurfaces for innovative applications. (a) The lossy acoustic metasurface and the measured acoustic transmissive fields[98]. (b) Hybrid Helmholtz elements and the resulting vortex field[99]. (c) Orifice-coated labyrinthine elements and acoustic energy distribution on the image plane.

As illustrated in Fig. 1.13(a), another scheme for asymmetric transmission simplifies the previous double-metasurface designs by harnessing the intrinsic

losses in GIM. The transmission of the lossy GIM is highly dependent on the incident angles, due to the different transmission behaviors caused by the loss-induced suppression of diffraction under various incident angles. As shown in Fig. 1.13(a), for negative incidence case (θ=-25°), the multiple reflections within the GIM are reinforced, which accumulate acoustic energy within the hybrid (Helmholtz resonators and pipe) elements and suppress the high order diffractions; for positive incidence case (θ=25°), waves well transmit the GIM with negligible multiple reflections[98]. Even though asymmetric transmission can be implemented by these two schemes, neither of them breaks the reciprocity principle. Metasurface-based systems for asymmetric transmission possess the flexible and planar features, which would be desirable in practice.

Another fantastic application of acoustic transmissive metasurfaces is to devise vortex beam with OAM. Acoustic waves with spiral phases and OAM have been actively[100, 101] and passively[102, 103] achieved by phased array transducers and structures with spirally dislocated profiles (e.g., helical substrate, spiral-shaped object), respectively. One scheme to achieve vortex beam with metasurface is to introduce acoustic resonances in a plane (metasurface) to produce the desired wave number for twisting the wave vectors into phase screw dislocation[99]. As shown in Fig. 1.13(b), the round planar metasurface composed of hybrid resonating structure is divided into 8 sectors, which consistently and discretely cover 0-2π phase with a resolution of π/4. In Fig. 1.13(b), the simulated transmission through the metasurface layer demonstrates desirable twisted wavefronts along z-axis.

As an essential means for acoustic wave manipulations, holography can be used to achieve imaging[89], medical treatments[104], acoustic traps[105], etc. Traditional acoustic holography are implemented by active phased arrays of discrete and independently driven transducer elements[105]. Acoustic holography achieved by active phased array has the disadvantages of complex structure and circuits. Acoustic metasurface can flexibly and passively control the phase and amplitude of acoustic waves, and further realize acoustic holography. As shown in Fig. 1.13(c), coating unit cells with perforated panel are applied to construct metasurface for acoustic holographic imaging, where the coating labyrinthine elements are served for the phase control and perforated panels are for the

amplitude manipulation, independently. With the respective modulations of phase and amplitude achieved by the acoustic metasurface consisting of these hybrid labyrinthine elements, 3D holographic imaging can be well acquired in the right of Fig. 1.13(c).

Acoustic metasurfaces for absorption

Various kinds of acoustic noises are omnipresent in domestic and industry environments, which could negatively influence our acoustic environment in general. Sound absorption and noise reduction or isolation have always been one of the main hot topics in acoustics. Traditionally, porous and fibrous materials[106], gradient index materials, micro-perforated panels with backed cavities[107], have been broadly employed for acoustic absorption. In general, these designs either lack perfect impedance matching or result in bulky sizes comparable to wavelength, which lead to inefficient and impractical absorption in low frequencies. The advent of metasurfaces with exotic properties and anomalous capabilities makes traditionally-restrained applications, e.g., wave manipulations with sub-wavelength or deep-sub-wavelength structures, possible. Two specific planar acoustic metamaterials or metasurfaces with deep-sub-wavelength thickness, i.e., decorated membrane resonator (DMR)[55] and space-coiling sink covered with perforated plate[108] illustrated in Fig. 1.14 prove promising schemes for perfect absorption.

Membrane-type of acoustic metasurfaces composed of different DMRs have demonstrated near total transmission at the resonant frequencies[109], while complete reflection at the anti-resonant frequencies[41] due to the decoupling from the incident waves. In between, the hybrid resonances have been applied and realized by innovative membrane-type metasurfaces[55]. As illustrated in Fig. 1.14(a), the membrane-type element consists of a DMR, a reflective surface (backed aluminum plate), and a thin sealed gas layer in between. The DMR is composed of a membrane with uniform strain and a decorated platenet. The first eigenmode (112 Hz) and the second one (888 Hz) are characterized as Mode 1 and Mode 2 by vibration of membrane in Fig. 1.14(b), where W/W_S is the ratio of displacement of the membrane to the amplitude of incident waves. The

fundamental mode with high vibration amplitude in the center of the membrane is selected and investigated.

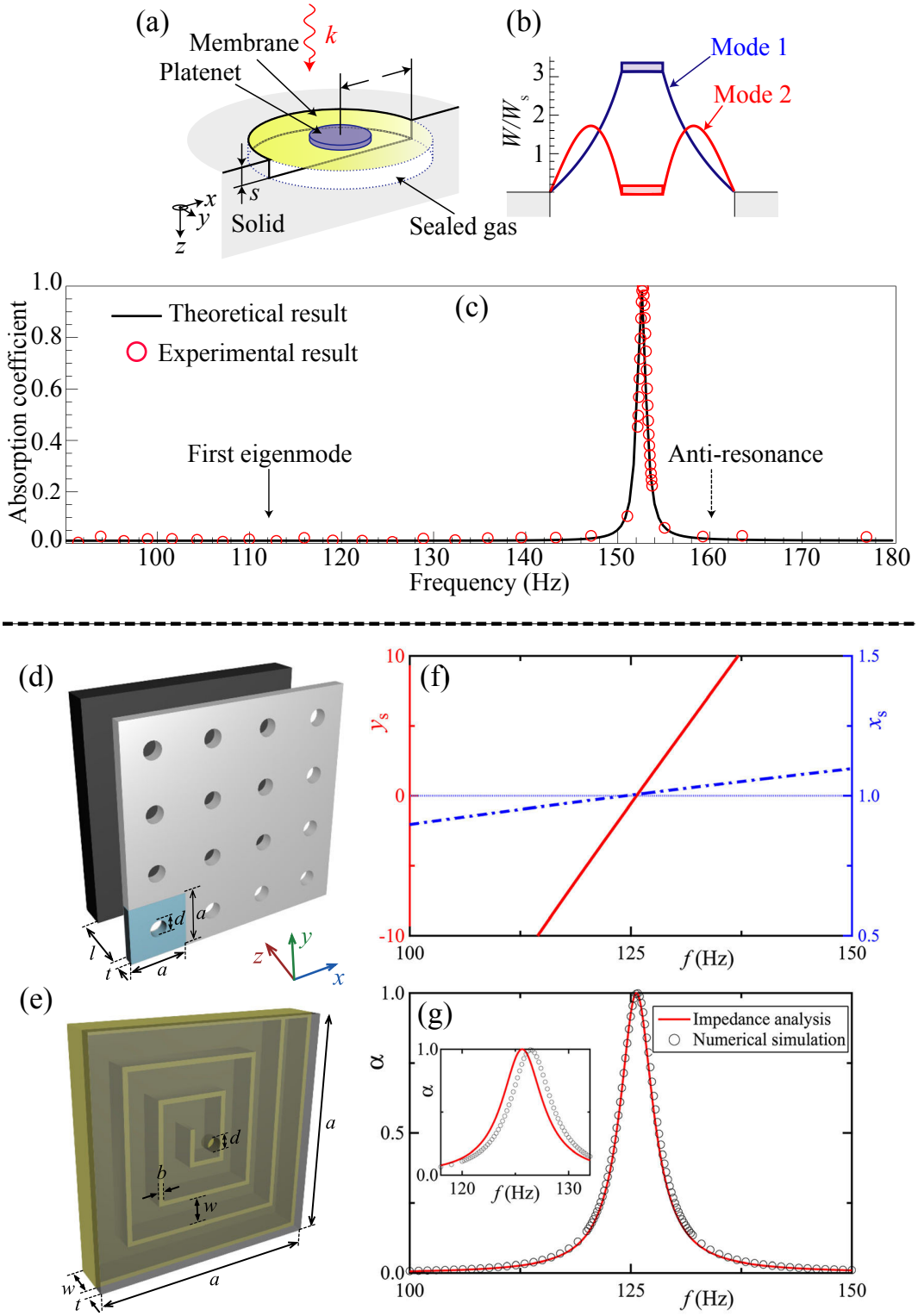

Figure 1.14 – Two absorbing ultrathin metasurfaces. (a) A DMR element. (b) Cross-sectional illustration of the lowest eigenmodes of a DMR. (c) Absorption coefficients as a function of frequency[55]. Conventional perforated panel system (d) and acoustic metasurface element (e) composed of perforated plate coupled with coiled air channel. (f) Absorption coefficient. (g) Normalized specific resistance x_s and reactance y_s[108].

The measured and simulated absorption coefficients as a function of frequency are illustrated in Fig. 1.14(c), and a sharp absorption peak (> 0.99) with a small width of 1.2 Hz can be observed at 152 Hz, which indicates perfect impedance match with air. The hybrid resonances result in the coupling among the gas, the reflecting surface, and the DMR. The large displacement of the DMR induced by the hybrid resonance, rather than its material dissipation, plays a vital role in the perfect absorption. Based on the DMR metasurface element, total absorption at multiple frequencies can be further achieved by integrating elements with respectively tuned platelet masses[55]. However, the fragility of such metasurface resulting from the sealed gas layer and the membrane could limit its practical application in general.

Besides the hybrid resonances, the wide-spread coiling-up-space concept has been employed[108, 110] to implement acoustic metasurfaces with deep-subwavelength features for perfect absorption. Distinct from conventional absorbers based on fibrous materials whose required thickness for total absorption depends on the phase delay (reactance), the resistance provided by the space-coiling design dominates the thickness. Therefore, the thickness of the metasurfaces based on coiling up space concept can go down to deep-subwavelength scale, which greatly favors the perfect absorption in low frequencies.

The coiling-up-space design can provide sufficient dissipation (resistance) for the refracted waves inside, while the remaining challenge is the impedance mismatch to the background medium. To this end, a coiled air channel coupled with a conventional perforated plate system (Fig. 1.14(d)) has been proposed in Fig. 1.14(e) to achieve significantly reduced thickness and impedance matching, simultaneously[108]. Through general impedance analysis, the absorption coefficient for effective boundary can be express as:

$$\alpha = \frac{4x_s}{(1+x_s)^2 + (y_s)^2}, \tag{1.4}$$

where x_s and y_s are the acoustic specific resistance and reactance normalized to the impedance of the air. According to the Eq. 1.4, total absorption ($\alpha = 1$) requires that two crucial conditions, i.e., the impedance matching $y_s = 0$ and the resonant state for energy dissipation $x_s = 1$, are satisfied in the same time. As

can be seen in Fig. 1.14(f), these two conditions are achieved simultaneously by the coiled element at the frequency around 125 Hz. The absorption spectrum of the presented metasurface demonstrates a unit absorption at the resonant frequency (around 125 Hz) in Fig. 1.14(g), and its thickness is 1/233 of the working wavelength, which verifies the capability for perfect absorption in deep subwavelength scale[108]. The absorbing metasurface composed of coiled channel and perforated plate should have advantages over others, due to its straightforward design and durability in practical applications.

1.2 Acoustic energy harvesting (AEH)

With the increasing energy crisis and environmental issues caused by traditional energy resources, various kinds of renewable, clean and applicable energy have attracted worldwide attention all these years. Among them, the mechanical[111], solar[112, 113], thermal[114] and biochemical[115] forms of energy, abundantly available in nature, could provide alternative power supplies to the growing energy consumption requirement. Energy harvesting can be defined as collecting and usually converting these forms of ambient energy into electrical energy. As a kind of ubiquitous and sustainable mechanical energy with low power density, sound or noise can act as a power source for microelectronic autonomous devices, especially in remote or embedded systems.

Sound pressure level (SPL) is a well-known term to evaluate the quantity of sound. Because of the wide range of pressure amplitudes, SPL is defined as a logarithmic measure of a time-root-square pressure (p_{rms}) to a reference value p_{ref}, i.e., SPL=20log($p_{\mathrm{rms}}/p_{\mathrm{ref}}$). The reference value p_{ref}=20 μPa is the believed hearing threshold of human hearing. The acoustic energy density in uniform nonviscous (ideal) medium can be correlated with pressure as $\varepsilon = p^2/\rho c^2$[37], where p, ρ and c represent sound pressure, density and sound velocity of the medium. Another more frequently used parameter to depict acoustic energy is the sound intensity, which by definition is the energy that travels through a unit

area per unit time. Sound intensity can, therefore, be written as

$$I = \frac{p^2}{\rho c}, \tag{1.5}$$

where ρc is the characteristic impedance of the medium. As can be seen from Eq. 1.5, the acoustic energy density depends on the pressure of the wave and the impedance of surrounding medium. Low power density is the intrinsic drawback of the acoustic energy. The exemplary sound sources and the corresponding sound intensity are listed in Table 1.1. Consider the case of a sound source in air with a SPL of 120 (dB) that renders the threshold of pain to human ears, the power density with unit area can be calculated with Eq. 1.5 as I_{rms} = (20 Pa)^2/1.21 kg m^{-3}/343 m s^{-1} = 1 W m^{-2}. As illustrated in Table. 1.1, sound

SPL(dB)	Intensity	Source example
20	0.1 nW/m^2	Whisper
40	10 nW/m^2	Rainfall
60	1 μW/m^2	Conversation
80	0.1 mW/m^2	Vacuum cleaner
100	0.01 W/m^2	Road drill
120	1 W/m^2	Ambulance siren
160	10 kW/m^2	Jet engine

Table 1.1 – Several representative sources or environments with a wide range SPL values and their corresponding intensities.

sources with SPL below 100 dB, which cover most of domestic human activities, demonstrate low power density feature, compared with the solar energy density indoor and outdoor of around 0.1 W m^{-2} and 100 W m^{-2}, respectively.

Practical AEH requires either high SPL sources or harvesters with large surface area. Besides these concerns, energy transduction from acoustic to electric also dominates the whole efficiency and effectiveness of AEH systems. There are three main methods for mechanical to electrical energy conversion, i.e., piezoelectric, electromagnetic and electrostatic means. Piezoelectric transduction relies on the phenomenon that electric charges accumulate in the solid materials (i.e., piezoelectric materials) when experiencing mechanical stress. Electromagnetic transduction uses the moving magnets through a ferromagnetic

circuit containing a coil to generate electricity by Faraday's law. Electrostatic transduction utilizes capacitor structures to produce electrical energy when applied a mechanical force. All these three methods can be effectively applied for mechanical energy harvesting with various trade-offs. However, piezoelectric method prevails in AEH over others due to its advantages of high energy conversion efficiency, mature fabricating technology, extreme miniaturization, flexible phases (soft or solid), etc. The piezoelectric design concepts and models for mechanical to electrical energy transduction are widely investigated and relatively mature[116, 117], which are not the research focus of this dissertation. Instead, various structures based on different types of wave localization mechanisms for AEH are sufficiently covered.

1.2.1 AEH with resonators

Because of the low power density property, sound generally needs to be confined or localized before it can be effectively and efficiently converted into electrical energy. Intuitively, the classical Helmholtz resonators, and other kinds of tube or chamber resonators have been applied to implement AEH systems. A typical Helmholtz resonator is composed of a neck connecting to a cavity. Through lumped element model (LEM) analysis, the effective mass and compliance of a Helmholtz resonator with short neck length ($kl \ll 1$) can be expressed as

$$M_e = \frac{4\rho_0 l}{3S}, C_e = \frac{V}{\rho_0 c_0^2}, \tag{1.6}$$

respectively, where S, l and V are the section area of the neck, length of the neck, and cavity volume (Fig. 1.15(a)), respectively. The frequency of HR for impedance matching is thereby $f_{res} = 1/2\pi\sqrt{M_e C_e}$ at the resonant status according to the equivalent circuit analysis.

A HR with the back wall replaced by a compliant composite diaphragm possessing a piezoelectric ring connecting to a rectifier circuit and a load was proposed to construct the electromechanical HR (EMHR) for AEH in Fig. 1.15[118]. Experimental measurements of the EMHR AEH system at its resonance status demonstrated an output power density of 0.34μW cm^{-2} with an acoustic inci-

dence of 149 dB, and a potential power density of 250 μW m^{-2} was theoretically anticipated with an improved fabrication process[118].

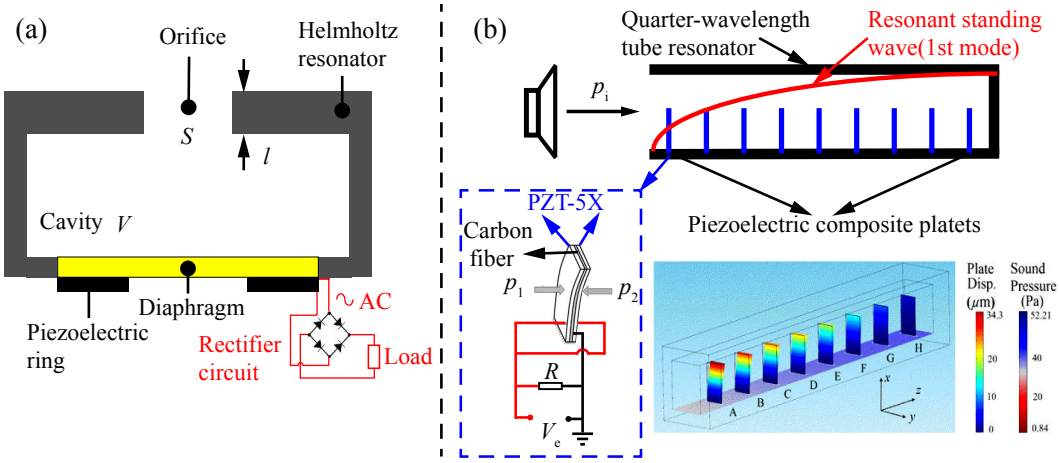

Figure 1.15 – Acoustic energy harvesters based on Helmholtz and tube resonators. (a)An AEH system based on Helmholtz resonator[118]. (b) An AEH system based on quarter wavelength-tube resonator[119].

The AEH system based on EMHR was further improved by adopting flyback converter instead of direct charging circuit to produce an output power of 30 mW under an acoustic incidence of 160 dB[120]. Piezoelectric polyvinylidene fluoride (PVDF) cantilever was integrated into a HR for AEH[121], and the maximized AEH efficiency can be acquired by tuning the resonance of the PVDF cantilever with that of the HR. Recently, an AEH system consisting a modified HR with a conical neck and a cantilever beam has been proposed to realize a broadband, multi-frequency and high-performance properties. The harvester demonstrated three output peaks at three different frequencies, and a maximum power of 214.23 μW was acquired when subjected to an acoustic incidence with SPL 130 dB[122].

In addition to the Helmholtz resonators, other chamber resonators, e.g., a half wavelength tube resonator (HWTR) and a quarter wavelength tube resonator (QWTR), can also be applied to confine acoustic energy. A HWTR is a tube with half wavelength long and both ends open. A QWTR is a tube of a quarter length long with one end open and the other closed. The damping capacities of these resonators have been investigated[123], and for the same volume, the QWTR

exhibits higher damping capability over HWTR, in spite of the same damping mechanism. Because of the higher damping or larger impedance matching capabilities, QWTRs are widely applied for AEH[119, 124]. As illustrated in Fig. 1.15(b), a QWTR is integrated with an array PZT cantilevers to implement AEH[119]. As can be seen in the lower part of Fig. 1.15(b), the output voltage and power can be optimized by filling the PZT cantilevers in the front half part of the tube instead of the whole. An optimized output voltage of around 5 V was achieved with an incidence sound pressure of 100 dB. An output voltage of around 15.7 V and the corresponding power density of 0.635 mW cm^{-2} could be acquired under an incident sound pressure of 110 dB.

Even though HRs or other cavity resonators can effectively realize AEH, the strategy based on resonators suffers from the defects of bulky structures and uncontrolled AEH in general, which inevitably limits their practical applications. The previously introduced metamaterials with exotic capabilities have revolutionized a series of traditional applications, including AEH, due to their obvious advantages in effective and efficient wave manipulations. The innovative AEH concepts based on AMMs will be addressed in the following section.

1.2.2 AEH with phononic crystals and metamaterials

Phononic crystals and acoustic metamaterials have demonstrated tremendous potentials in AEH, due to their innovative mechanisms and unconventional wave localization behaviors. As an important application of phononic crystals and metamaterials, the defect mode in the band gaps can be effectively and efficiently applied for wave focusing or localization, and the subsequent AEH[125, 126]. To be more specific, the resonators (meta-atoms) the PCs or AMMs are adjusted to achieve the band gaps with bandwidth as broad as possible, and then several resonators are removed from the PCs or AMMs to create cavity or line defect to induce defect mode. The waves are localized or confined in the defect cavity or line with the acoustic incidence at the defect mode, and the confined acoustic energy is then converted into electricity through piezoelectric method. As illustrated in Fig. 1.16(a), a point is created by removing a rod of a perfect sonic crystal, and the defect mode can be observed in the band structure

of the defected sonic crystal[125]. Through the airborne analysis, the sound transmission level evolution towards frequency is plotted in Fig. 1.16(b), and a high sound transmission is acquired at the defect mode frequency.

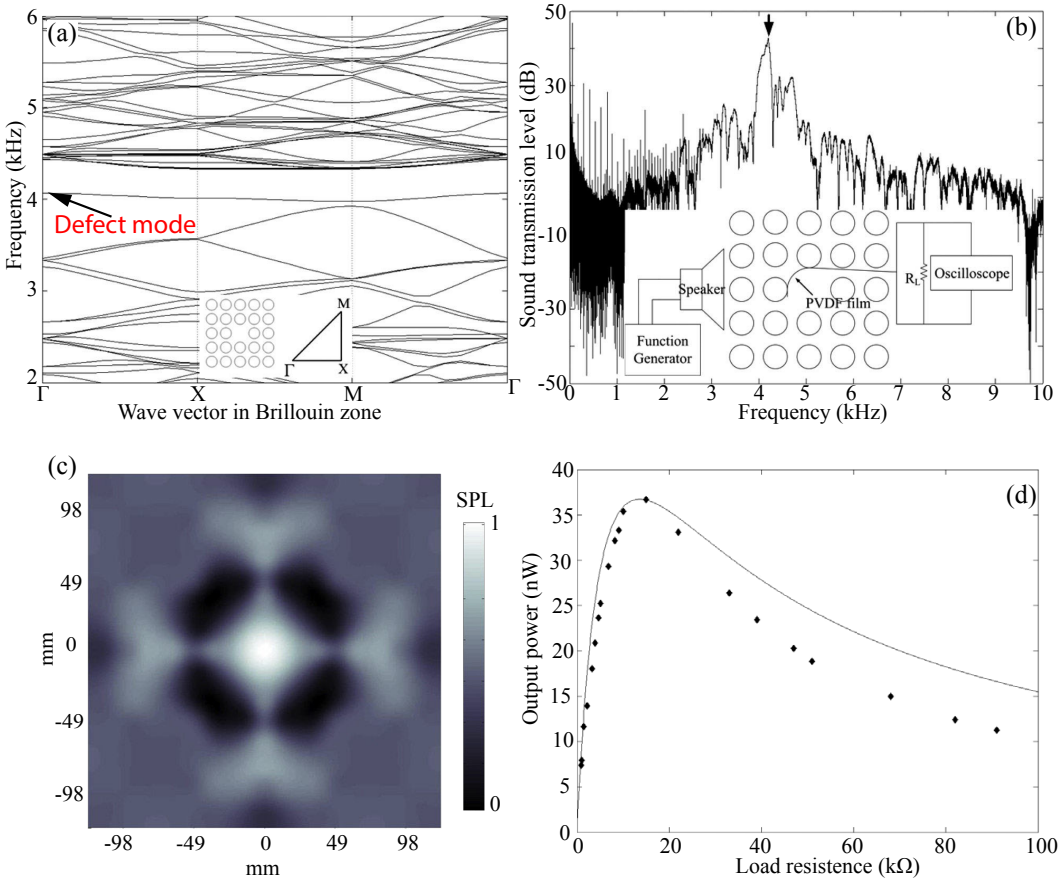

Figure 1.16 – An AEH system based on a phononic crystal. (a) The band structure of the sonic crystal with a defect. (b) The sound transmission level of the sonic crystal with a defect and the AEH system. (c) Sound pressure distribution of the sonic crystal with a defect in the center. (d) Experimental and theoretical output power from the AEH system.[125, 126].

As shown in Fig. 1.16(c), sound pressure level in the defect cavity is much higher than other regions of the sonic crystal, which indicates that the acoustic energy is confined in the defect as designed and anticipated. The experimental and theoretical output power obtained from the AEH system based on the defected PC is illustrated in Fig. 1.16(d), and the maximum output power is

about 37 nW with the load resistance of around 15 kΩ. The power scavenging efficiency of the PC with a defect is 625 times larger than that without[126].

Acoustoelastic crystals and metamaterials have also been applied for AEH recently. Parabolic acoustic mirror consisting of an aluminum plate and parabolically deposited stubs were used to focus elastic wave and the energy harvesting[127]. The similar concept based on defect and band structures has been used in elastic metamaterials for acoustoelastic energy harvesting[127, 128]. Phononic crystal Luneburg lens was proposed to focus and harvest elastic energy from onmidirectional incidence[129].

Recently, an acoustic metamaterial based on the concept of coiling up space has extended its application into AEH[130]. Distinct from the concept of taking advantage of defect mode, the space coiled acoustic metamaterial composed of two parallel metasurfaces and a cavity in between confines the acoustic energy through improving refractive index and forming half wavelength resonance. A piezoelectric bimorph plate is placed in the cavity to convert acoustic energy into electrical energy. The elongated zig-zag channels increase the refractive index and thus contribute to wave compression and localization inside the cavity. A complete transmission can be ensured by tuning the system for the half wavelength resonance (Fabry-Perot), due to the absence of cut-off frequency. A strong SPL gain of 16 dB at 600 Hz can be obtained, and the system is 11 times smaller than the wavelength. A maximum output power of 0.345 μW was acquired for the incidence SPL of 100 dB[130].

The overall noise level around the world is increasing year by year, and the omnipresent noise could negatively influence the life quality, work efficiency, and even safety, in general. On the other hand, with the tremendous development of low-power stand-alone electronic devices (wireless sensors, IoTs, etc.), and the inevitable environmental issues caused by traditional battery-related sources, the alternative and innovative power sources are pressingly demanded. Acoustic energy harvesting should attract broad and increasing attention from both scientific and industrial communities, due to its noise abatement and power supply capabilities, simultaneously. Among the emerging technologies, AEH with PCs and AMMs is preferably desirable and practical because of the advantages of miniaturization, high efficiency, flexibilities, etc.

The best way to predict the future is to create it.

Peter Drucker

Chapter 2

AEH with planar acoustic metamaterials

Contents

In this chapter, we theoretically report on an innovative and practical acoustic energy harvester based on a defected acoustic metamaterial (AMM) with piezoelectric material. The idea is to create suitable resonant defects in an AMM to confine the strain energy originating from an acoustic incidence. This scavenged energy is converted into electrical one by attaching a structured piezoelectric material into the defect area of the AMM. We show an acoustic energy harvester based on a meta-structure capable of producing electrical power from an acoustic pressure. Numerical simulations are provided to analyze and elucidate the principles and the performances of the proposed system. A maximum output voltage of 1.3 V and a power density of 0.54 μW/cm^3 are obtained at a frequency of 2257.5 Hz. The proposed concept should have broad applications on energy harvesting as well as on low-frequency sound isolation, since this system acts as

both acoustic insulator and energy harvester.

2.1 Introduction

With the increase of the environmental issues caused by traditional resources, renewable and clean forms of energy have attracted worldwide attention nowadays. Energy harvesting is defined as gathering and storing various forms of ambient energy such as sunlight[131], wind[132], heat[133] , mechanical vibration[116], biochemical effect[134] , etc., for later use. As a kind of sustainable and pervasive energy yet sometimes undesired interference, sound may act as a renewable and clean power source for energy production as well as for micro electronic devices, especially in remote or embedded systems[135].

Because of the intrinsic drawback of low power density, sound energy generally needs to be confined or localized before it can be effectively harvested and converted into electric energy through piezoelectric, electrostatic or electromagnetic means. Intuitionally, traditional resonating structures, such as Helmholtz resonators[118, 120] and other chamber resonators[119, 136] are utilized to achieve acoustic energy harvesting (AEH).

On another hand, innovative engineered materials, such as phononic crystals (PCs)[12] and acoustic metamaterials(AMMs)[30], emerging recently with rich physics and many extraordinary capabilities[32, 108, 137], have intrigued compelling interest among scientists and engineers for the applications in energy harvesting field[127, 128, 138]. Based on the mechanisms of the Bragg scattering and local resonance, the acoustic band gaps (BGs) of PCs and AMMs can be tuned or designed to realize AEH. Wu et al.[126] proposed an acoustic energy harvester composed of a square sonic crystal consisting of polymethyl methacrylate cylinders in the air back-ground. A power harvesting efficiency 625 times larger than that without sonic crystal is achieved in their report[126]. However, the property of a phononic crystal that large lattice constant leads to low central frequency may hinder its engineering applications in low-frequency situations due to the space and intensity limitations. Overcoming the mass density law of ordinary PCs, planar AMMs proposed by Assouar et al.[137, 139] show the properties of low sound transmission loss (STL) and strong strain energy con-

finement properties at low frequency range, which provides the potentials of sound insulation and acoustic energy harvesting. Meanwhile, the planar AMMs possess the advantages of easy fabrication, spacial efficiency and tough durability, favoring their applications in various situations. Metamaterial-inspired planar structures for mechanical wave energy harvesting have been proposed by Carrara et al. [127] based on the concepts of wave focusing, wave guiding and energy localization. Their stub-plate structure with a defect in the center cannot support the propagation of the mechanical wave from the side of the plate, thus leading to limited energy confinement efficiency in the defected area. Instead of concerning the vibration source, we propose in this chapter an innovative concept to scavenge the airborne acoustic wave energy by using a planar AMM with piezoelectric material, which can effectively address the issues of noise and efficiently harvest the sound energy as well, regardless of low frequency limitations[140].

2.2 Theoretical modeling and analysis

The proposed AEH system consists of acoustic energy confinement part (acoustic model) and strain energy conversion part (electrical model).

As schematically illustrated in Fig. 2.1, an array of silicone rubber stubs are periodically deposited on a thin homogenous aluminum plate lying in x - y plane, and a defect is created by removing four stubs to confine the strain energy originating from the acoustic wave incidence in z direction. A PZT patch is attached to the defected region to convert the localized strain energy into electrical energy.

As a locally resonant sonic crystal, the 2D periodic arrays of resonators (stubs) and the aluminum plate are considered uniform. The commonly applied plane wave expansion method could be used to analyze the acoustic-structure interaction behaviors. The structure can be modeled as an infinite thin plate with an array of mass-spring resonators[31, 33, 141].

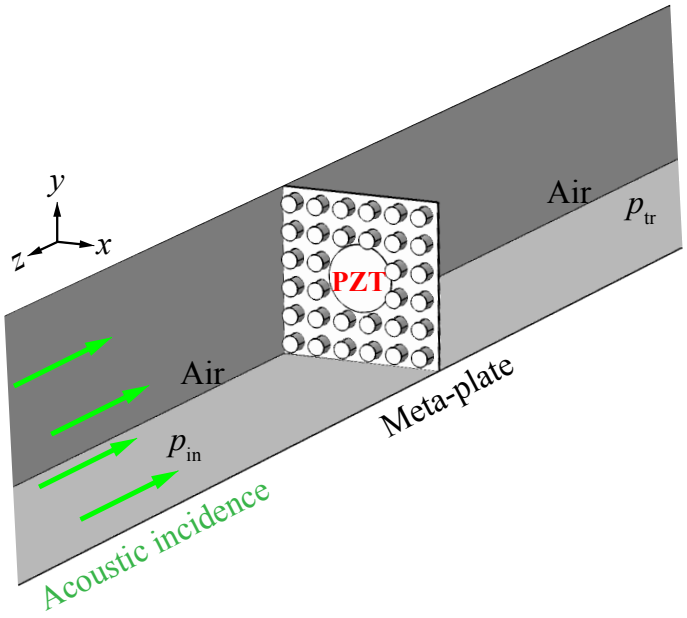

Figure 2.1 – The scheme diagram of the planar AEH system.

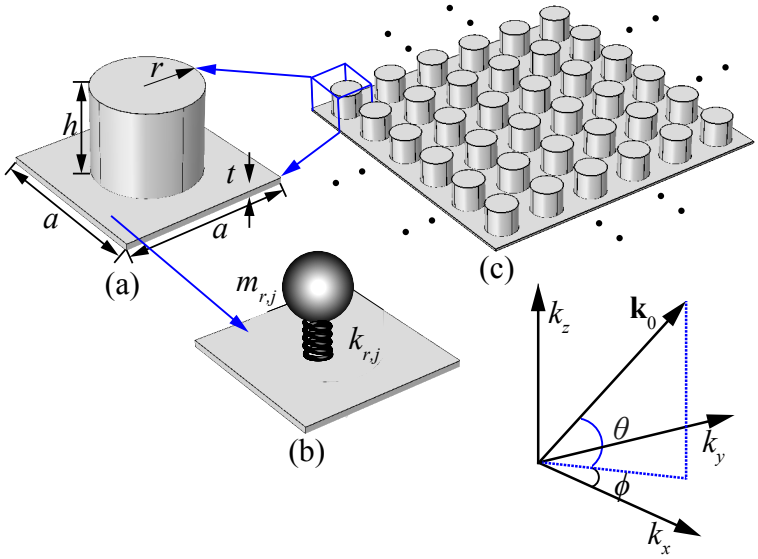

Figure 2.2 – The schematic of the stub-plate AMM.

N stubs can construct a unit cell. The cycle of a stub (Fig. 2.2(a)) from the infinite periodic array (Fig. 2.2(c)) is a and the thickness of the plate is t. Generally, several such stubs (N) can construct a unit cell.

A single stub can be modeled to be a mass-spring resonator (Fig. 2.2(b)). Therefore, the structure can be represented as a thin plate with infinite mass-spring resonators. The spring constant and mass of the jth resonator are $m_{r,j}$ and $k_{r,j}$, respectively. The damping of the system can be considered by introducing a complex spring constant $k_{r,j}(1+i\eta_{r,j})$, with $\eta_{r,j}$ the loss coefficient.

Considering an oblique and time-harmonic acoustic plane wave p_{in} with an elevation and an azimuth angle θ and ϕ, the incident acoustic pressure can be expressed below,

$$p_{\text{in}} = p_0 \mathrm{e}^{-i(k_x+k_y+k_z)} \mathrm{e}^{i\omega t}, \tag{2.1}$$

where p_0, ω and k are the amplitude, angular frequency and wave vector of the incident wave, respectively. The wavenumber vectors along x, y, z directions can be correlated with the incident angle as below,

$$k_x = k_0 \sin(\theta)\cos(\phi), k_y = k_0 \sin(\theta)\sin(\phi), k_z = k_0 \cos(\phi), k_0 = \omega/c_0, \tag{2.2}$$

where c_0 is the sound speed in air. To better characterize plane wave in $x-y$ plane, x and y of the position vector and the wavenumber vector are integrated as $\mathbf{r} = (x, y)$ and $\mathbf{k} = (k_x, k_y)$. Taking the modified terms, the incident sound pressure can be revised as

$$p_{\text{in}} = p_0 \mathrm{e}^{-i\mathbf{k}\cdot\mathbf{r}} \mathrm{e}^{-ik_z z} \mathrm{e}^{i\omega t}, \tag{2.3}$$

The acoustic waves impinging on the plate system are split into reflected and transmitted waves along z-axis, which can induce the harmonic vibration of the plate. With omitting the time factor $\mathrm{e}^{i\omega t}$, the vibration of the thin plate can take the following form as

$$\begin{aligned} D\,\nabla^4 w(\mathbf{r}) - \rho t \omega(\mathbf{r}) = p_{\text{in}}(\mathbf{r}, z))_{z=0} + p_{\text{re}}(\mathbf{r}, z)_{z=0} - p_{\text{tr}}(\mathbf{r}, z)_{z=0} \\ + \sum_{j=1}^{N} \sum_{\mathbf{R}} (f_j + \mathbf{R}) \delta[\mathbf{r} - (\mathbf{r}_j + \mathbf{R})], \end{aligned} \tag{2.4}$$

where $D\nabla^4 = (\partial^2/\partial x^2 + \partial^2/\partial y^2)^2$, $w(\mathbf{r})$ represents the transverse displacement of

the plate, and p_{re}, p_{tr} are the reflected and transmitted sound pressure. The plate bending stiffness is $D = Et^3/12(1-\nu^2)$, with E, t, ν the Young's modulus, thickness of the plate, and Poisson's ratio, respectively. The basis vector of the attached position for each resonator is $\mathbf{R} = m\mathbf{a}1 + n\mathbf{a}2$, with m and n integers. The term $f_j(\mathbf{r}_j + \mathbf{R})$ stands for the force exerted by the resonator at $\mathbf{r}_j + \mathbf{R}$.

Because of the periodic condition of the resonate system, the displacement response of the plate can be given by

$$w(\mathbf{r}) = \sum_{\mathbf{G}} W_{\mathbf{G}} \mathrm{e}^{-i(\mathbf{k}+\mathbf{G})\cdot\mathbf{r}}, \tag{2.5}$$

where $G = m\mathbf{b}1 + n\mathbf{b}2$ is defined as the reciprocal-lattice vector. m and n are integers, and $\mathbf{b}1$ and $\mathbf{b}2$ are basis vectors. $W_{\mathbf{G}}$ is displacement coefficient. Likewise, the reflected and transmitted waves can be expressed as

$$p_{\mathrm{re}}(\mathbf{r}, z) = \sum_{\mathbf{G}} p_{\mathrm{re},\mathbf{G}} \mathrm{e}^{-i(\mathbf{k}+\mathbf{G})\cdot\mathbf{r}} \mathrm{e}^{+ik_{z,\mathbf{G}}z}, \tag{2.6}$$

and

$$p_{\mathrm{tr}}(\mathbf{r}, z) = \sum_{\mathbf{G}} p_{\mathrm{tr},\mathbf{G}} \mathrm{e}^{-i(\mathbf{k}+\mathbf{G})\cdot\mathbf{r}} \mathrm{e}^{-ik_{z,\mathbf{G}}z}, \tag{2.7}$$

where

$$k_{z,\mathbf{G}} = \begin{cases} \sqrt{k_0^2 - |\mathbf{k}+\mathbf{G}|^2}; k_0^2 \geq |\mathbf{k}+\mathbf{G}|^2 \\ \sqrt{k_0^2 - |\mathbf{k}+\mathbf{G}|^2}; k_0^2 < |\mathbf{k}+\mathbf{G}|^2. \end{cases} \tag{2.8}$$

Based on the periodicity of the resonators, the resonator force term in Eq. 2.4 can be expanded in Fourier series form as

$$\sum_{\mathbf{R}} f_j(\mathbf{r}_j + \mathbf{R})\delta[\mathbf{r} - (r_j + \mathbf{R})] = f_j(\mathbf{r}_j)\frac{1}{S}\sum_{\mathbf{G}} \mathrm{e}^{i(\mathbf{k}+\mathbf{G})\cdot\mathbf{r}_j} \mathrm{e}^{-i(\mathbf{k}+\mathbf{G})\cdot\mathbf{r}}, \tag{2.9}$$

where S is the area of the unit cell in terms of periodic lattice.

The force bending stiffness $D_{r,j}$ of the unit cells and the force $f_j\mathbf{r}_j$ induced by

the resonators can be correlated as

$$D_{r,j} = \frac{-\omega^2 m_{r,j}}{1-\omega^2/[\omega_{r,j}^2(1+i\eta_{r,j})]}; f_j(\mathbf{r}_j) = -D_{r,j}w(\mathbf{r}_j). \tag{2.10}$$

At the air-plate interface, the momentum conservation requires

$$\frac{\partial[p_{\text{in}}(\mathbf{r},z)+p_{\text{re}}(\mathbf{r},z)]}{\partial z}|_{z=0} = \frac{\partial[p_{\text{tr}}(\mathbf{r},z)]}{\partial z}|_{z=0} = \rho_0\omega^2 w(\mathbf{r}). \tag{2.11}$$

The reflected and transmitted sound pressure coefficients for each $\mathbf{G}$ is

$$p_{\text{re},\mathbf{G}} = p_0\delta_{\mathbf{0}-\mathbf{G}} - \frac{i\rho_0\omega^2}{k_{z,\mathbf{G}}}W_{\mathbf{G}}, \tag{2.12}$$

and

$$p_{\text{tr},\mathbf{G}} = \frac{i\rho_0\omega^2}{k_{z,\mathbf{G}}}W_{\mathbf{G}}, \tag{2.13}$$

Plugging Eqs. 2.3, 2.5-2.7 and 2.9 into Eq. 2.4, the following equation can be obtained:

$$\begin{aligned}\{DS[(\mathbf{k}+\mathbf{G})_x^2+(\mathbf{k}+\mathbf{G})_y^2]^2 + i\omega(2\rho_0\omega S/k_{z,\mathbf{G}}) - \omega^2\rho tS\}W_{\mathbf{G}} \\ + \sum_{j=1}^{N}\sum_{\mathbf{G}'} W_{\mathbf{G}'}D_{r,j}e^{-i\mathbf{G}'\cdot\mathbf{r}_j}e^{i\mathbf{G}\mathbf{r}_j} = 2p_0S\delta_{\mathbf{0}-\mathbf{G}}.\end{aligned} \tag{2.14}$$

The coefficients of the reciprocal-lattice vectors are set as $m = n = [-M,...,M]$ for $\mathbf{G}$ and $\mathbf{G}'$, and the number of plane waves sampled for the calculation is $n = (2M+1)^2$. The above equation can be simplified in a matrix form as

$$([\mathbf{K}_p] + i\omega[\mathbf{C}_f] - \omega^2[\mathbf{M}_p] + [\mathbf{D}_r])\{\mathbf{W}_{\mathbf{G}}\} = 2p_0S\{\delta_{\mathbf{0}-\mathbf{G}}\}, \tag{2.15}$$

where the plate stiffness and fluid loading matrices are $\mathbf{K}_p$ and $\mathbf{C}_f$, and the mass and dynamic stiffness matrices of the resonators are $\mathbf{M}_p$ and $\mathbf{D}_r$. Considering

the wave propagating in air, the sound transmitted loss (STL) is defined by[142]

$$\mathrm{STL(dB)} = 20\log_{10}(p_{\mathrm{in}}/p_{\mathrm{tr}}). \tag{2.16}$$

The displacement coefficients $W_{\mathbf{G}}$ can be obtained from Eq. 2.15. Combining Eqs. 2.12, 2.13 and 2.16, the general STL of the planar meta-structure can be resolved.

The above acoustic-structural airborne analyses characterize the overall property of the planar metamaterial in terms of sound transmission spectrum. In addition to the airborne analysis, the band structure analyses of solid materials are essential for understanding the vibration of elastic system. Considering the sheer structural analysis, the governing equation of wave propagation in a solid plate based on Kirchhoff plate theory can take from Eq. 2.4 as

$$D\,\nabla^4 w(\mathbf{r}) - \rho t\omega(\mathbf{r}) = \sum_{j=1}^{N}\sum_{\mathbf{R}}(f_j + \mathbf{R})\delta[\mathbf{r} - (r_j + \mathbf{R})]. \tag{2.17}$$

Considering the force applied by each resonator in the super-cell, the following relation can be obtained

$$f_j(\mathbf{r}_j) = -k_{r,j}[u(\mathbf{r}_j) - w(\mathbf{r}_j)] = -\omega^2 m_{r,j} u(\mathbf{r}_j), \tag{2.18}$$

where $u(\mathbf{r}_j)$ and $k_{r,j}$ are the displacement and stiffness of the mass resonators at the position $\mathbf{r}_j$. For the band structure calculation, the damping of the plate is reasonably neglected in Eq. 2.18 for simplification.

By inserting the Eqs. 2.5 and 2.9 into Eqs. 2.17 and 2.18, the governing equation of wave propagation in plate can be obtained

$$DS[(\mathbf{k}+\mathbf{G})_x^2 + (\mathbf{k}+\mathbf{G})_y^2]^2 W_{\mathbf{G}} + \sum_{j=1}^{N} k_{r,j}\left(\sum_{\mathbf{G}'} W_{\mathbf{G}'} \mathrm{e}^{-i(\mathbf{K}+\mathbf{G}')\cdot\mathbf{r}_j} - U_{\mathbf{G}}\right)\mathrm{e}^{i(\mathbf{k}+\mathbf{G})\cdot\mathbf{r}_j} = S\rho t\omega^2 W_{\mathbf{G}} \tag{2.19}$$

where

$$k_{r,j}\left(\sum_{\mathbf{G}'} W_{\mathbf{G}'} e^{-i(\mathbf{K}+\mathbf{G}')\cdot\mathbf{r}_j} - U_{\mathbf{G}}\right) = m_{r,j}\omega^2 U_{\mathbf{G}}. \tag{2.20}$$

The eigenvalues and band structures could be acquired by solving the Eqs. 2.19 and 2.20.

2.3 Implementation of the planar AMM

Band gaps of the periodic structures could be applied for wave guiding and confinement through introducing defect modes inside. Defect mode in the band gap can be created by breaking the periodicity of the perfect structures. At the defect mode frequency, the propagating waves are localized in the defect region, which leads to the strain energy confinement. The defect mode in a larger band gap contributes to a stronger energy confinement effect. According to the theoretical analyses in Sec. 2.2, the STL and band structure of the periodic plate metamaterial can be acquired. Through adjusting the mass and the dynamic stiffness of the resonators, and the fluid loading and plate stiffness, the band structure can be modified or optimized for wider band gap and larger quality factor of the defect mode.

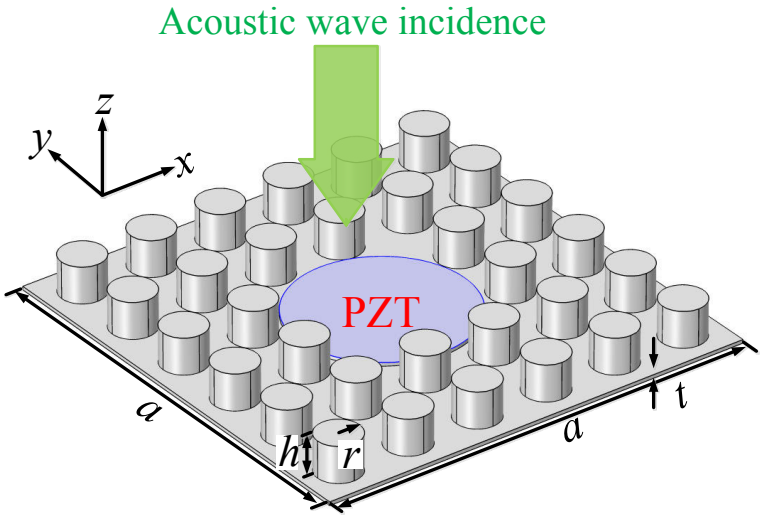

Figure 2.3 – A defected super cell of the planar metamaterial for AEH.

As illustrated in Fig. 2.3, a supercell composed of 6 by 6 resonators is considered, and four of them are removed to create a defect. The fluid loading, i.e., acoustic wave incidence, impinges along z direction and a PZT patch is attached to the defected cavity to convert the localized strain energy into electricity. The proposed planar metamaterial can be also numerically modeled and simulated by finite element method (FEM). Since an infinite structure is assumed in x - y plane, Bloch - Floquet periodic boundary conditions are employed for connections in x and y directions. With referring to the theoretical analyses and the corresponding numerical validation, the repeated cycle of the supercell, the geometries are optimally tuned for the best energy confinement performance. The radius and height of the rubber stubs, and the thickness of the aluminum plate are set to be $a = 60$ mm, $r = 3$ mm, and $h = 5$ mm, $t = 0.4$ mm, respectively.

Parameters	Silicone rubber	Aluminum
Density (kg/m^3)	1300	2700
Young's modulus (MPa)	1.89	7×10^4
Poisson ratio	0.4998	0.33

Table 2.1 – Parameter values of materials in calculations.

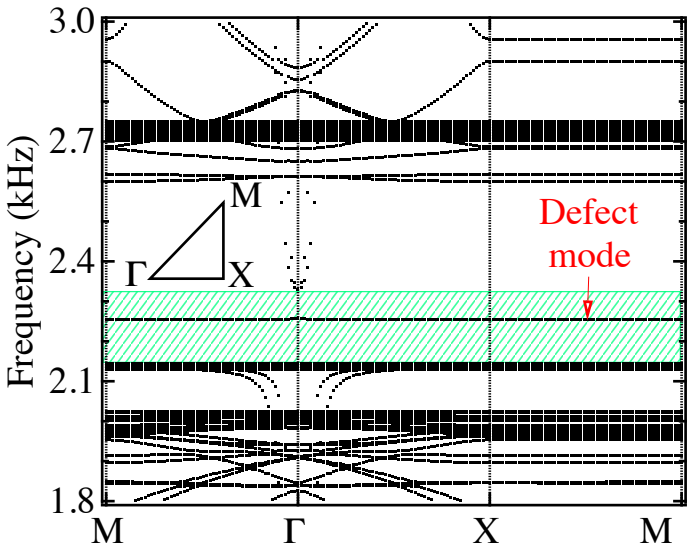

Figure 2.4 – Band structure of the defected supercell in the frequency range (1.8 - 2.5 kHz).

Commercial FEM software COMSOL Multiphysics™ Version 5.2 is utilized to analyze and simulate the perfect and defected supercell shown in Fig. 2.3. Pressure acoustics, solid mechanics and electrostatics modules are applied for the coupling of the acoustic, mechanical and electrostatic fields. The band structure of the supercell is computed with considering the structural effect of the PZT patch. The parameters of aluminum plate and rubber silicone stubs for computation are listed in Table 2.1. The geometries of the defect and supercell are optimized with considering the band gap and the coupling effect of adjacent defects. Figure 2.4 presents the band structure of the defected AMM structure along the directions of the first irreducible Brillouin zone. A complete acoustic band gap illustrated as the shaded area in Fig. 2.4 is obtained in the frequency range 2144 - 2331 Hz. A flat defect mode with frequency around 2254 Hz (dotted line in the shadow) is achieved after creating the defect and adding the PZT patch in the perfect supercell, which opens a gate of transmission in the gap and provides the possibility of energy confinement.

In order to further validate the acoustic model, an acoustic plane wave incidence with a sound pressure of 2 Pa (100 dB) is considered and STL curves of the AMM system with and without defect are depicted as a blue line with symbols and a black line in Fig. 2.5, respectively.

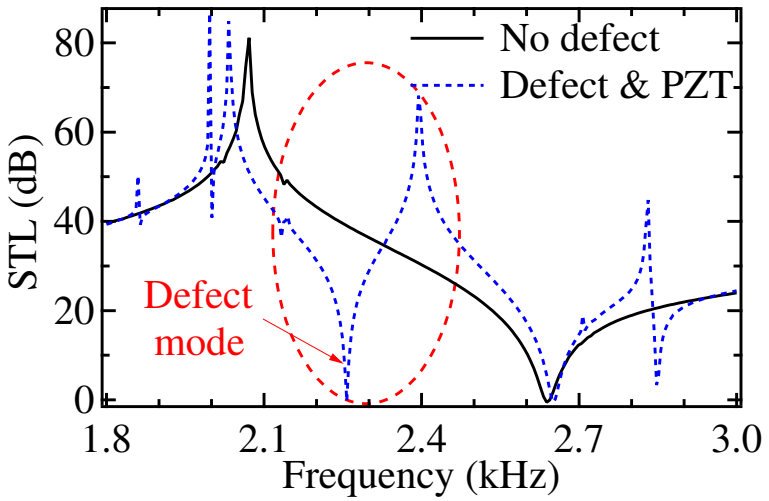

Figure 2.5 – STLs of the planar AMM with and without defect.

It can be seen in Fig. 2.5 that the defect mode (see the dashed blued curve)

with the frequency of 2257.5 Hz shows high sound transmission (STL ≈ 0) in the band gap as expected, while the transmission maintains low under no defect condition (refer to the black line). It is worth noting that there is another mode (2847.5 Hz) generated by the defect beyond the band gap with high transmission (STL = 3.3 dB), which also possesses the capability of energy confinement.

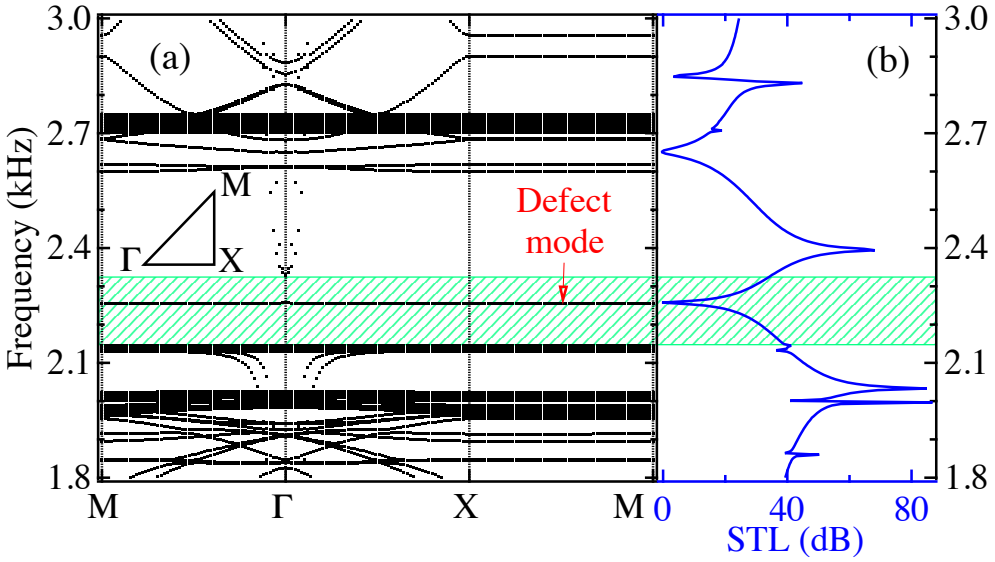

Figure 2.6 – Band structure and STL of the defected AMM.

Both STL and band structure of the defected AMM are presented and corresponded to mutually validate the vibrating behaviors of the AMM in Fig. 2.6. The opening and close of the full band gap illustrated in Fig. 2.6(a) correspond well with the resonance and anti-resonance from STL in Fig. 2.6(b). The defect mode appears at the same frequency under both the structural-borne and airborne analysis.

At the frequency of the defect mode, strong strain energy confinement can be readily observed and most of the energy is centralized in the defect region as illustrated in Fig. 2.7.

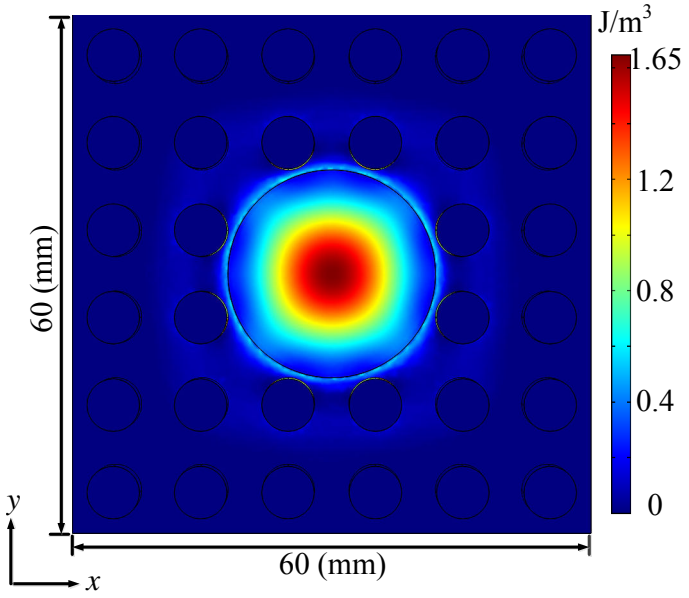

Figure 2.7 – Strain energy distribution of the planar AMM at the defect mode.

The concentrated energy density can be up to 1.65 J/m^3, and the strain energy directly determines the output power of the PZT circuit. The confined elastic strain energy in the planar AMM can be expressed as below,

$$E_s = \frac{1}{2}\sum_{ijkl} c_{ijkl} S_{ij} S_{kl}, \tag{2.21}$$

where c_{ijkl} is the elastic stiffness tensor, and $S_{ij} and S_{kl}$ are the strains. The confined strain energy can be converted into electrical energy through the attached PZT patch and the loading circuit. The details will be discussed in the following Section.

2.4 Electrical model

As illustrated in Fig. 2.8(a), a PZT-5H patch connecting to an electric circuit is attached to the defected area for the energy conversion part. In order to efficiently and effectively pick up the confined strain energy, the geometries of the circular PZT-5H patch need to be optimized.

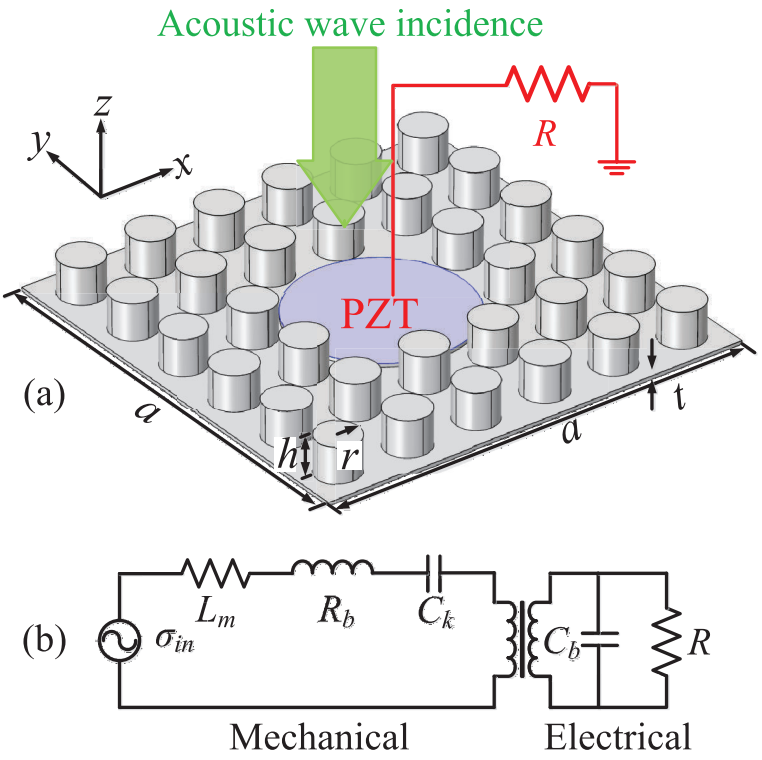

Figure 2.8 – The planar AEH system and the equivalent circuit. (a) Sketch of AEH system composed of a supercell and a piezoelectric patch. (b) Equivalent circuit representation of the AEH system.

The piezoelectric patch should be light enough to minimize the mass effect to the system, yet large enough to completely cover the strain energy confined area. Specifically, the radius is sufficiently swept and set to be 12 mm with a small thickness of 0.2 mm for the maximum output voltage. Moreover, the structural resonance of the patch is checked to well match the defect mode. The incident acoustic waves interact with the defected plate AMM variously with the frequencies. Most of the waves are reflected at the band gaps, and coupled with the meta-structure at defect mode or other resonating modes. An equivalent circuit for mechanical and electrical parts of the AEH system is presented in Fig. 2.8(b), where σ_{in}, L_{m}, R_{b}, C_{k}, C_{b} and R represent the confined stress, system mass, mechanical damping, mechanical stiffness, capacitance of the PZT patch and the load resistance, respectively (cf. in Table A.1). The piezoelectric energy conversion model illustrated in Fig. 2.8(b), developed by S. Roundy and P. K.

Wright[143], is applied. The output voltage of the resistive load R is given as,

$$V = \frac{j\omega \frac{2c_p d_{31} t}{\varepsilon}}{j\omega(\omega^2 k_{31}^2 + \frac{2\xi\omega}{RC_b}) - 2\xi\omega^3} \frac{A_{in}}{k}, \tag{2.22}$$

where $\frac{c_p d_{31}}{\varepsilon}$ and $k_{31}^2 = \frac{c_p d_{31}^2}{\varepsilon}$ are the piezoelectric coupling coefficient terms, with k, A_{in}, ξ and ω the geometric constant, scavenged vibration acceleration, mechanical damping and driving angular frequency, respectively. The capacitance and the density of the piezoelectric patch are 0.43 nF and 7500 kg/m^3. The coupling coefficient k_{31} and the mechanical damping ratio ξ are 0.36 and 0.015, respectively. The root mean square (RMS) power P can be readily transferred as $|V|^2/2R$, and the optimal load resistance for maximum output P can be acquired as,

$$R_{opt} = \frac{1}{\omega C_b} \frac{2\xi}{\sqrt{4\xi^2 + k_{31}^4}}. \tag{2.23}$$

Electrostatic module for electromechanical coupling is conducted and a floating potential boundary is set for the upper layer of the PZT patch. The frequency of incident sound is swept to obtain the maximum output electrical potential on the PZT patch.

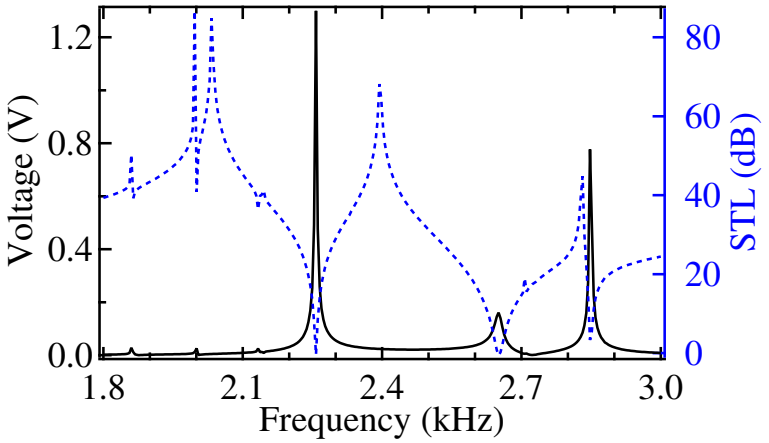

Figure 2.9 – Output voltage magnitude and corresponded STL as functions of frequency.

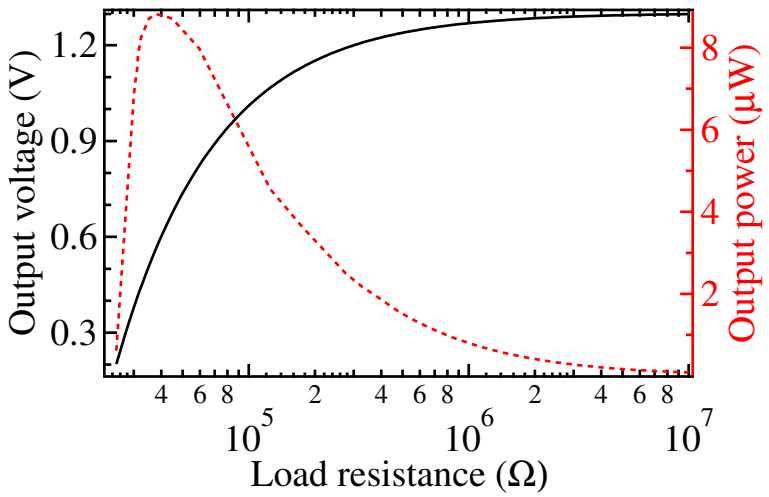

Figure 2.10 – Output voltage magnitude and power versus the load resistance.

In Fig. 2.9, the solid line shows the voltage magnitude of the PZT patch as a function of frequency, and the voltage magnitude peaks of 1.3 V and 0.78 V are obtained at the frequency of 2257.5 Hz and 2847.5 Hz, respectively, which correspond precisely with the defect mode and the other resonant mode illustrated in STL (the blue dash line). The defect mode of 2257.5 Hz exhibits strong energy confinement capability and thus high output voltage, and the peak at 2847.5 Hz results from the other resonant mode.

As given in Eq. 2.22, the output voltage is a function of the resistive load. A circuit module is connected to the floating potential terminal to calculate the output electrical voltage and power. R is constantly swept at the frequency of the defect mode to determine its value producing the optimal generated power. As shown in Fig. 2.10, the output voltage and power increase rapidly with the increase of R, and then the power reaches its maximum value at $R = 38$ kΩ and then decreases with increasing R, while the voltage remains increasing until becoming flat. The optimized load resistance R_{opt} can be also determined from Eq. 2.23, and the value is calculated to be 37.8 kΩ with the relative parameters provided above, which validates the electrical simulation. The maximum output voltage V_{out} and power W_{out} are 1.3 V and 8.8 μW, respectively. Considering the geometries of the whole AEH system, the obtained power density is around 0.54 μW/cm^3 with 2 Pa acoustic incidence at the frequency of 2257.5 Hz. The energy

conversion efficiency η_e can be acquired by calculating the ratio of input sound energy and the output electrical energy W_s as below

$$\eta_e = \frac{W_{out}}{I_{in} S}, \tag{2.24}$$

where S is the area of the system in $x-y$ plane. In the case of incident waves with sound pressure of 2 Pa and the output power of 8.8 μW, the energy harvesting efficiency of the system is around 0.24.

2.5 Discussion and conclusion

In summary, applying the properties of the acoustic band gap and the defect mode for wave localization of AMMs, an acoustic energy harvester based on a planar AMM with piezoelectric material has been realized and analyzed. For the stub-plate AMM structure, the coupling between the Lamb and stub modes is very weak and the localized modes in the rubber stubs occur at relatively low frequencies, leading to strong localization in the stub and thus large strain energy confinement in the defected region. A PZT-5H patch with a load circuit is applied to convert the strain energy into electrical energy. The maximum output voltage and power of 1.3 V and 8.8 μW are acquired with an acoustic incidence of 2 Pa at a frequency of 2257.5 Hz. The output power would increase with the acoustic incidence and the coupling coefficient of the PZT patch. A sound to electrical energy conversion efficiency of 24% is obtained from the planar AMM system with the locally optimized system configuration. The current system only considers a 6 by 6 square matrix as a supercell with a defect of four resonators. The shape, area and the size of supercell and defect configurations of the AMM can be varied and tuned to further improve the AEH efficiency from the aspect of the acoustic-structural coupling. Meanwhile, our AEH system shows in Fig. 2.5 a high STL of 40 dB in the band gap excluding the defect mode, which greatly favors its application in sound insulation. Our AEH system maintains valid and effective for acoustic waves with oblique incidence from -$\pi/3$ to $\pi/3$, while the efficiency reduces with larger incident angles. Because the defect mode mechanism is applied, the AEH system is born with narrow band property.

Compared with the existing AEH systems based on piezoelectric effects listed in Table A.2 abstracted from the review paper on AEH[135], the innovative system proposed here excels in competitive power density and construction simplicity. The thickness of the system is around 1/28 of the wavelength. The proposed planar AEH system exhibits the advantages of high power efficiency, small dimensions at relatively low frequencies, easy fabrication and tough durability, which can achieve both sound insulation and energy harvesting in various applications.

Nous devons avoir la persévérance, surtout la confiance en nous-même. Notre talent est utilisé pour réaliser quelque chose et on doit la réaliser à n'importe quel prix.

Marie Curie

Chapter 3

Multilateral metasurfaces for AEH

Contents

Metamaterial-based acoustic wave manipulation shows great potential in effective acoustic energy confinement and low-frequency acoustic isolation. We numerically and theoretically propose in this chapter a concept based on multilateral metasurfaces for reflected acoustic focusing and energy harvesting. The

theoretical phase-shift profile required for reflected wave focusing and governed by the generalized Snell's law can be discretely realized by appropriately arraying the labyrinthine units in the right sequences. Based on this design, multilateral metasurfaces for acoustic wave focusing and energy confinement under point-source incidence are considered and sufficiently investigated. The coupling effects and multiple reflections between or among metasurfaces, which play a significant role in the energy confinement, are initially analyzed and discussed. We show that the acoustic focusing and confinement increase with the sides of the multilateral metasurfaces as anticipated. In addition to the contribution of the first reflection, multiple reflections also contribute to the acoustic focusing and energy confinement, especially when the metasurfaces are configured in parallel. The proposed multilateral metasurfaces should have excellent performance in acoustic energy confinement in various situations due to the variable designs and strong acoustic focusing capabilities. Subsequently, an innovative acoustic energy harvester based on acoustic multilateral metasurfaces and a piezoelectric bimorph are proposed. The acoustic energy confined by the metasurfaces from a point source is converted into electrical energy by a structured piezoelectric bimorph. Numerical simulations and theoretical analysis evidenced that the output voltage and power drastically increase with the sides of the multilateral metasurfaces energy harvesting system. Maximum output voltage and power 52 and 407 times higher than those under the case without metasurfaces are achieved with enclosed multilateral metasurface design.

3.1 Introduction

Energy harvesting from ambient environments has intrigued scientists as well as engineers recently with the advances in low-power electronic designs. As a kind of clean, ubiquitous and renewable form of energy, sound or noise may act as a promising sustainable power source for energy production and microautonomous devices, such as wireless sensors, mobile electronics and so forth. Even though sound abundantly exists in industrial and domestic environments, its energy densities in ordinary surroundings are relatively low compared to other ambient energy sources [133, 144, 145], and, thus, sound or noise generally

needs to be focused or confined through effective conversion media for better acoustic energy harvesting (AEH). Intuitively, classical Helmholtz [120] and other chamber resonators [119, 136] can be used to enhance the acoustic confinement and subsequently realize AEH. Li *et al*. [136] utilized a quarter-wavelength straight-tube resonator to form and harvest the standing sound wave inside, and the work frequency heavily depends on the geometrical sizes of the tube [136]. In general, the strategy based on resonators suffers from a defect of the bulky structures and uncontrolled wave field, thus hampering the applicable energy harvesting.

In a different context, the recent emergence of artificially engineered acoustic metamaterials (AMMs) [30, 39, 44, 71, 146] has significantly broadened the horizon of acoustic wave manipulations. AMMs possess anomalous properties and capabilities, paving new avenues to achieve fascinating phenomena, such as subdiffraction imaging [147, 148], extraordinary acoustic transmission [149, 150], one-way propagation [54, 63], cloaking [49, 50], superabsorption [55, 151], and AEH [140]. As a category of AMMs, acoustic metasurfaces [74, 77, 152, 153] or metascreens [87, 154, 155] exhibit great capabilities on the wave-front manipulations. Because of the ultrathin planar features and fully controlled phase shift, metasurfaces have been rapidly extended to unidirectional transmission [73, 90, 93], perfect absorption [108], lenses [153, 156], cloaking [157–159], etc. To maintain the subwavelength-thickness property and desired phase shift, metasurfaces generally utilize the concept of coiling up space to control the effective acoustic paths, which can ensure the predefined phase lead or lag for desired wave-front tailoring. Even though the metasurfaces can tailor the wave front in various ways, few studies of acoustic metasurfaces have emphasized on the aspect of acoustic energy confinement and harvesting. Therefore, the achievement of energy confinement or harvesting with multilateral metasurfaces, if realized, should solve the drawbacks of using conventional resonators and open degrees of freedom for acoustic energy control and recycling.

To this end, we theoretically and numerically propose in this chapter a concept based on multilateral metasurfaces for acoustic focusing and energy harvesting. A series of labyrinthine elements, yielding fully controlled phase shift, are employed to construct the metasurfaces [74, 77]. Different from or-

dinary flat acoustic metasurfaces, multilateral metasurfaces are partially or completely enclosed boxlike metasurfaces, which can catch more impinging acoustic waves, thus contributing to higher acoustic confinement, especially when a point acoustic source is considered. It is worth stressing that the coupling effects and multiple reflections between/among metasurfaces, existing in the proposed multilateral metasurfaces, have never been explored or investigated. These effects and phenomena can be essential to the design of the multilateral metasurfaces specified in acoustic focusing and energy confinement. Therefore, multilateral metasurfaces with various geometrical configurations and different extent of enclosure are analyzed and simulated in great detail. Because of the fully controllable wave field and the planar features, the partially or enclosed multilateral AMs, together with a piezoelectric bimorph energy converter, are unprecedentedly applied for effective and efficient AEH. The idea is to arbitrarily focus and confine the acoustic waves from a point sound source by the multilateral AMs at any designed position, and subsequently convert the confined acoustic energy into electrical energy through a piezoelectric cantilever bimorph system. The proposed AEH system based on multilateral AMs and piezoelectric bimorph converter can be effectively applied to power public or private micro/nano devices in a variety of partially or completely enclosed space environments, such as noisy plants, offices, streets, and so forth.

The multilateral metasurfaces proposed here provide an innovative idea for acoustic focusing and energy harvesting. The designs can be applied to efficient and effective AEH in partially or completely enclosed spaces with a variety of occasions.

3.2 Space coiling elements

Metasurfaces made up of a variety of unit cells, such as Helmholtz resonators [87] and labyrinthine chambers [82], have demonstrated extraordinary wavefront shaping capabilities. In this chapter, different labyrinthine unit cells are utilized as candidates to manipulate the phase of reflected waves by coiling up space. The shifted phase of the reflected waves controlled by each unit is crucial to achieve desired reflected field. A sample labyrinthine unit (length l_x and width

l_y) of the case (m, n) = (3, 2) is illustrated in Fig. 3.1, with m and n referring to the number of the identical bars (length l and width w) in upper and lower boundaries, respectively. The identical and parallel bars, arrayed with equal space d in the upper and lower boundaries of a unit, construct a zigzag channel to realize space coiling for effective sound path control, and the left end of the unit is set as hard boundary.

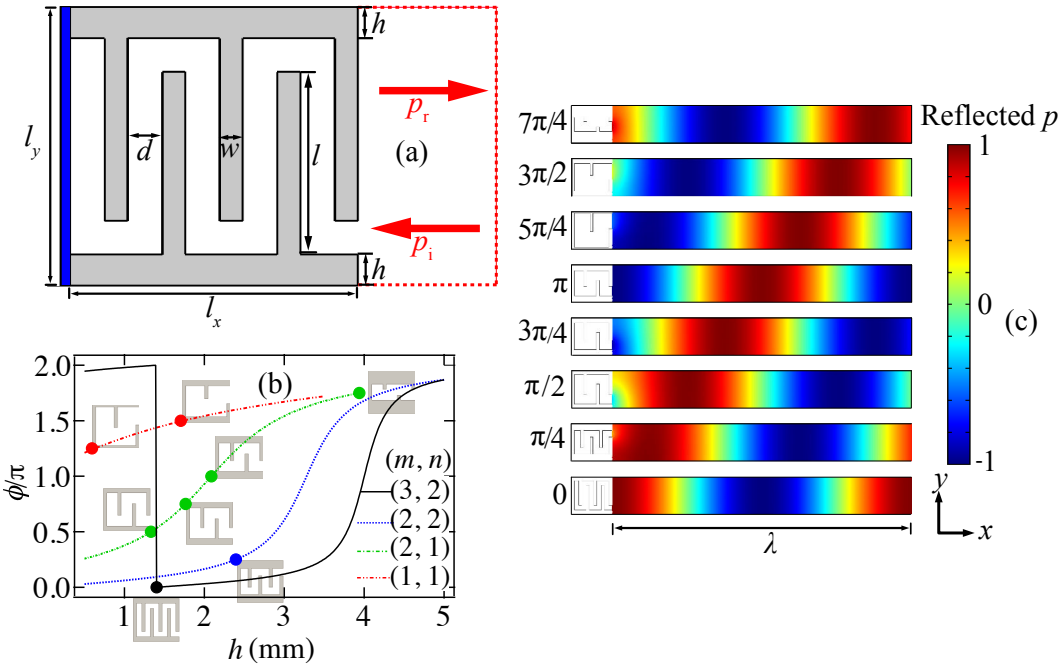

Figure 3.1 – Labyrinthine elements and phase shifts. (a) Schematic diagram of a typical labyrinthine unit (width l_x and length l_y) of the case (m, n) = (3, 2), with m and n referring to the number of the identical bars (width w and length l) in upper and lower boundaries, respectively. d is the gap width between any two bars and and t is the thickness of the upper and lower boundary plates. (b) Four phase towards thickness h evolution curves corresponding to labyrinthine units with four different (m, n) configurations. Eight units with individual phase shift (solid circles) are carefully chosen to continuously cover the phase range from 0 to 2π with a step of $\pi/4$ for the minimum viscosity loss. (c) Normalized reflected sound pressure field evolutions of the eight labyrinthine elements from the four different configurations.

According to geometrical relations shown in Fig. 3.1(a), the length of the bars and the width of the channel can be readily expressed as $l = l_y - 2t - d$ and

$d = l_x/(m+n) - w$, respectively. As theoretically and experimentally validated in previous study [74], the thickness of the upper/lower plates h and the number of bars (m, n) are the two essential configurable parameters to achieve the full 2π range phase shift and maintain planar properties as well. The work frequency and sound velocity in air for all the simulations and theoretical analysis in this chapter are set as 3430 Hz and 343 m/s, respectively, and thus the wavelength is $\lambda = 0.1$ m. The parameters l_x and l_y are fixed to be 0.0125 m ($\lambda/8$) for all the units to ensure subwavelength property of the whole structure, and w of all bars is fixed to be 1 mm ($\lambda/100$). Therefore, the space of the zigzag channel can be sufficiently adjusted at will by changing the parameters (m, n) and h. As illustrated in Fig. 3.1(b), units of four groups (1, 1) red dash dotted line, (2, 1) green dash dotted line, (2, 2) blue dashed line and (3, 2) black solid line) with a varying h from 0.5 mm to 5 mm ($\lambda/200$ to $\lambda/20$) for phase shift are proposed and well investigated. From the phase evolution curves of the groups in Fig. 3.1(b), the phase shift range that a group can cover increases with the number of the bars (sum of m and n), and the introduce of the bars improves the parameter h's effectiveness in phase shifting. It can be also readily observed that the units in group (3, 2) (black line) can completely realize the phase shift within the full 2π range. However, in real applications, the number of barrier bars of the units should be minimized to avoid potential viscosity loss and airborne dissipation (see Sec. 3.4 for details).

Therefore, eight labyrinthine units (see the solid cycles in Fig. 3.1(b)) with less bars are optimally selected to sufficiently cover the phase shift of the 2π range with a resolution of $\pi/4$. Through numerical simulation, the phase shift performances of all the eight selected labyrinthine units are individually investigated and consistently demonstrated in Fig. 3.2(c). As shown in the latter, the incident waves are impinging from the right ends, and the reflected sound pressure fields with one wavelength (0.1 m) formed by the left labyrinthine units are normalized to each maximum value. Viewing from the bottom to the top of Fig. 3.2(c), the selected labyrinthine units gradually and completely shift the phase of the reflected waves from 0 to 2 π range with a fine discrete resolution of $\pi/4$ as designed and desired. Compared with other common anisotropic metamaterials in wavefront manipulation, the proposed labyrinthine units can

provide higher refractive index and therefore smaller geometrical dimension ($\lambda/8$), which favors the planar design of metasurfaces.

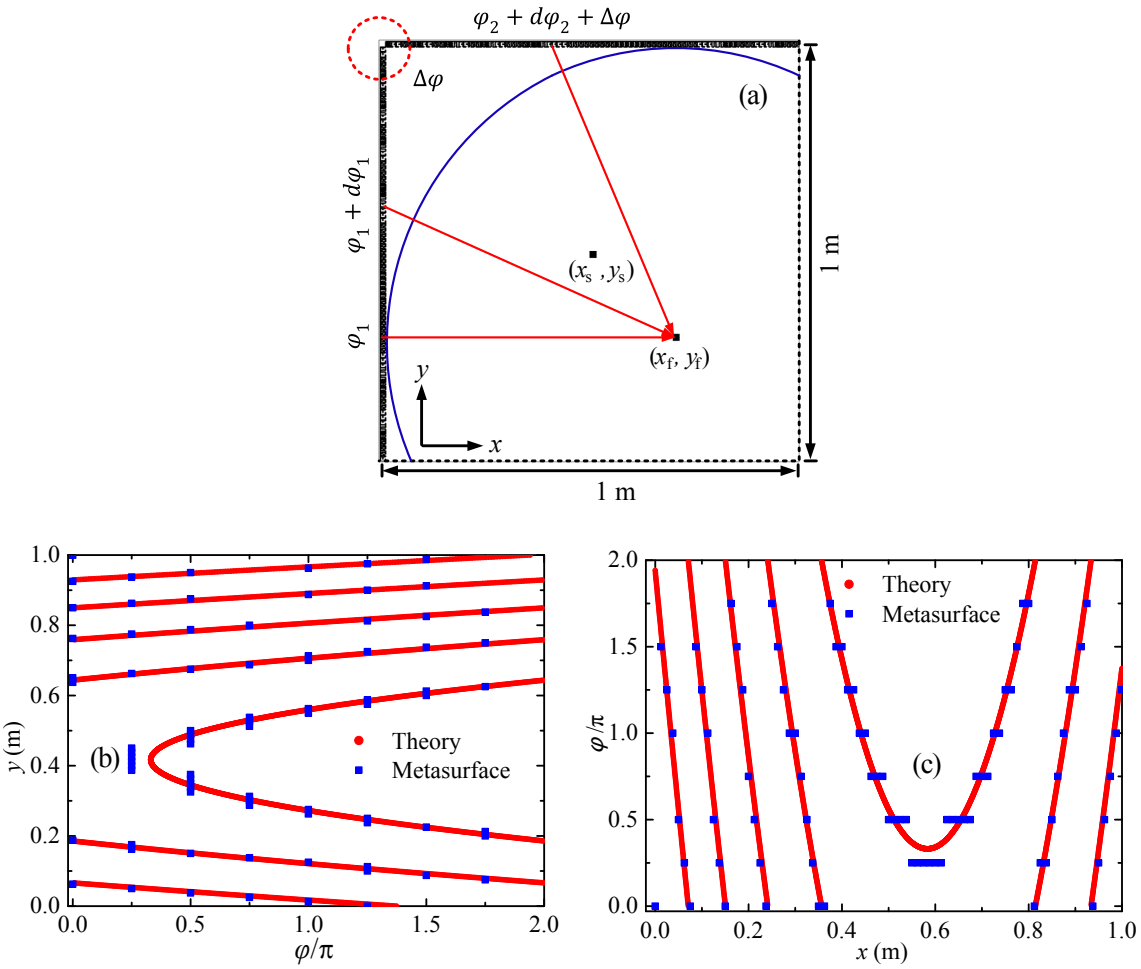

Figure 3.2 – Schematic of acoustic confinement and the required phase distributions. (a) Schematic illustration of a partially enclosed metasurface structure composed of two perpendicular metasurfaces designed for the acoustic confinement at arbitrary focusing position (x_f, y_f) in an acoustic field with a point source (x_s, y_s) centring at (0.5 m, 0.5 m), and the corresponding phase profiles (theory and metasurfaces) for the left (b) and upper (c) metasurfaces at a specific focusing position (x_f, y_f) = (0.7 m, 0.3 m)

The idea for acoustic confinement here is to focus the arbitrarily reflected acoustic waves at will. Innovative multilateral acoustic metasurfaces composed

of aforementioned labyrinthine units for various acoustic incident exposures are proposed and analyzed for better acoustic confinement. Both numerical and theoretical methods[74] are applied to study the reflected acoustic focusing and confinement of metasurfaces. Figure 3.2(a) is a general scheme of a two-sided metasurface system consisting of two perpendicular metasurfaces with the length 1 m (10λ) for acoustic focusing. In the design, a point acoustic source (x_s, y_s) is considered and centered at (0.5 m, 0.5 m), and (x_f, y_f) is an arbitrarily desired focusing position in the acoustic field. Each of the acoustic metasurface illustrated in Fig 3.2(a) can be theoretically characterized by the normalized acoustic admittance $\tilde{\beta} = \rho_0 c_0 / Z_s = i\tan(\varphi/2)$, where $\rho_0 c_0$, Z_s and φ are the acoustic impedance, theoretical impedance and phase distribution of the metasurface structure, respectively. With suppressing the time harmonic factor $e^{-i\omega t}$ and considering the frequency domain, Green's function of free space under the 2D situation of a point source located at (x_s, y_s) can be written as[37]

$$G(x, y; x_s, y_s) = \frac{i}{4} H_0^{(1)}(k_0 R), \tag{3.1}$$

where $R = \sqrt{(x - x_s)^2 + (y - y_s)^2}$ is the distance between the field point (x, y) and the point source (x_s, y_s), and $H_0^{(1)}$ is Hankel function of the first kind at zero order. Considering a metasurface with length L, the whole field takes the form as

$$p(x, y) = \int_V G(x, y; x_s, y_s) \mathcal{D}(x_s, y_s) dV_s + \int_{L+C} \left[G(x, y; x_s, y_s) \frac{\partial p(x_s, y_s)}{\partial n_s} - p(x_s, y_s) \frac{\partial G(x, y; x_s, y_s) \mathcal{D}(x_s, y_s)}{\partial n_s} \right] dS_s \tag{3.2}$$

where $\mathcal{D}(x_s, y_s)$ is the distribution of acoustic source and can be formulated by a Dirac function with normalized quality factor as $\mathcal{D}(x_s, y_s) = \delta(x - x_s)\delta(y - y_s)$. The normal derivative of the integral paths of metasurface with length L and reflected arc with length C is $\partial / \partial n_s$. Combining Eqs. 3.1 and 3.2, the pressure of

the reflected waves modulated by the metasurface can be deduced as

$$p_{\mathrm{r}}(x,y) = -\frac{k_0}{4}\int_0^L \tilde{\beta}(y_{\mathrm{s}})p(0,y_{\mathrm{s}})H_0^{(1)}(k_0R)\Big|_{x_{\mathrm{s}}} dy_{\mathrm{s}} + \frac{i}{4}\int_0^L p(0,y_{\mathrm{s}})\frac{\partial H_0^{(1)}(k_0R)}{\partial x_{\mathrm{s}}}\Big|_{x_{\mathrm{s}}=0} dy_{\mathrm{s}} \tag{3.3}$$

where the pressure distribution $p(0,y)$ along the metasurface can be written as

$$p(0,y) = \frac{i}{2}H_0^{(1)}(k_0R)\Big|_{x=0} - \frac{k_0}{2}\int_0^L \tilde{\beta}(y_{\mathrm{s}})p(0,y_{\mathrm{s}})H_0^{(1)}(k_0R)\Big|_{x_{\mathrm{s}}} dy_{\mathrm{s}} + \frac{i}{2}\int_0^L p(0,y_{\mathrm{s}})\frac{\partial H_0^{(1)}(k_0R)}{\partial x_{\mathrm{s}}}\Big|_{x_{\mathrm{s}}=0} dy_{\mathrm{s}}, \tag{3.4}$$

which is a second-kind Fredholm integral equation. According to Eqs. 3.3 and 3.4, the reflected waves can be effectively and precisely manipulated at will by specifically designing the admittance $\tilde{\beta}$ or the phase distribution $\varphi(y)$ of the metasurface, due to the exact derivation process. Snell's law needs to be revisited to theoretically determine the phase distributions for reflected wave focusing. As for the metasurface system shown in Fig. 3.2(a), the phase profiles of the left and upper boundaries (resembled by metasurfaces) required to achieve the phase contour (blue arc line) for the focusing at (x_{f}, y_{f}) from the point source (x_{s}, y_{s}) can be expressed as,

$$\varphi_1(y) = k\left[\sqrt{(y-y_{\mathrm{s}})^2+x_{\mathrm{s}}^2} - x_{\mathrm{s}} + \sqrt{(y-y_{\mathrm{f}})^2+x_{\mathrm{f}}^2} - x_{\mathrm{f}}\right] \tag{3.5}$$

and

$$\varphi_2(x) = k\Bigg[\sqrt{(x-x_{\mathrm{s}})^2+(y_0-y_s)^2} - (y_0-y_{\mathrm{s}}) + \sqrt{(x_{\mathrm{f}}-x)^2+(y_0-y_{\mathrm{f}})^2} - (y_0-y_{\mathrm{f}}) + \Delta\varphi\Bigg], \tag{3.6}$$

where x_0 and y_0 are the length and width of the system, and k and $\Delta\varphi$ are the wave number and additional phase shift, respectively. Distinct from the single

metasurface situation, the coupling of these two metasurfaces should be dealt with to ensure the synchronization of the phase profiles at the focusing point. Considering the phase continuity of the two individual metasurfaces at the joint shown in Fig 3.2(a), $\Delta\varphi$ can be expressed as,

$$\Delta\varphi = k(2y - x_f - y_f - x_s - y_s). \tag{3.7}$$

Since (x_0, y_0) is set to be (1 m, 1 m) or $(10\lambda, 10\lambda)$, 80 elementary labyrinthine units of the eight types shown in Fig. 3.1(c) are connected in series as required to discretely fit the theoretical phase profile of each side. At a specific focusing position (0.7 m, 0.3 m), the phase profiles of the left and upper sides, provided by theory (red dot) and metasurface structures (blue square), are plotted in Figs. 3.2(b) and 3.2(c), respectively. It can be readily observed that the theoretical phase profiles shown in Figs. 3.2(b) and 3.2(c) required for focusing can be well realized by two metasurfaces composed of labyrinthine units.

3.3 Acoustic confinement results

Commercial finite element software COMSOL Multiphysics™ Version 5.2a is utilized to analyze and simulate the multilateral metasurfaces proposed in this chapter. Pressure acoustics module is applied, and the sides without metasurfaces are set as perfectly matched layer (PML). Hard boundary condition is applied for all the air-solid interfaces. In order to acquire the acoustic focusing and confinement properties and performances of the proposed multilateral metasurfaces, various structural configurations and the corresponding and relating parameters, such as acoustic pressure, intensity fields, and the acoustic focusing distributions, are sufficiently investigated and analyzed.

3.3.1 Two-sided metasurface

Two metasurfaces can be perpendicularly constructed or configured in parallel to form a two-sided metasurface. According to the aforementioned phase profiles illustrated in Figs. 3.2(b) and 3.2(c), 80 labyrinthine units are arrayed in the

left and upper sides separately and perpendicularly to form the two-sided metasurface, which can numerically achieve the focusing at the position (0.7 m, 0.3 m). The theoretically and numerically obtained sound pressure fields are normalized to the point source, and the corresponding reflected intensity fields acquired by removing the incident fields are then normalized to the maximum focusing intensities in the areas for better performance evaluation and comparison.

The normalized sound pressure and reflected intensity fields by numerical simulations are shown in Figs. 3.3(a) and 3.3(c), respectively. In order to observe the phase front and source details of the two-sided metasurface, the pressure field with point source incidence is illustrated in Fig. 3.3(a), and it can be seen that the point sound source is centered at (0.5 m, 0.5 m) and the reflected waves from the left and upper metasurfaces show continuous wave fronts as expected. Moreover, since the lower and right sides are set as PML in Fig. 3.3(a), the sound pressure is relatively low in the lower right corner except the focusing position (0.7 m, 0.3 m). Sound pressure distributions of several sampled units are magnified and provided in the dashed red rectangles shown in Fig. 3.3(a), and it is can be seen that the sound pressures inside the chamber units are high and unevenly distributed.

To study the acoustic focusing for acoustic energy confinement, the reflected sound intensity $|p|^2$ (normalized to maximum value) field relevant to energy by the two-sided metasurface (numerical) is simulated and presented in Fig. 3.3(c), without the source and the incident field for better performance evaluation. As shown in Fig. 3.3(c), the metasurface structure can well focus and confine the sound around the position (0.7 m, 0.3 m) as designed, which are quantitatively examined through analyzing the intensity along the dashed pink lines of $x = 0.7$ m and $y = 0.3$ m. The normalized sound intensity distribution curves at $x = 0.7$ m and $y = 0.3$ m achieved by the metasurface (numerical) are plotted in open blue and red cycles shown in Fig. 3.3(e), and it shows that the reflected intensity peaks at the position (0.7 m, 0.3 m) are much higher with referring to that of the incidence field (black dashed line). The sizes of the focusing spot along $x = 0.7$ m and $y = 0.3$ m are acquired by cutting the 3 dB attenuation line of the pressure amplitude $|p|$, that is, 0.25 of $|p|^2$, as shown in Fig. 3.3(e).

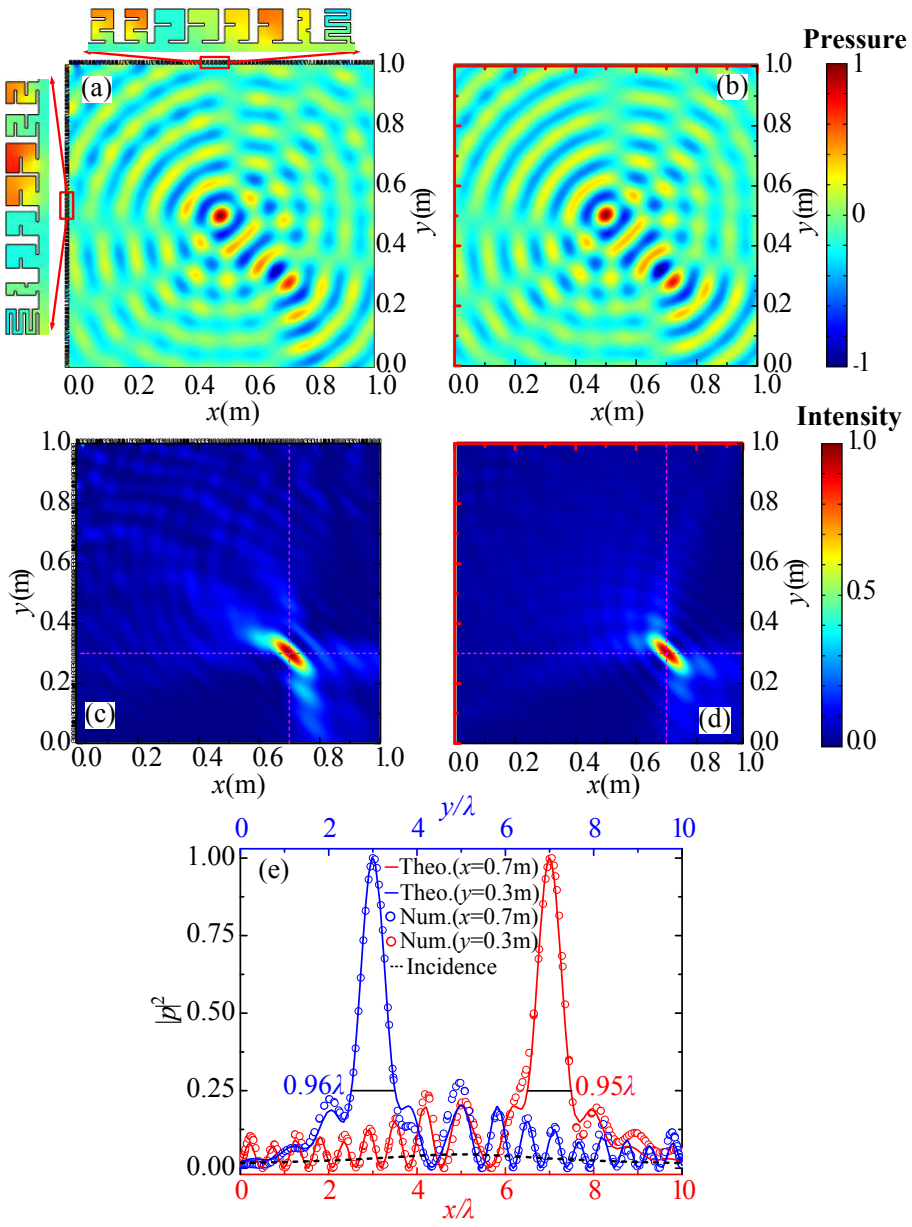

Figure 3.3 – Numerical and theoretical results of a two-sided metasurface for acoustic energy confinement. (a) Normalized sound pressure filed (numerical simulation) of the two perpendicularly connected metasurfaces composed of labyrinthine units for the focusing position (0.7 m, 0.3 m). The magnified labyrinthine units in the dashed red rectangles provide sound distribution details inside the metasurface structure. (b) Normalized theoretical sound pressure field. (c) and (d) are the normalized numerical and theoretical reflected sound intensity fields $|p|^2$, respectively. (e) Comparison of the numerical and theoretical sound intensities of the cross-section lines illustrated in (c) and (d). The blue and red circles and curves correspondingly stand for the normalized numerical and theoretical sound intensity along the horizontal (x = 0.7 m) and vertical (y = 0.3 m) cross sections. The dashed black line is the normalized incidence intensity of the point source. The two red frame lines in (b) and (d) are theoretical designs for the phase shifting manipulations.

The focusing sizes along $x = 0.7$ m and $y = 0.3$ m are 0.96 λ and 0.95 λ, respectively, which illustrate good focusing capability. To further validate the numerical simulation of the two-sided metasurface, analyzed impedance conditions are applied to the left and upper sides to theoretically calculate the pressure and intensity fields. With substituting the phase profile Eqs. 3.5-3.7 into the admittance-phase equation, the impedances for the left and upper sides can be expressed as

$$Z_s(y) = -i\rho_0 c_0 \cot[\varphi_1(y)/2] \tag{3.8}$$

and

$$Z_s(x) = -i\rho_0 c_0 \cot[\varphi_2(x)/2], \tag{3.9}$$

respectively.

Theoretical designs with impedance boundaries on the sides/frames are highlighted in red for the whole chapter. With the theoretical designs on the boundaries, the sound pressure and the reflected intensity fields are acquired and shown in Figs. 3.3(b) and 3.3(d), respectively. Compared with the pressure field acquired with the metasurface structure, the theoretical one in Fig. 3.3(b) shows a very similar pattern with a focusing at the position (0.7 m, 0.3 m), while a better consistency for each wavefront. Meanwhile, the theoretical reflected intensity field illustrated in Fig. 3.3(d) exhibits very similar distributions to that shown in Fig. 3.3(c). As before, two cross section lines through the focusing point are plotted to obtain the intensity distribution details. The specific comparison of the numerical and theoretical intensity distributions at $x = 0.7$ m and $y = 0.3$ m are illustrated in Fig. 3.3(e), where the open circles, solid lines, and dashed line stand for the numerical, theoretical and incidence intensities, respectively. It is can be readily seen in Fig. 3.3(e) that both the numerical and the theoretical results demonstrate a very good agreement with each other and prove obvious focusing at the position (0.7 m, 0.3 m), where the reflected intensities are much larger than those in the other area and those of the incidence (dashed line).

Through comparing the numerical and theoretical results, the proposed

multilateral metasurfaces composed of labyrinthine units can well realize the phase profiles in 2π range with a considerably fine discrete resolution and maintain little energy dissipation inside the structure.

As can be seen from Eqs. 3.5-3.7, the focusing point (x_f, y_f) and the source position (x_s, y_s) can be arbitrarily designed in the acoustic field, which are exemplified and validated in Appendix A.3. Unlike one-sided flat metasurfaces emphasizing on acoustic reflected/transmitted wave manipulations, multilateral metasurfaces proposed here are targeted to maximize acoustic energy confinement. Due to the phase asymmetry of the multilateral metasurface, the confined sound intensity may vary with the focusing positions. Therefore, it is quite necessary to obtain the spatial distribution of the confined sound intensity to find the maximum focusing positions, which can provide direct guidance for focusing spot selection in real applications.

To this end, the focusing position (x_f, y_f) is sufficiently swept within the region $(x, y) \in [0.1\text{ m}, 0.9\text{ m}]$, and the corresponding reflected intensities are recorded and mapped in Fig. 3.4, where as before, the point source is centered at (0.5 m, 0.5 m) and the left and upper sides (highlighted in red) are theoretically processed. The phase profile and the metasurface are theoretically redesigned according to Eqs. 3.5-3.7 for each focusing position to obtain its sound intensity. The incident sound intensities from the source are removed from the acquired intensities to get the reflected intensity field. The reflected intensities of all the focusing positions are normalized to their maximum value for a better demonstration of the optimal focusing positions/regions.

As shown in Fig. 3.4, the upper-left region (above the dashed line) demonstrates relatively high and nonuniform reflected intensity distribution, while the lower-right region approaches the opposite case. Moreover, the intensity distribution in Fig. 3.4 shows a fringe pattern in general, especially obvious in the upper-left region. The phenomena indicate that the metasurfaces on the left and upper sides work more independently on the lower-right focusing region, while demonstrate strong coupled effect for the focusing in the upper-left region besides the individual contribution from each. According to the theoretical analysis (Eqs. 3.5-3.7) of the multilateral metasurface system, the phase profile for the focusing of the premier reflection is designed, without considering the

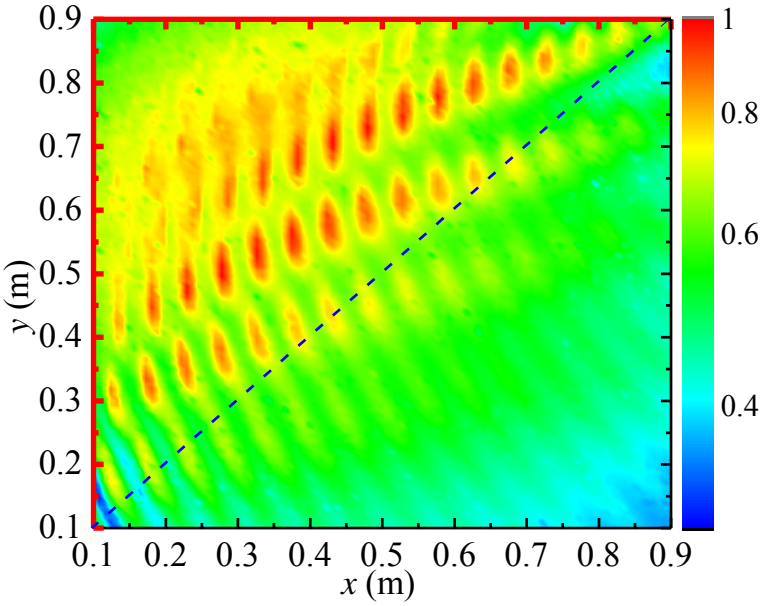

Figure 3.4 – Normalized reflected sound intensity mapping for the two-sided perpendicular configuration (left and top) within the area $(x, y) \in [0.1\ \text{m}, 0.9\ \text{m}]$.

multiple orders of reflections. The sound waves in the upper-left region can experience multiple reflecting interferences due to the hard metasurfaces in the upper and left sides. Those interferences can additionally contribute to the sound focusing besides the designed premier reflection, which accounts for a higher intensity distribution in the upper-left region and the general fringe pattern in Fig. 3.4. Meanwhile, the lower and right sides are set as PMLs and the focusing positions in the lower-right region are relatively far from the metasurface wall. Therefore, the designed focusing in the lower-right region can neither be influenced by the perfectly matched lower-right sides nor by the multiple reflecting interferences from the upper-left metasurfaces. This explains the more uniform and lower sound intensity distribution in the lower-right region shown in Fig. 3.4. As shown in Fig. 3.2(a), apparently, the two-sided perpendicular metasurface is symmetrically constructed, and thus the intensity mapping in Fig. 3.4 composed of each focusing point should be expected to be symmetrical. However, a compensated phase shift (Eq. 3.7) is introduced and breaks the symmetry of the phase profile of the whole structure to ensure a continuous and synchronized wavefront induced by each individual metasurface in each

focusing position. Therefore, the reflected intensity distribution shown in Fig. 3.4 is neither uniformly nor symmetrically distributed as anticipated.

In order to further validate and explicate the specific contributions/behaviors of the multiple reflections from the upper-left metasurfaces to the designed premier focusing, the proposed two-sided multilateral metasurface system is analyzed in the time domain (see Sec. 3.5 for details). To be more specific, representative focusing positions A (0.36 m, 0.73 m) and B (0.7 m, 0.3 m) from the upper-left and the lower-right regions are selected and studied, respectively. The source is positioned at (0.5 m, 0.5 m) and its generation function is set as sine wave with a frequency $f_0 = 1/T_0 = 3430$ Hz, where T_0 is the cycle of the source signal. The width of the source signal (number of exciting cycle) is scanned from 1 T_0 to 15 T_0 to observe the time evolution of the focused sound pressure at the targeted positions. The results at the selected positions show that, the multiple reflections hardly contribute to the pressure focusing at the position B as the sound field reaches steady state, which complies with the above discussion. As to the position A, the interferences between the left and upper metasurfaces begin to obviously reinforce the focusing when the signal width reaches 3 T_0, that is, 3 λ in space field, and the interferences increase the focusing pressure amplitude by about 20% under this specific case, which agrees well with the analysis in frequency domain shown in Fig. 3.4.

As demonstrated in Fig. 3.4, both the fully controlled premier reflection and multiple reflections that follow contribute to the acoustic energy confinement. To further explore the interference effect on the acoustic focusing and confinement, another two-sided multilateral metasurface configured with two parallel metasurfaces (lower and upper sides) is investigated. The focusing position is arbitrarily selected as (0.37 m, 0.18 m), and the detailed formula derivation of the design of the phase profiles and the compensated phase shift for focusing is similar as before, thus being neglected here to avoid redundancy.

The normalized reflected sound intensity field for the parallel multilateral metasurfaces is shown in Fig. 3.5(a), where the focusing is located around (0.37 m, 0.18 m) as designed. The reflected intensity field in Fig. 3.5(a) illustrates the focusing at the designed position and obvious standing-wave-like interfering pattern along the direction of the line passing through the source point and the

focusing point. In order to check the performance of the focusing, the cross sections along $x = 0.37$ m and $y = 0.18$ m are plotted in dashed lines in Fig. 3.5(a) and the intensity values along the lines are normalized and illustrated in Fig. 3.5(b), where the blue dash-dotted line and the red solid line stand for reflected intensity along the vertical and horizontal section lines, respectively. Along the line $y = 0.18$ m, the intensity curve (red solid line) in Fig. 3.5(b) shows a perfect focusing peak at (0.37 m, 0.18 m), while along the line $x = 0.37$ m there are several peaks besides the one at designed position (see the blue dash-dotted curve), which conforms with what shown in Fig. 3.5(a).

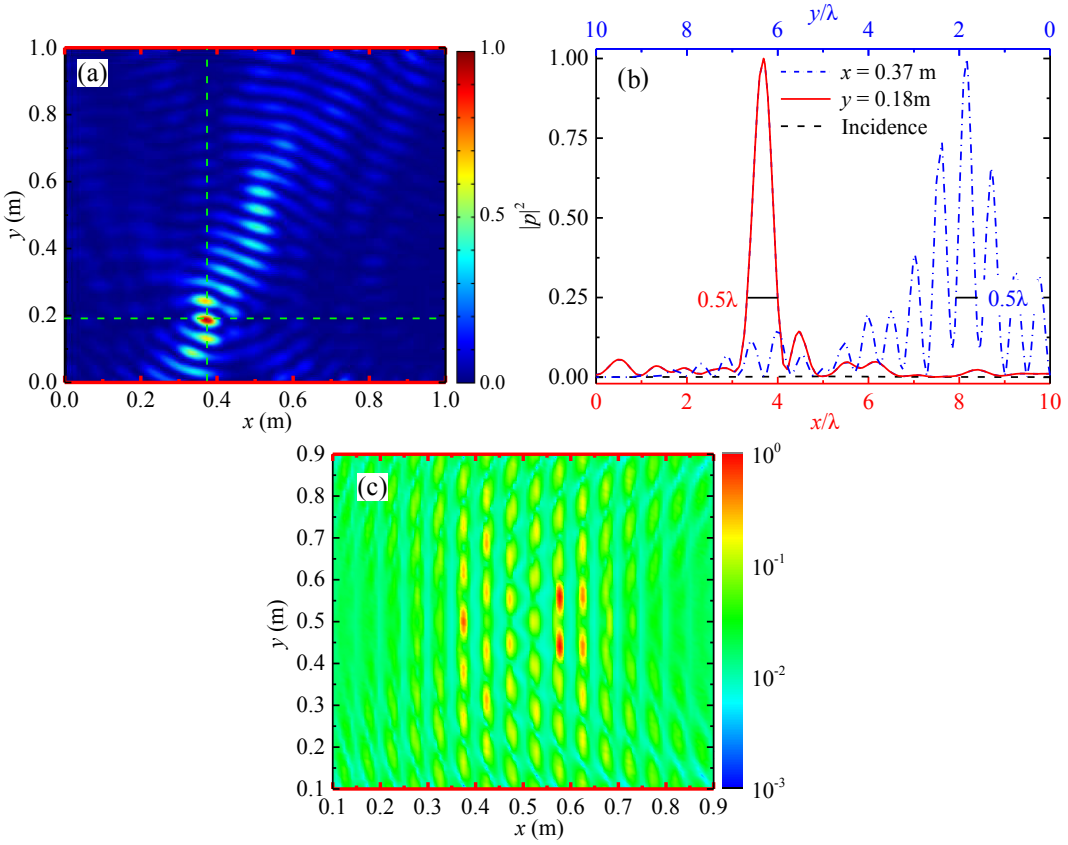

Figure 3.5 – Results of energy confinement of two-sided AMs with parallel configuration. (a) Normalized reflected sound intensity field of the two-sided parallel configuration (up and down) for a typical focusing position (0.37 m, 0.18 m). (b) Normalized sound intensity curves at the horizontal ($x = 0.37$ m) and vertical ($y = 0.18$ m) cross sections. (c) Normalized sound intensity mapping of the area $(x, y) \in [0.1\text{ m}, 0.9\text{ m}]$ for the parallel configuration.

The focusing spot sizes along $x = 0.37$ m and $y = 0.18$ m are 0.7 λ and 0.5 λ, respectively, which are smaller than those shown in Fig. 3.3(e). In Fig. 3.5(a), two parallel metasurfaces are arrayed in vertical direction with the source centering in between, and this configuration induces strong standing wave effect inside the structure, besides the designed focusing of the premier reflection. Moreover, the multiple reflections between the upper and lower sides are less likely to be absorbed by vertically arranged PMLs. These two integrated effects explain the enhanced focusing (decreased focusing spot size) at the designed position (0.37 m, 0.18 m), accompanying with a strong standing-wave-like interfering pattern.

The focusing point (x_f, y_f) is sufficiently swept within the region $(x, y) \in [0.1$ m, 0.9 m] and the acquired intensities are recorded and normalized to their maximum value to form the mapping as before. As shown in Fig. 5(c), the normalized reflected intensity is unevenly distributed in the swept region, and the ratio of maximum intensity value and that of the majorities is about one hundred, which is much larger than what shown in Fig. 3.4. In Fig. 3.5(c). The focusing areas/regions with high intensity are discretely and periodically distributed in vertical direction between the lines $x = 0.35$ m and $x = 0.65$ m), and the regions close to the left and right PMLs demonstrate relatively low intensity distribution.

The parallel design of the multilateral metasurface enhances multiple reflections, which leads to the strengthened general interfering and the standing wave effects in vertical direction. Besides the designed contribution of the first reflection, the standing wave effects periodically reinforce and weaken the focusing, which explains the discrete intensity distribution in the vertical direction and the larger intensity difference between the maximum and the majority. The source is centered in the middle of the multilateral metasurface and the PMLs in the left and right sides can absorb all the incidences and reflections, thus accounting for the higher intensity distribution in the middle. The asymmetrical intensity distribution and the fringe pattern are attributed to the asymmetrical phase profile and the general interfering effect caused by multiple reflections.

3.3.2 Three-sided metasurface

The mechanisms of multilateral metasurfaces on acoustic focusing and energy confinement are thoroughly demonstrated and elucidated under two-sided configurations. To present a complete and systematical study, three-sided metasurface is investigated as before.

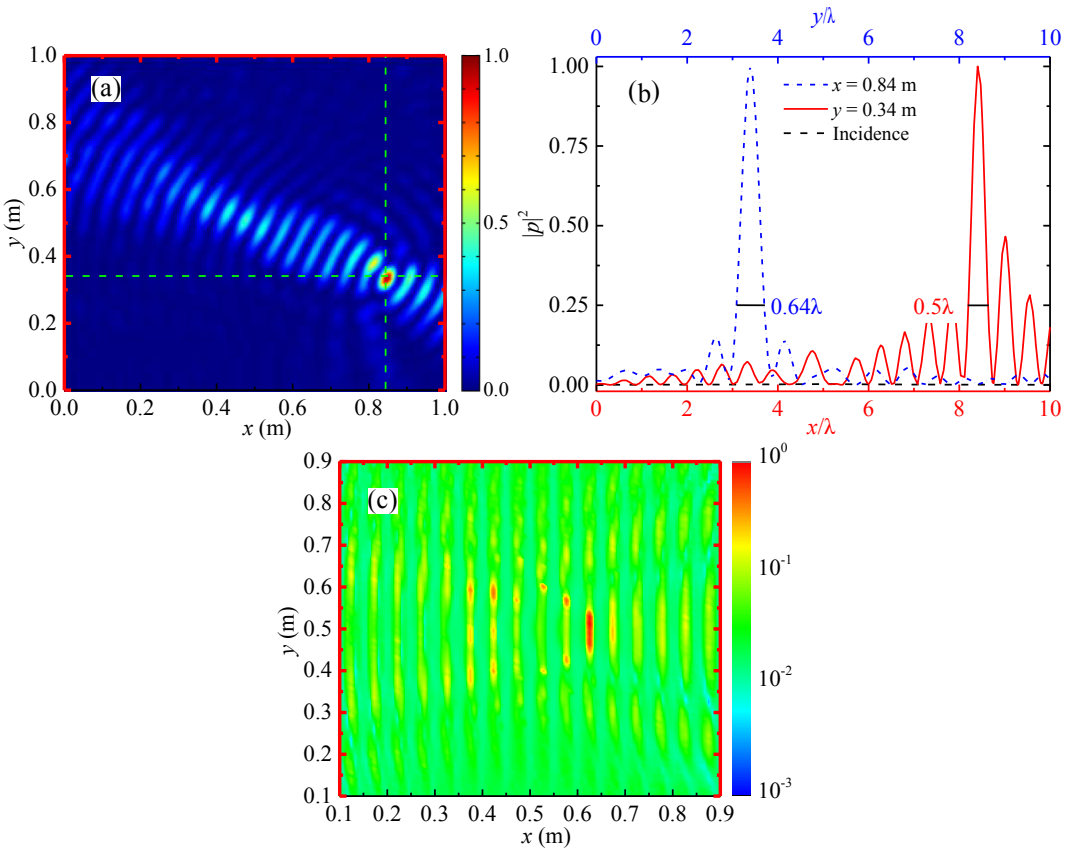

Figure 3.6 – Results of energy confinement of three-sided AMs. (a) Normalized reflected sound intensity field of the three-sided configuration (left, top and right) for a typical focusing position (0.84 m, 0.34 m). (b) Normalized sound intensity curves at the horizontal (x = 0.84 m) and vertical (y = 0.34 m) cross sections. (c) Normalized sound intensity mapping of the area $(x, y) \in$ [0.1 m, 0.9 m] for the three-sided configuration.

As shown in Fig. 3.6(a), three-sided metasurface (upper, right and left sides

highlighted in red) for a typical focusing point (0.84 m, 0.34 m) is theoretically designed with considering the phase continuity at the upper-left and upper right corners, and the lower side is set as PML. The reflected intensity field in Fig. 3.6(a) shows a good focusing at the designed point (0.84 m, 0.34 m), even though there is a standing wave interfering pattern along the line passing through the focusing point and the source. Compared with Fig. 3.5(a), Fig. 3.6(a) illustrates an improved and stronger focusing filed, in spite that both of them show obvious standing wave interfering effects.

To validate the performance of the designed focusing at (0.84 m, 0.34 m), the normalized reflected intensity curves of cross sections along $x = 0.84$ m and $y = 0.34$ m are correspondingly plotted as blue dash-dotted line and solid red line in Fig. 3.6(b), where the black dashed line represents the incidence intensity for reference. In Fig. 3.6(b), the blue dash-dotted line for the vertical section $x = 0.84$ m shows one sharp peak at (0.84 m, 0.34 m) as designed, and the intensity curve of the horizontal section $y = 0.34$ m also exhibits good focusing in spite of some minor peaks close to $x = 0.84$ m. Meanwhile, the focusing spot sizes along $x = 0.84$ m and $y = 0.34$ m for focusing performance evaluation are shown to be 0.64 λ and 0.5 λ, respectively, which demonstrate an enhanced focusing capability. Compared with Fig. 3.5(b), the peaks in Fig. 3.6(b) for the focusing performance are narrower and much clearer.

The parallel sides of the multilateral metasurface in x axis and the designed phase profile contribute to the standing wave interfering pattern in Fig. 3.6(a) generated by multiple reflections along the line passing through the source and focusing points. Moreover, the three-sided metasurface possess the combined advantages of accurate focusing and strong standing wave resonating effects of two-sided metasurfaces, which accounts for a better acoustic focusing and energy confinement performance.

As before, each focusing position is sufficiently swept within the region $(x, y) \in [0.1 \text{ m}, 0.9 \text{ m}]$ to acquire the spatial mapping of reflected intensity. Similar to what shown in Fig. 3.5(c), the normalized reflected intensity in Fig. 3.6(c) is unevenly distributed in the swept region, and the ratio of maximum intensity value and that of the majorities is more than one hundred, which indicates that the value of intensity is very sensitive to focusing position, even

though it can be arbitrarily designed. In Fig. 3.6(c), the focusing points with high intensity are discretely and horizontally distributed in the upper middle of the multilateral metasurface (between the lines $y = 0.3$ m and $y = 0.8$ m), and the whole mapping shows an unsymmetrical fringe pattern.

The parallel design of the multilateral metasurface along x axis and the metasurface on the upper side further enhance multiple reflections, which leads to the strengthened general interfering and the standing wave effects in horizontal direction. Besides the designed contribution of the first reflection, the standing wave effects periodically reinforce and weaken the focusing, which explains the fringed intensity distribution in the horizontal direction and the larger intensity difference between the maximum and the majority. The source is centered in the upper middle of the multilateral metasurface and the PML in the lower side can absorb all the incidences and reflections, thus accounting for the higher intensity distribution in the middle. The asymmetrical intensity distribution and the fringe pattern are interpreted as the asymmetrical phase profile and the general interfering effect caused by multiple reflections inside the multilateral metasurface. Additionally, the neglected airborne dissipation should lead to a slightly lower focusing amplitude in real situation due to the strong multiple reflections in the three-sided case.

3.3.3 Enclosed metasurface

Both the completely controllable premier reflection and the multiple reflections that follow enhance with the increase of the sides of multilateral metasurfaces. These two types of reflection are coupled and corporately contribute to the acoustic confinement. To achieve maximum acoustic focusing and energy confinement, enclosed metasurface with four sides are investigated in great details.

Four flat metasurfaces are theoretically designed to construct the completely enclosed multilateral metasurfaces with considering the phase continuity at each joint corner. The point sound source is centered at (0.5 m, 0.5 m) and the focusing position is selected at (0.21 m, 0.24 m). As illustrated in Fig. 3.7(a), the normalized sound pressure field containing the sound source and incidence formed by the multilateral metasurface shows a very strong focusing pattern

of wavefronts at the designed point, as well as at the source point, with close observation. The sound pressure value at the focusing point in Fig. 3.7(a) is comparable to the value of the sound source and is much higher than that under the two-sided metasurface situation shown in Fig. 3.3(b). The pressure field shows an accurate and strong acoustic confinement performance as designed at the selected focusing position.

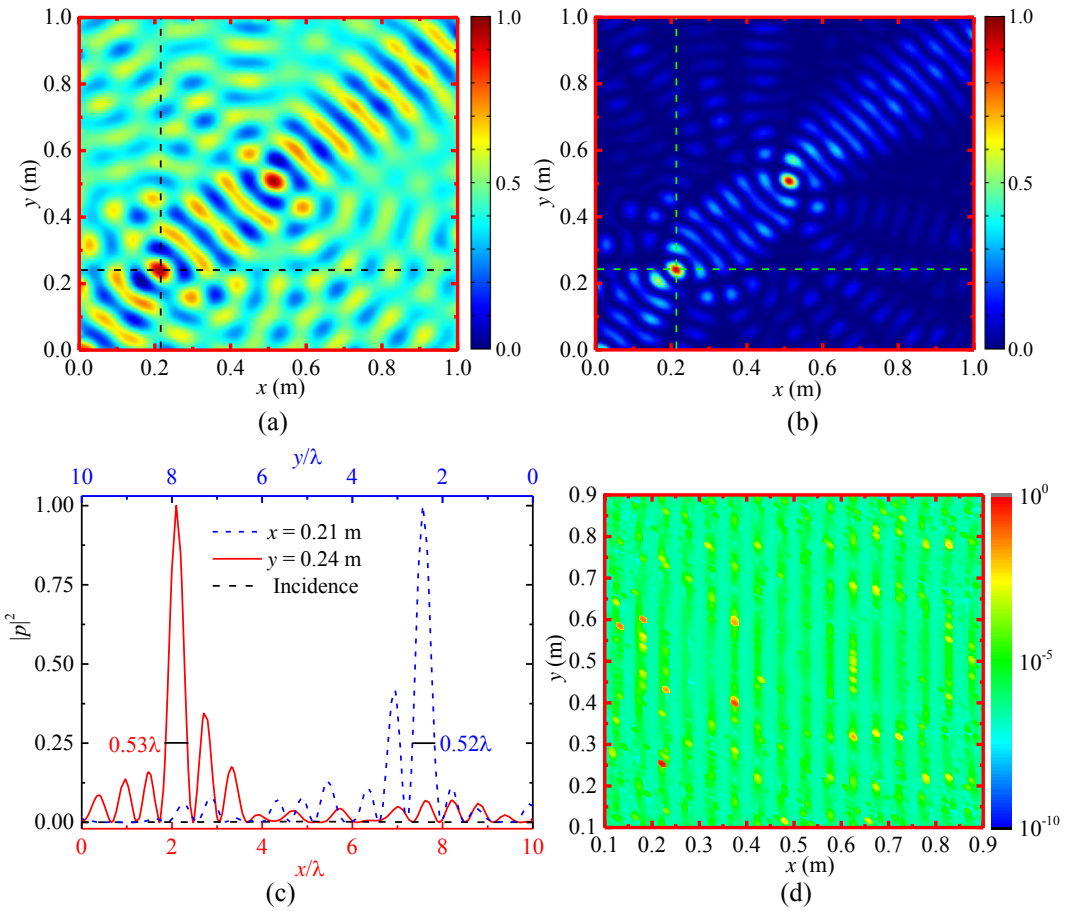

Figure 3.7 – Results of energy confinement of enclosed AMs.(a) Normalized sound pressure filed of the enclosed configuration for a typical focusing position (0.21 m, 0.24 m). (b) Normalized reflected sound intensity field of the enclosed configuration for a typical focusing position (0.21 m, 0.24 m). (c) Normalized sound intensity curves at the horizontal (x = 0.21 m) and vertical (y = 0.24 m) cross sections. (d) Normalized sound intensity mapping of the area $(x, y) \in$ [0.1 m, 0.9 m] for the enclosed configuration.

The normalized reflected sound intensity field is checked and illustrated in Fig. 3.7(b), where there is another one obvious focusing point right at the source position (0.5 m, 0.5 m), besides the strong one designed at (0.21 m, 0.24 m).

Similarly, there is a standing wave interfering pattern along the line passing through the focusing point and the source in the Fig. 3.7(b), and smaller interferences from other directions can also be observed. To evaluate the performance of the designed focusing at (0.21 m, 0.24 m) under the enclosed configuration, the normalized reflected intensity curves of cross sections along $x = 0.21$ m and $y = 0.24$ m are correspondingly plotted as blue dash-dotted line and solid red line in Fig. 3.7(c), where the black dashed line represents the incidence intensity for reference. In Fig. 3.7(c), the intensity curves of the vertical section $x = 0.21$ m and the horizontal section $y = 0.24$ m exhibit similarly good and accurate focusing performance, which varies with what shown in Figs. 3.5(b) and 3.6(b). The focusing spot sizes along $x = 0.21$ m and $y = 0.24$ m are as small as 0.53 λ and 0.52 λ, respectively. The focusing results agree well with what exhibits in Fig. 3.7(b).

As explained before, only the premier/first reflection from the metasurface is totally controlled through designing its phase profile for the focusing, while the standing-wave-like multiple reflections can enhance or weaken the focusing and confinement, which is heavily dependent on the specific positions and the geometrical configuration of the metasurface. No PML side is utilized for the completely enclosed multilateral metasurface and there is no chance for absorption from any sides, which leads to extremely strong multiple reflections inside the space that the metasurface contains. It is worth noting that the real sound amplitude can be slightly decreased under the strong reflecting situation due to the airborne dissipation, even though the labyrinthine units are optimized for minimum thermo-viscosity. The designed phase profile and some of the multiple reflections contribute to the designed acoustic focusing and confinement due to the modified generalized Snell's law and wave interfering mechanism. The other multiple reflections are responsible for the obvious focusing at the source position (0.5 m, 0.5 m) due to the strong standing wave resonating and interfering from all the four sides.

To find the positions for maximum acoustic focusing and confinement, the

spatial intensity distributing mapping of the reflected intensity of each designed position is investigated and acquired through sufficiently sweeping each focusing position(x_f, y_f) within the region $(x, y) \in [0.1\ \text{m}, 0.9\ \text{m}]$. The result is illustrated in Fig. 3.7(d), where, unlike the distributions under previous configurations, the focusing positions with maximum reflected intensities are dispersedly distributed in the whole swept region, and the ratio of maximum intensity value and that of the majorities is more than 10^5, which indicates that the acoustic energy confinement of enclosed metasurface is extremely sensitive to focusing position. In Fig. 3.7(d), the reflected intensity mapping shows an asymmetrical vertical fringe pattern in general, and all the maximum focusing spots are located at the enhanced strips (dark green bands). The cycle the fringe or the width of each two strips is about 0.1 m, which happens to be one wavelength of the incident wave.

The premier/first reflections can be completely controlled as desired through designing the phase profile of the multilateral metasurface, while the standing-wave-like multiple reflections or other types of interfering effects are heavily dependent on the specific focusing positions and the geometrical configuration of the multilateral metasurfaces. For enclosed multilateral metasurface, no PML side with total absorption is utilized, thus leading to extremely strong multiple reflections for standing wave resonating and interfering effects from all the metasurface walls. This leads to the dispersed distribution of the points with maximum intensities and explains the very large ratio of maximum intensity value and that of the majorities. The enhanced standing wave resonating and interfering effects induced by strengthened multiple reflections also increase the position dependence of the focusing. The phase shift compensations are applied in the joints of each two metasurfaces with referring to the vertical left metasurface. Even though the whole phase profile of the enclosed metasurface is designed specially for premier reflection control, it could have some other influence on standing wave resonances generated by the following multiple reflections, which may lead to the general fringe pattern in vertical direction. As elucidated previously, both the designed premier reflections and the following multiple reflections contribute to the acoustic focusing and confinement in a corporately way, which may be the reason that the maximum focusing spots

are located at the enhanced strips generated by standing waves. The width between two enhanced or weakened strips takes up one wavelength, which further validates the standing wave effects of the enclosed multilateral metasurface.

3.3.4 Summarized focusing results

The focusing and confinement results of the multilateral metasurfaces of two to four sides with various geometrical configurations are demonstrated in great details from Fig. 3.3 to Fig. 3.7. The main purpose is to propose and evaluate the innovative metasurface systems specialized for acoustic focusing and energy confinement, and thus it is quite necessary to make a quantitative comparison of all the metasurface systems to check their relative performances.

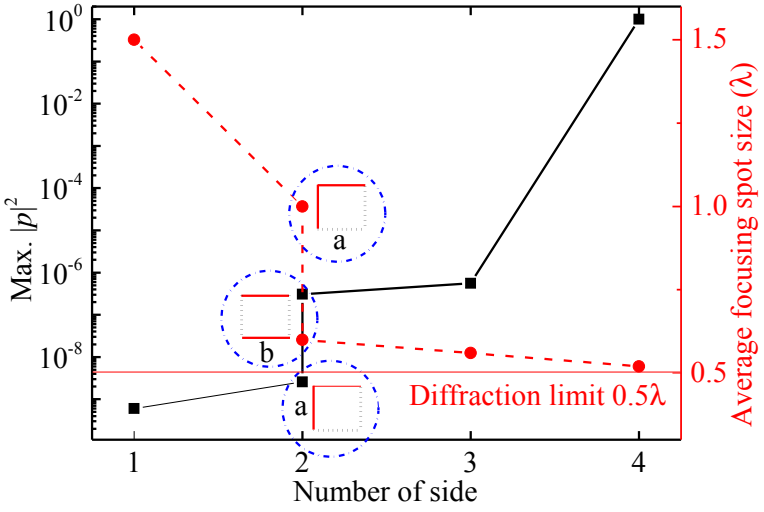

Figure 3.8 – Normalized maximum reflected intensities and average focusing spot sizes achieved under multilateral metasurfaces with various number of side.

The maximum reflected acoustic intensity and the average confined spot sizes representing the capability of the focusing and energy confinement are investigated and illustrated in Fig. 3.8 as solid black squares and red circles, respectively. To make a complete comparison, the confined maximum reflected intensity of the one-sided ordinary flat metasurface is also provided. As shown in Fig. 3.8, the dashed blue cycles a and b represent two different geometrical configurations (perpendicular and parallel) of the two-sided multilateral meta-

surface, and it can be seen that the parallel one possesses higher maximum value. Meanwhile, the maximum intensity increases with the degree of the enclosure of the metasurfaces (number of side of metasurfaces) in Fig. 3.8.

On another aspect, the focusing is enhanced with the increase of the enclosure degree, which leads to the decrease of the focusing spot sizes in Fig. 3.8. Similarly, the parallel configuration demonstrates the focusing spot sizes are above the diffraction limit (red line in Fig. 3.8), due to the absence of the evanescent wave propagation mode from the surfaces. The standing wave resonating effect caused by the multiple reflections from two parallel metasurfaces greatly contributes to the acoustic focusing and energy confinement, which explain the higher maximum intensity value under the parallel configuration. As the increase of the enclosure, the multilateral metasurfaces can catch more acoustic incidence from the source, and achieve stronger multiple reflections, which corporately contribute to the acoustic focusing and energy confinement, besides the controlled premier reflections. Therefore, the maximum intensity increases with the degree of the enclosure of the metasurfaces.

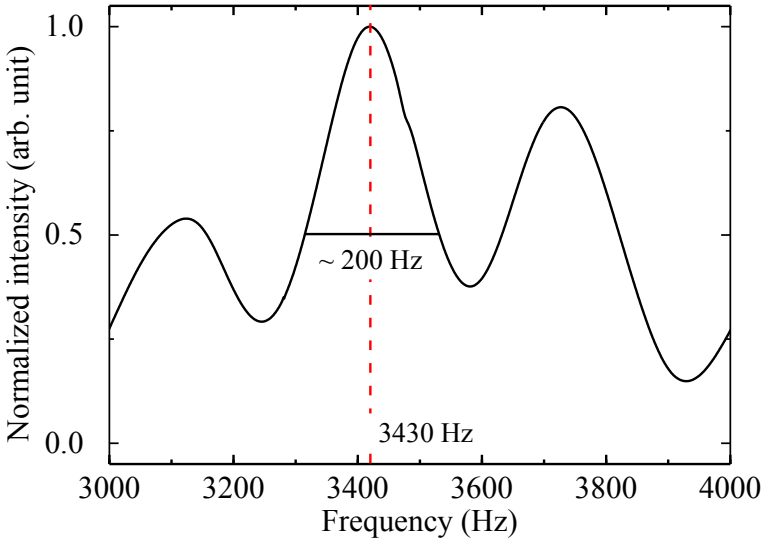

Figure 3.9 – Bandwidth of two-sided metasurface.

The bandwidth properties of the proposed multilateral metasurfaces are explored with respect to number of sides. A typical example of the frequency response of a two-sided metasurface with perpendicular configuration is provided

in Fig. 3.9, and the bandwidth is about 200 Hz around the working frequency (3430 Hz). The bandwidths of metasurfaces with other configurations have also investigated. Generally, the metasurface structures with various configurations demonstrate narrow bandwidth characterization (< 200 Hz). Specifically, the bandwidth reduces with the increase of the degree of the enclosure of the metasurfaces.

3.4 Thermovicous effects

The airborne thermo-viscous effects of the labyrinthine unit cell are systematically and numerically studied with details.

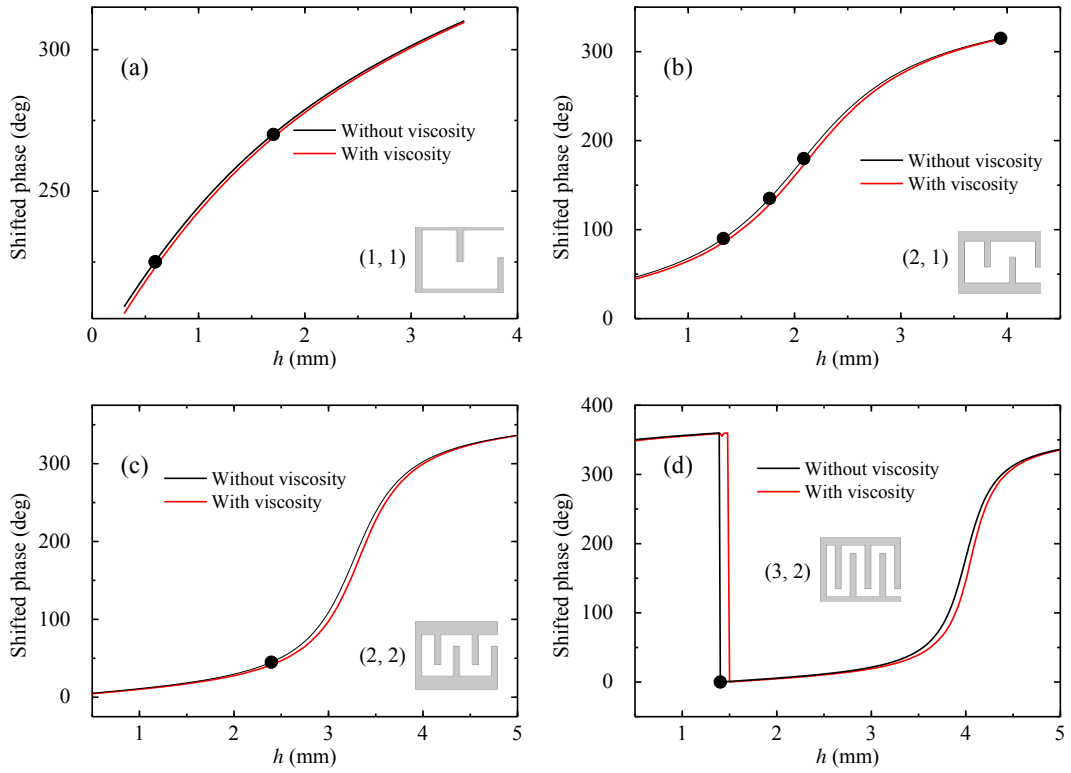

Figure 3.10 – Phase variations by thermo-viscosity. Phase shift profiles with and without considering the thermo viscosity towards plate thickness h under four $(m, n) = (1, 1), (2, 1), (2, 2)$ and $(3, 2)$ configurations, which are demonstrated in (a), (b), (c) and (d), respectively.

The commercial finite element software COMSOL Multiphysics™ Version 5.2a is utilized for the modeling and simulation as before, where the modules of Thermoviscous Acoustics module, Pressure Acoustics, and Solid Mechanics are utilized.

When designing labyrinthine units for metasurfaces, the ideal target is to obtain the desired and exact phase shift with zero acoustic loss/dissipation for each unit. However, in real situation, the thermo-viscous effects may potentially lead to the reduced reflection coefficients and the undesired phase variation for each labyrinthine unit.

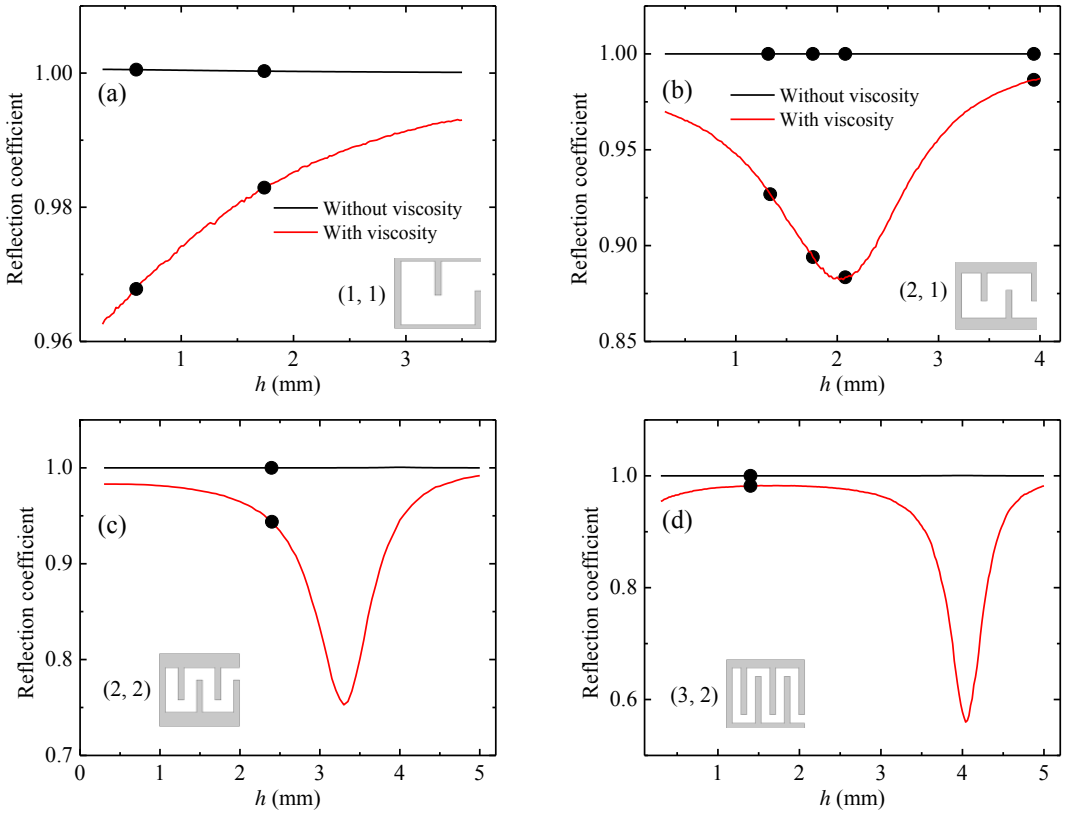

Figure 3.11 – Reflection coefficient varied by thermo-viscosity. Reflection coefficients with and without considering the thermo viscosity towards plate thickness h under four $(m, n) = (1, 1), (2, 1), (2, 2)$ and $(3, 2)$ configurations, which are demonstrated in (a), (b), (c) and (d), respectively.

The plate thickness h and the cell configuration (m, n) are the two essential parameters to control the geometries (length, width, etc.) of the air channel

of labyrinthine units for phase shift designs. The channel geometries directly determine the thermo-viscous properties of each unit, and further that of the whole metasurface. Therefore, the plate thickness h of the units with all the four (m, n) configurations and their corresponding phase variations and reflection coefficients are broadly investigated, which are shown in Figs. 3.10 and 3.11, respectively.

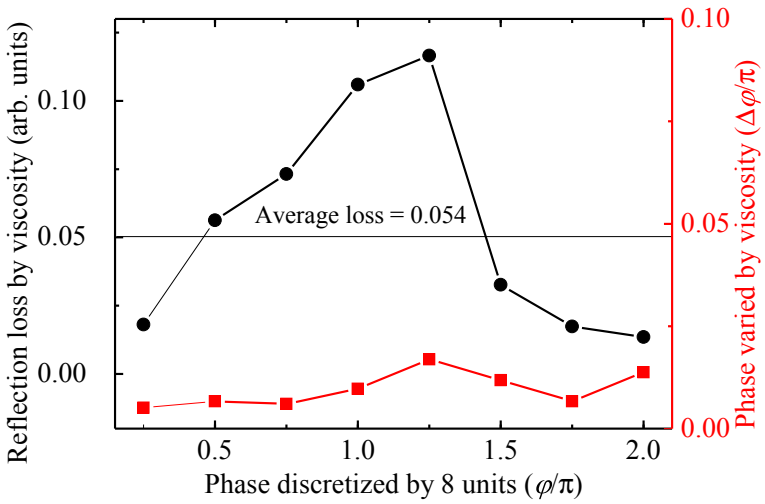

Figure 3.12 – Reflected loss coefficients and phase variations of the eight labyrinthine units caused by thermo viscous effects.

The phase shift profiles of labyrinthine units under four (m, n) configurations with (red lines) and without (black lines) considering the thermo-viscous effects are illustrated in Fig. 3.10. Plate thickness parameter h of the units with four configurations (1, 1), (2, 1), (2, 2) and (3, 2) is scanned in the range [0.5 mm, 5 mm] in Fig. 3.10(a) - 3.10(d), respectively, where the solid cycles stand for the selected/applied units under each configuration. As shown in Fig. 3.10, thermo viscosity barely influences the designed phase shift profiles with various h under any (m, n) configuration, and thus its effect on phase variation to labyrinthine units is negligible.

In parallel, the reflection coefficients of the labyrinthine units under four (m, n) configurations with (red lines) and without (black lines) considering the thermo-viscous effects are illustrated in Fig. 3.11. Plate thickness parameter h of the units with four configurations (1, 1), (2, 1), (2, 2) and (3, 2) is scanned in

the range [0.5 mm, 5 mm] in Figs. 10(a) - 10(d), respectively. The solid cycles stand for the selected/applied units under each configuration. As shown in Fig. 3.11, the reflection coefficients are around 1 for all the plate thickness parameter h under all configurations when the thermo viscosity is not considered. The reflection coefficient under configuration (1, 1) is very close to 1 and increases with h in Fig. 3.11(a). There is obvious reflection loss valley around certain h values caused by thermo viscosity for configurations (2, 1), (2, 2) and (3, 2) as shown in Fig. 3.11(b)-(d). Most of the selected units avoid the viscous loss valley and achieve optimal reflection coefficients.

The thermo-viscous effects of the eight units we utilized to fabricate the metasurfaces in this chapter are concluded in Fig. 3.12. The phase variations caused by the thermo viscosity is very small and less than 0.02 π for all the eight units, as shown in red squares in Fig. 3.12. The reflection loss varies a little bit for different unit and is small as well. The average reflection loss coefficient of the eight units is about 0.054, which is valid to be neglected in numerical calculation.

3.5 Time domain analysis of two-sided metasurface

The proposed acoustic multilateral metasurface systems are partially or completely enclosed in geometries, which inevitably generate multiple reflections between/among metasurface walls. The acoustic multilateral metasurfaces are designed specially for the focusing and energy confinement of the premier reflection of the source. Frequency domain study of the multilateral metasurfaces generally provides steady state analysis. Therefore, it is quite necessary to conduct time domain analysis when the tracking of the contributions/behaviors of multiple reflections is required.

The case of the perpendicular two-sided metasurface is studied, and representative focusing positions A (0.36m, 0.73 m) and B (0.7 m, 0.3 m) shown in Fig. 3.13(a) from the upper-left and lower-right areas are selected for the time domain analysis. The point sound source is set at S (0.5 m, 0.5 m) and its generation function is sine wave with a frequency of f_0 = 3430 Hz. Figs. 3.13(b) and 3.13(c) are examples of time domain results of the focusing pressure fields

at A and B, under identical source with a width of 6 T_0.

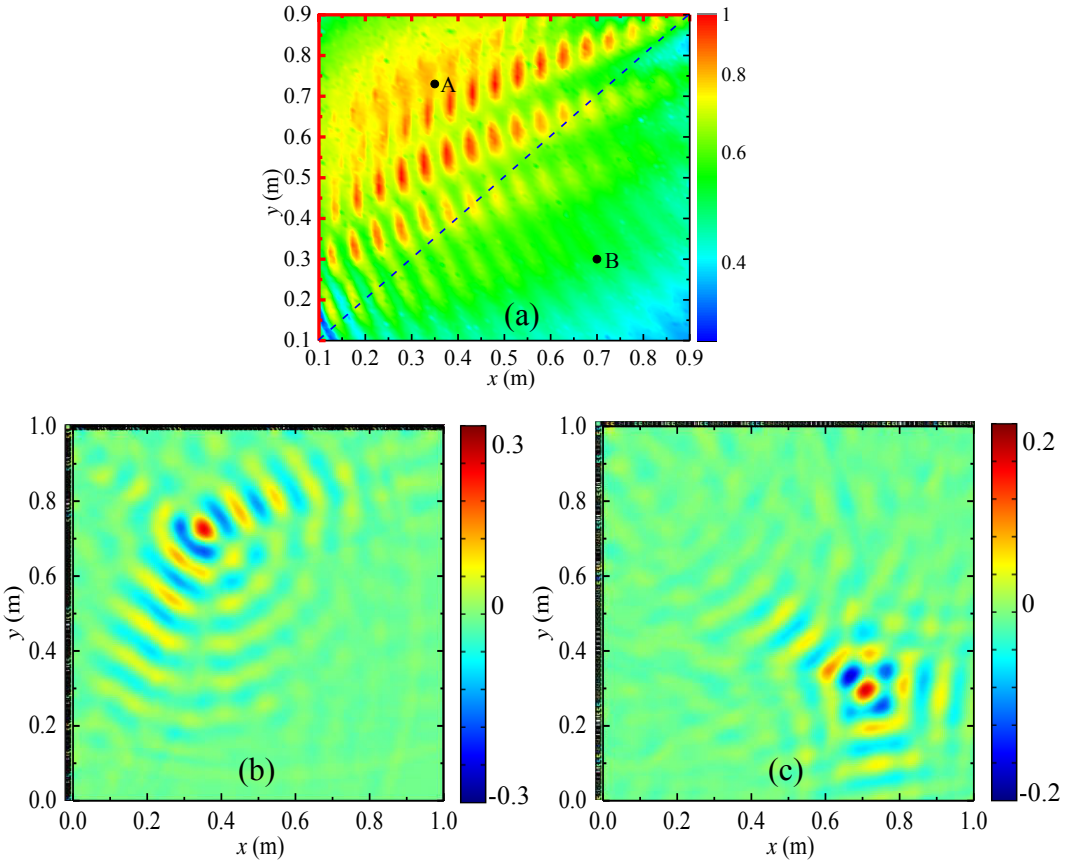

Figure 3.13 – Pressure distributions at two exemplary focusing positions. (a) Representative focusing positions A (0.36 m, 0.73 m) and B (0.7 m, 0.3 m) in the upper-left and lower-right regions. (b) Normalized acoustic pressure field of the focusing position A at time $t = 14.6\ T_0$ with a generation signal width of 6 T_0. (c) Normalized acoustic pressure field of the focusing position B at $t = 17\ T_0$ with a generation signal width of 6 T_0.

As shown in Figs. 3.13(b) and 3.13(c), the maximum focusing acoustic pressure fields of A and B are acquired at time $t = 14.6\ T_0$ and $t = 17\ T_0$, respectively, and then the fields are normalized to the point source with a amplitude of 20000 (Pa). The pressure fields shown in Figs. 3.13(b) and 13(c) demonstrate good focusing performance in time domain as well, and the complete time evolution of the focusing pressure fields at A and B are demonstrated in VIDEO 1 and

VIDEO 2[1], respectively.

For multilateral metasurfaces, the whole acoustic pressure field is composed of three kinds of interacting contributions, which are (I) the controlled premier reflected waves from each metasurface wall, (II) the incident waves when the width of the source signal is large enough to overlap with the reflections, and (III) the multiple reflections between/among metasurface walls. These three contributions are greatly dependent on the width of the point source signal. Therefore, the width of the source signal for the focusing of A and B is scanned from T_0 to 15 T_0 to check the behaviors of each contributions in time domain. The time evolution of the acoustic pressure field $p(t)$ for A and B are explored, and several crucial results are provided in Fig. 3.14.

The pressure towards time curves at position A and B with one cycle T_0 generation are shown in Figs. 3.14(a) and 3.14(g), respectively. The distances from A and B to the point source are 2.7 λ and 3.6 λ, and the first arrival incidence for A and B should be expected at 2.7 T_0 and 3.6 T_0, respectively, which are illustrated in Figs. 3.14(a) and 3.14(g). Since the distance difference for A and B to the source is small, the amplitudes of both incident waves show no big difference in Figs. 3.14(a) and 3.14(g). Compared with A, the position B is further away from the metasurfaces, and thus the time of the focusing for B is longer than that of A. Since the width of the source signal is as narrow as T_0, it is neither impossible to form an interfering pattern in space field nor for the direct incidence to overlap with the reflections. Therefore, the contribution of multiple reflections to the focusing in this situation hardly exists, neither does the contribution of direct incidence. The reflected focusing waves in A and B are purely due to the designed metasurface, which explains the almost identical focusing amplitudes shown in Figs. 3.14(a) and 3.14(g). As we increase the width of the source generation signal to 3 T_0, the multiple reflections between the metasurface walls begin to influence the designed reflected focusing waves for position A. Compared with Fig. 3.14(i), the reflected wave shows a large improvement in amplitude in Fig. 3.14(c), which is caused by the multiple

[1]Click "VIDEO 1" and "VIDEO 2" to view the videos.
https://journals.aps.org/prapplied/abstract/10.1103/PhysRevApplied.7.054006#supplemental

reflections between the left and upper metasurface walls at position A. The focusing position B is close to the perfect absorbing sides, and there is very little contribution from multiple reflections.

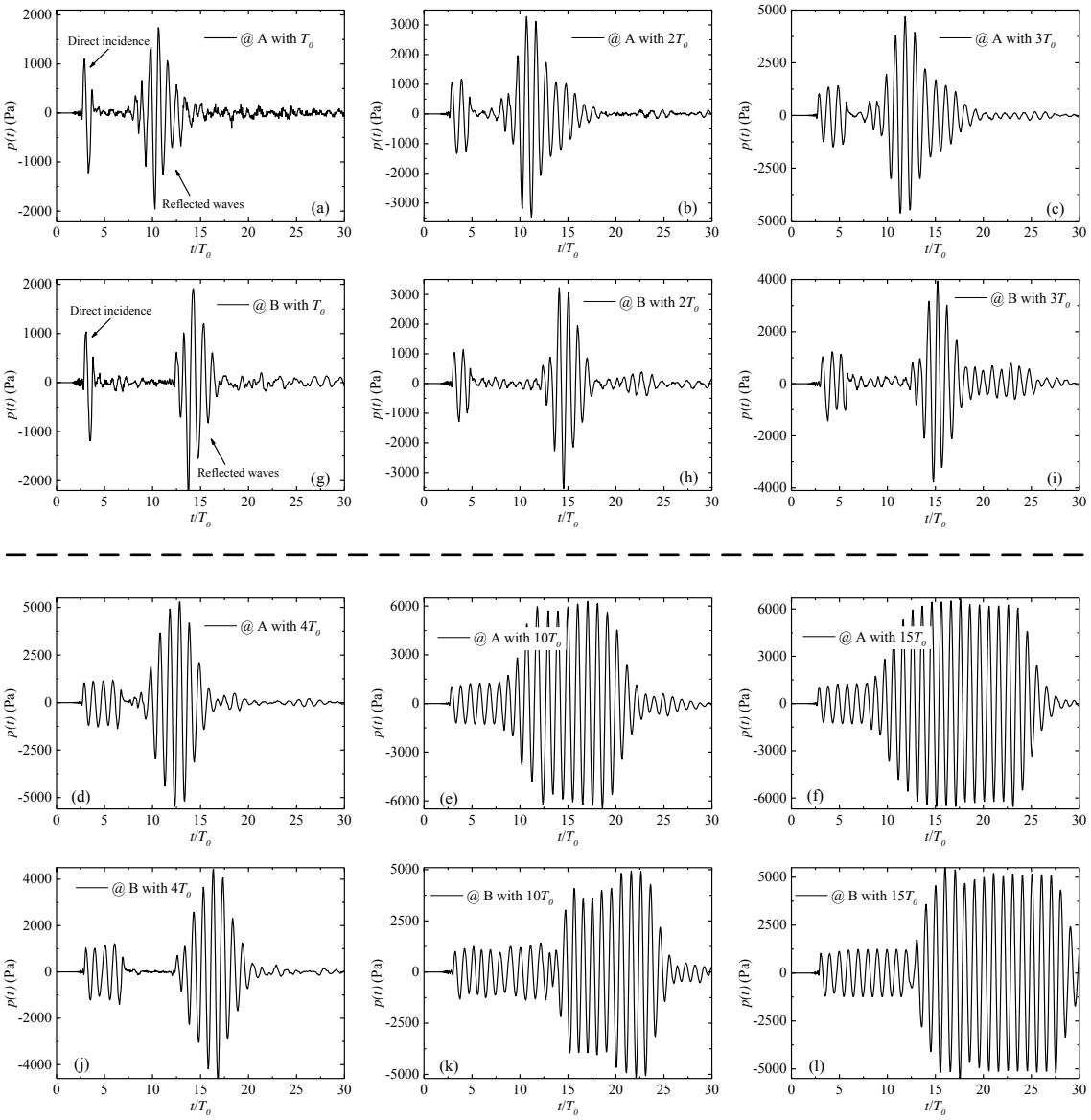

Figure 3.14 – (a) - (f) are the focusing pressure curves towards time at position A with generation signals of 1 T_0 - 3 T_0 and 4 T_0, 10 T_0, 15 T_0, respectively. (g) - (l) are the focusing pressure curves towards time at position B with generation signals of 1 T_0 - 3 T_0 and 4 T_0, 10 T_0, 15 T_0, respectively.

The amplitudes of the reflected wave slightly increase until flat as we further increase the signal width to the values (5 T_0 for A and 9 T_0 for B) before the overlap of the incidence and the reflection for each position happens. It is worth noting that the focusing amplitudes of A and B increase with the width of the source generation signal, due to the better the superposition of controlled reflected waves from each metasurface wall. This explains the increase of the reflections as the width increases from T_0 to 4 T_0 for both A and B, besides the additional contribution of multiple reflections at B, as illustrated in Figs. 3.14(a) - 14(d) for A and Figs. 3.14(g) - 14(j) for B.

When the signal width reaches 10 T_0, the incidences overlap with the reflections for both A and B, and thus an additional superposition of the incidence and reflection is expected. This explains the further increase in amplitudes and width of the reflected waves for A and B in Figs. 13(e) - 13(f) and Figs. 13(k) - 13(l).

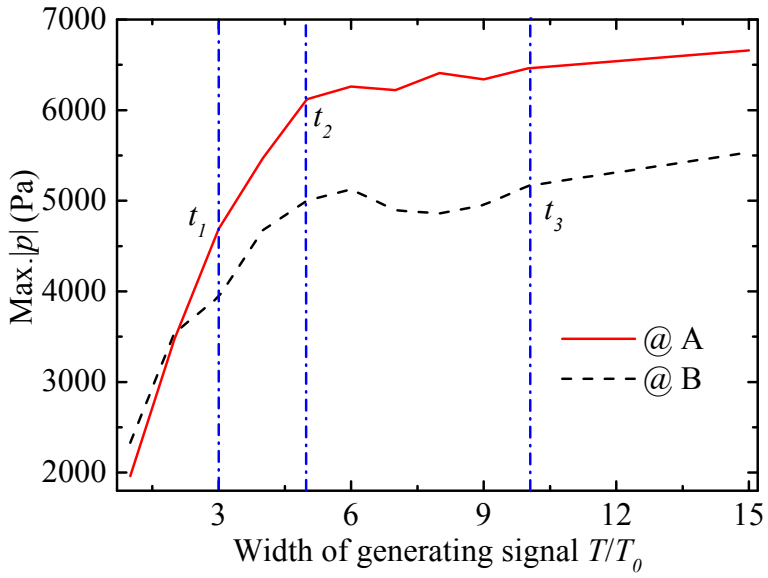

Figure 3.15 – Maximum sound pressure as a function of generating signal duration at positions A and B.

The contribution of the multiple reflections changes with the increase of the source width. When the source width is below 2 T_0, the multiple reflections demonstrate little or no obvious contribution to the reflected waves for both A

and B. As the source width reaches 3 T_0, the multiple reflections show strong and obvious influence on the amplitude and width of the reflected waves for A only. The maximum amplitudes of the reflected focusing waves under 3 T_0 for A and B are 4690 (Pa) and 3939 (Pa), respectively. As the pressure fields for A and B reach steady state (about 15 T_0), the reflected focusing waves for A and B are 6770 (Pa) and 5534 (Pa), respectively. Based on the data, the contribution of the multiple reflections to the whole focusing at position A is roughly estimated to be 20%. The perpendicularly configured two-sided metasurface for position A achieves around 33.8% of the focusing from the point source in pressure amplitude.

The confined maximum sound pressure values at A and B achieved by the two-sided metasurface as a function of exciting signal duration are concluded in Fig. 3.15. With the signal duration less than 3 T_0, the sound pressures at A and B are nearly equal to each other, due to the lack of superposition of multiple-times reflection. The coupling effect of the left and right metasurfaces is reinforced with the increase of the exciting signal duration, which accounts for the increase of confined sound pressure with generating signal width at both A and B in Fig. 3.15. The superposition of the multiple reflections from the upper and left sides at position A begins to take effect from 10 T_0, and the confinements for position A and B reach steady after 15 T_0 and 10 T_0, respectively, due to the lack of the multiple reflection effect for position B. The confined acoustic wave pressures with the exciting signal widths t_1, t_2 and t_3 in Fig. 3.15 well explain the aforementioned three possible contributions for the reflected wave focusing at A and B.

3.6 Metasurface AEH system and outputs

Based on the fundamental idea of coiling up space and generalized Snell's law, the innovative concept of acoustic focusing and energy confinement with multilateral metasurfaces composed of labyrinthine elements has been proposed in previous sections. Multilateral metasurfaces with various sides from two to four and different geometrical configurations are theoretically and numerically investigated and validated in great details in terms of acoustic focusing and energy confinement. The results show that all the proposed multilateral

metasurfaces illustrate excellent performances in acoustic focusing and energy confinement, and that the maximum confined intensities of each system increase with the degree of the enclosure of the multilateral metasurfaces. Both the completely controllable premier reflection and the multiple reflections that follow are coupled and corporately contribute to the acoustic focusing and energy confinement.

Furthermore, the standing wave resonance and other types of interfering effects caused by multiple reflections lead to the uneven spatial intensity distributions of the metasurface systems. The mappings of the acoustic intensity distribution for all the proposed multilateral metasurfaces can provide a worthwhile and practical guide for the further AEH applications. Moreover, the specific investigation and minimization of the thermal viscosity effects of the proposed metasurfaces, as well as the time domain analysis, validate the strong focusing performance for feasible and practical AEH in real situations. The innovative multilateral metasurfaces with variable configurations demonstrate strong acoustic focusing capabilities and flexibilities in terms of acoustic energy confinement, which should be ideal candidates for AEH under various situations when the acoustic energy conversion aspect is handled.

With the sufficient investigation and analysis of the previously proposed multilateral metasurfaces, an innovative acoustic energy harvester based on such metasurfaces and a piezoelectric bimorph will be proposed and discussed in this section. As discussed in previous sections, the coiling-up-space concept realized by labyrinthine units is applied to achieve the desired phase profiles for the acoustic focusing and energy confinement. The acoustic energy confined by the metasurfaces from a point source is converted into electrical energy by a structured piezoelectric bimorph. Numerical simulations and theoretical analysis of the AEH system will be provided and the output voltage and power of harvesting system will be presented thereafter.

3.6.1 Acoustic energy harvesting system

The schematic diagram of an AEH system based on a two-sided multilateral metasurface and a piezoelectric bimorph energy converter is illustrated in Fig.

3.16(a). The point sound source (x_s, y_s) is placed in the center and the arbitrarily designed focusing point (x_f, y_f) is in the lower-right corner.

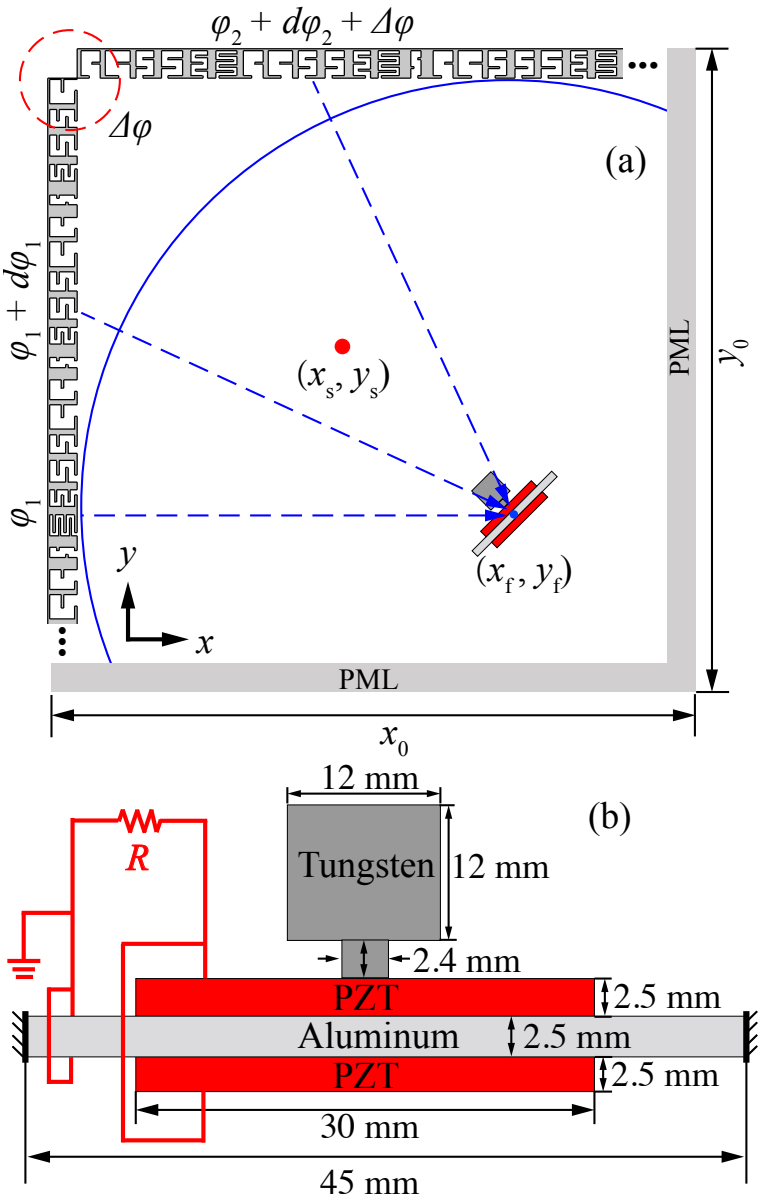

Figure 3.16 – An AEH system composed of metasurfaces and a piezoelectric cantilever. (a) Schematic diagram of a partially enclosed AEH system composed of two perpendicular metasurfaces and a piezoelectric bimorph cantilever. (b) Sketch of the piezoelectric bimorph acoustic energy converter with a tungsten mass and a resistive load circuit.

As theoretically analyzed in previous section, the two-sided acoustic metasurface illustrated in the upper-left sides of the AEH system shown in Fig. 3.16(a) can be theoretically characterized by the normalized acoustic admittance $\tilde{\beta} = \rho_0 c_0 / Z_s = i\tan(\varphi/2)$, where $\rho_0 c_0$, Z_s and φ are the acoustic impedance, theoretical impedance and phase distribution of the metasurface structure, respectively.

The lower and right sides of the AEH system shown in Fig. 3.16(a) are set as perfectly matched layers (PMLs), and the theoretical phase profiles of the left and upper sides (resembled by the multilateral metasurface) required to achieve the phase contour line (blue arc) for the focusing at (x_f, y_f) can be adopted as $\varphi_1(y)$ and $\varphi_2(x)$ from Eqs. 3.5 and 3.6, respectively. Considering the phase continuity of the two individual metasurfaces at the joint shown in Fig 3.16(a), the compensated phase shift $\Delta\varphi$ can be taken from Eq. 3.7.

The size of the system (x_0, y_0) is set to be (1 m, 1 m) or $(10\lambda, 10\lambda)$, and thus 80 elementary labyrinthine units from the eight types shown in Fig. 3.1 are arrayed in the left and upper sides to construct the multilateral metasurface to discretely fit the theoretical phase profile required for the designed focusing at (x_f, y_f).

It is worth noting that the size of the system can be varied as required for various applications, and the system can be still effective until its size going down to $(3\lambda, 3\lambda)$ or 3λ for one-sided case. With the theoretical phase profiles designed by Eqs. 3.5-3.7 and the discretely represented multilateral metasurfaces constructed by labyrinthine units, the acoustic waves from arbitrary sound source position (x_s, y_s) can be theoretically and numerically confined at any desired position.

Because of high energy conversion efficiency and smaller size at a given resonance frequency, the piezoelectric (PZT-5H) bimorph cantilever with a tip mass[143] is selected and placed in the focusing region of Fig. 3.16(a) to convert the confined acoustic energy into electrical energy. The complete piezoelectric energy converter composed of the cantilever and the load circuit is schematically demonstrated in Fig. 3.16(b). As schematically demonstrated in Fig. 3.16(b), two identical PZT plates with length 30 mm and thickness 2.5 mm are symmetrically attached to a both-ends-clamped shim with length 45 mm and thickness 2.5 mm to construct the PZT bimorph cantilever. A stepped square tungsten block

with length 12 mm is deposited in the middle of the cantilever to work as a tip mass. The minimum size of the confined spot formed by the AMs is slightly larger than the diffraction limit of 50 mm (0.5 λ). Therefore, the dimension of the PZT bimorph cantilever is optimized to be 45 mm by 22 mm, balanced to be large enough to sufficiently catch the confined energy yet small enough to avoid the influence of effectiveness of the acoustic energy confinement. The geometrical parameters of the PZT converter are also carefully tuned to ensure that the fundamental resonating frequency of the system matches the work frequency of the AMs, viz., 3430 Hz. The PZT plates only cover the middle part of the aluminum shim to avoid the charge canceling effect[160], and the tip mass on the top is stepped to minimize its coverage area (zero strain area) on the PZT plate. The two PZT plates are connected in series[161] to form an electrical circuit with resistive load. A single vibration mode of the PZT bimorph structure is tuned and selected to match the work frequency of the AMs, and the bimorph cantilever model[161] for series connection of PZT layers could be applied for specific electromechanical coupling and converting analysis. Rigorous and detailed studies on the PZT bimorph cantilevers can be found in the literatures[143, 162].

3.6.2 Acoustic energy harvesting outputs

Commercial finite element analysis (FEA) software COMSOL Multiphysics™ Version 5.2a is utilized to analyze and simulate the AEH system shown in Fig. 3.16. Pressure acoustics, solid mechanics and electrostatics modules are applied for the coupling of the acoustic, mechanical and electrostatic fields, and the resistive load circuit is simulated by the electrical circuit module. The density and Young's modulus of the aluminum plate and tungsten mass for computation are 2700 and 17800 kg/m^3, and 3.6×10^5 and 7×10^4 MPa, respectively. The mechanical damping coefficient of the PZT bimorph system is set as 0.015 for the calculation. According to the aforementioned phase profiles and their discretely realized labyrinthine unit arrays in Fig. 3.16(a), two AMs can be perpendicularly connected to numerically realize the theoretically designed profiles for the reflected wave control.

Parameters	Tungsten	Aluminum
Density (kg/m^3)	17800	2700
Young's modulus (MPa)	3.6×10^5	7×10^4
Poisson ratio	0.28	0.33

Table 3.1 – Parameter values of materials in calculations.

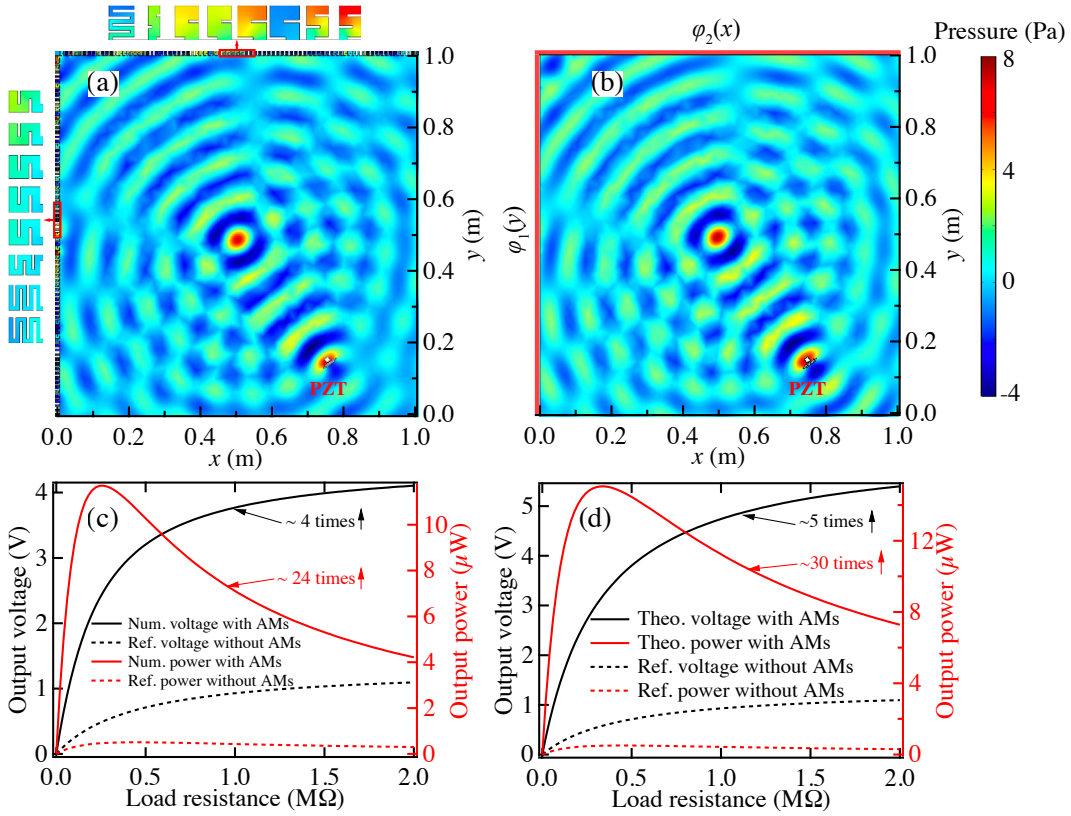

Figure 3.17 – Numerical and simulating results of the AEH system. (a) Numerical sound pressure filed formed by the two-sided multilateral metasurface. (b) Sound pressure field formed by the theoretically designed phase profiles. (c) and (d) are the output voltage and power of multilateral metasurface and theoretical designs, respectively.

As the input parameters, the positions of point sound source and the focusing are arbitrarily set at (0.5 m, 0.5 m) and (0.75 m, 0.16 m), respectively. In this case, the numerically and theoretically acquired results from the AEH system and the

theoretical designs are demonstrated in Fig. 3.17. The numerical result shown in Fig. 3.17(a) is obtained through the simulation of the interaction of metasurface structure and incident waves, and the theoretical result illustrated in Fig. 3.17(b) is acquired through the phase profile analysis in the corresponding boundaries.

As illustrated in Fig. 3.17(a), the sound waves reflected from the metasurface walls are well focused in the designed focusing position (0.75 m, 0.16 m) where the PZT bimorph is positioned. Even though there are some fluctuations in each wave front line caused by the slight phase discontinuity, obvious focusing wave fronts around the designed focusing position (0.75 m, 0.16 m) can be readily observed in Fig. 3.17(a). The specific sound pressure distributions in the sampled labyrinthine units are amplified and demonstrated in the left and upper sides. Theoretical designs with impedance boundaries for desired phase profiles on the sides/frames are highlighted in red in Fig. 3.17(b), and a similar and perfect focusing pattern at (0.75 m, 0.16 m) is observed. The PZT cantilever bimorph is placed around the designed focusing position to convert the acoustic energy into electrical energy.

Because the focusing region is small and the PZT bimorph system shown in Fig. 3.16(b) presents narrow directivity property, the specific position and the angle of the PZT bimorph are sufficiently and carefully swept to maximize the output voltage and power. The electrical outputs from numerical and theoretical AEH systems are demonstrated in Fig. 3.17(c) and 3.17(d), respectively. The referenced output voltages (see dashed black lines) and powers (see dashed red lines) shown in Fig. 3.17(c) and 3.17(d) are obtained from the same PZT cantilever bimorph at the same position (0.75 m, 0.16 m) in the free sound field without AMs or theoretical designs in the boundaries.

The volume flow rate out from the point sound source is set to be 5×10^{-4} m^2/s for all the cases. As demonstrated in Fig. 3.17(c), the output voltage evolution curve (see black solid line) increases with the load resistance until reaching saturation, while the output power (see red solid line) increases with the load resistance to a peak and then decreases. The same trends can be observed in theoretical results shown in Fig. 3.17(d). The maximum output voltages can reach 4 V and 5 V for numerical and theoretical cases, which are about 4 and 5 times of the referenced voltages. The maximum output powers are 12 μW and 15

μW for numerical and theoretical cases, which are about 24 and 30 times of the referenced powers. The small difference between the numerical and theoretical output results can be explained by the phase discontinuity and a small amount of energy retained within the labyrinthine cavities.

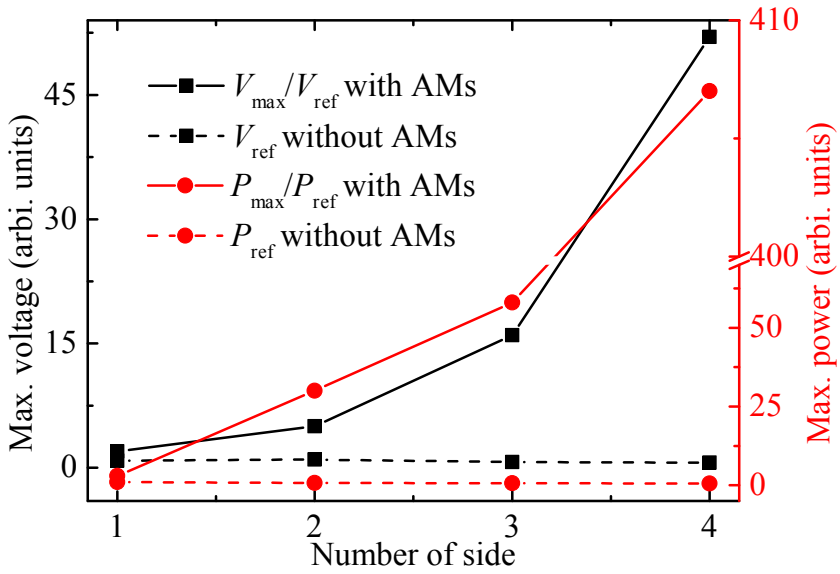

Figure 3.18 – Amplified and intensified output voltage and power from the AEH system with increasing degree of enclosure from one to four sides.

Figure 3.17 provides one specific example of an AEH system with two-sided AMs and the structured PZT bimorph converter. The AM configurations can be extended to three and four sided cases. For better comparison, the AEH system with one-sided metasurface is also calculated, and all the maximum output powers and voltages for the corresponding configurations are obtained and demonstrated in Fig. 3.18. The maximum output voltage V_{max} (solid black line with squares) and power P_{max} (solid red line with circles) ratios with AMs to those without (dashed black line with squares V_{ref} and dashed red line with circles P_{ref}) increase with the number of side of the AEH system. The maximum electrical outputs are achieved in the case of four-sided multilateral AEH system, and the output voltage and power are 52 and 407 times higher than those without AMs, respectively.

3.7 Summary and conclusions

Based on the fundamental idea of coiling up space and generalized Snell's law in the scope of acoustics, an innovative concept of acoustic focusing and energy confinement with multilateral metasurfaces composed of labyrinthine elements has been proposed. Multilateral metasurfaces with various sides from two to four and different geometrical configurations are theoretically and numerically investigated and validated in great details in terms of acoustic focusing and energy confinement. The mechanisms of the standing wave resonance and other interferences caused by multiple reflections from metasurface walls are qualitatively explored and discussed based on the numerical simulation results. The results show first that all the proposed multilateral metasurfaces illustrate excellent performances in acoustic focusing and energy confinement, and second that the maximum confined intensities of each system increase with the degree of the enclosure of the multilateral metasurfaces. Both the completely controllable premier reflection and the multiple reflections that follow are coupled and corporately contribute to the acoustic focusing and energy confinement. Time domain studies of the two-sided metasurfaces have been conducted to further validate the suppositions of the coupling of the focusing waves and multiple reflections. Furthermore, the standing wave resonance and other types of interfering effects caused by multiple reflections lead to the uneven spatial intensity distributions of the metasurface systems.

The mappings of the acoustic intensity distribution for all the proposed multilateral metasurfaces should provide a worthwhile and practical guide for the further AEH applications. The thermo-viscous effects existing in labyrinthine elements on phase shift and reflected sound pressure are sufficiently investigated. The thermoviscous effects result in very little phase variations. Eight elements with different configurations are optimally selected to avoid their resonant status, thus ensuring high reflections. The innovative multilateral metasurfaces with variable configurations demonstrate strong acoustic focusing capabilities and flexibilities in terms of acoustic energy confinement, which should be ideal candidates for AEH under various situations when the acoustic energy conversion aspect is handled.

As one of the potential applications of the proposed reflective metasurfaces, an innovative AEH system composed of the multilateral metasurfaces and a structured PZT bimorph cantilever has been proposed in the final section. The case of two-sided AM energy harvester is intensively studied and demonstrated. As exemplified in Fig. 3.17, an output voltage of 4.2 V and a power of 11.7 μW are acquired with a two-sided multilateral metasurface AEH system. Compared with the output results of AEH systems constructed by various metasurface configurations, the output voltage and power increase with enclosure degrees of the AEH system. The maximum output voltage and power 52 and 407 times higher than those under the case without AM can be obtained with AEH system with enclosed AMs configuration.

Because of its easy fabrication, good flexibility, and arbitrary wave manipulations in spatial dimension, the proposed AEH system based on multilateral AMs and a piezoelectric bimorph converter should be readily applicable for micro energy production and ideally work as power source for public or private micro/nano devices in a large variety of partially or completely enclosed space environments. In order to further explore the properties and features for practical applications, metasurfaces based on new mechanism, i.e., local resonance, besides the coiling-up-space concept, will be introduced and sufficiently investigated in the following chapter. Moreover, the 2D metasurface system will be extended into 3D case and be specified for real situations.

La science a fait de nous des dieux avant même que nous méritions d'être des hommes.

Jean Rostand

Chapter 4

Three-dimensional metasurfaces for energy confinement

Contents

An advanced concept of reflective acoustic focusing based on an ultrathin metasurface is numerically and analytically investigated in this chapter. We propose a reflective metasurface of $\lambda/15$ thick, with λ being wavelength, composed of locally resonant Helmholtz-like elements which discretely realize the 2π phase shift. The theoretical design based on the generalized Snell's law is numerically achieved by the proposed ultrathin metasurface. Numerical simulations and theoretical analysis have converged to a good consensus and validated the ultrathin reflective metasurface concept for acoustic focusing. Furthermore, the

previously reported reflective metasurface with sub-wavelength thickness ($\lambda/8$) and based on the coiling-up-space concept constructed by three-dimensional (3D) labyrinthine elements is investigated and compared to the ultrathin one. Despite both metasurfaces illustrating equivalent good performances for acoustic focusing, the ultrathin one demonstrates its superiority with thinner thickness, simpler design and easier fabrication, which would greatly facilitate its real implementation in relevant applications.

4.1 Introduction

Acoustic focusing has broad applications in the fields of biomedical imaging, ultrasound therapy, acoustic microscopy and nondestructive testing. In order to break the limited focusing resolution, difference-frequency method[163] illustrates capability to realize the sub-wavelength focusing, while the method shows a deficiency of very low efficiency. Based on time-reversal mirrors[164], another super-focusing method is able to achieve a sub-wavelength focusing spot. With considering the negative refractive index and taking advantage of the evanescent wave, the concept of perfect lens overcoming the diffraction limit[165, 166] has inspired and propelled the evolution of various super-lenses[167, 168] and hyper-lenses[169, 170] thereafter. The vigorous development of the phononic crystals and elastic/acoustic metamaterials[30, 31, 34, 39, 44, 171] with anomalous features and exotic capabilities has favorably enabled various kinds of wave manipulations[32, 63, 146, 149, 155, 172]. Advanced and unconventional acoustic lenses[147, 148, 173, 174] achieved by these artificial materials have intrigued compelling research interest due to their revolutionary potential in imaging and focusing applications.

As a novel branch of metamaterials, acoustic metasurfaces (AMSs) demonstrate sub-wavelength or ultrathin features, and thus possess additional capabilities and flexibilities in sound wave manipulations[175], such as diffusion[56], unidirectional transmission[176], lensing[146, 153, 177], absorption[108], wave focusing[178–180], etc. In general, acoustic wave manipulations are realized by predefining the phase distributions of the wavefronts, which can be theoretically achieved by the generalized Snell's law[68]. The continuous theoretical phase dis-

tributions for designed wave manipulations can be discretized and represented by the AMSs composed of elements with individual phases arranged in the due order. In the scope of reflected acoustic wave tailoring, the elements capable of complete and discrete 2π phase shifts of the reflected waves are selected to construct the AMSs. Based on the concept of coiling up space, the thickness of the phase elements can be greatly reduced to the scale of subwavelength. Labyrinthine elements with a thickness of $\lambda/8$, with λ being wavelength, are utilized as candidates to construct the AMSs for acoustic wave focusing[74, 178] and acoustic energy harvesting (AEH)[130, 179]. In order to achieve thinner and more practical AMSs for acoustic focusing and energy confinement, in this chapter, Helmholtz-like elements with a thickness of $\lambda/15$ based on locally resonant mechanism [56] are designed and applied to construct an ultrathin acoustic metasurface (Helmholtz-like metasurface). The previously proposed acoustic metasurfaces[178] composed of labyrinthine elements (labyrinthine metasurface) for acoustic focusing are in the first time extended from two-dimensional (2D) design into three-dimensional (3D) situation, and the results are compared with those of the ultrathin metasurface under plane wave incidence. The ultrathin acoustic metasurface possesses advantages over the labyrinthine one in thinner thickness and easier fabrication, even though both results illustrate equally good acoustic focusing and energy confinement. With negligible thermoviscous dissipation under airborne condition, the proposed ultrathin acoustic metasurface demonstrates strong capability and flexibility in acoustic focusing and energy confinement[181], which would greatly favor the practical acoustic focusing and its related applications, such as acoustic imaging, AEH and acoustic lenses, especially in low frequency situations.

In what follows, we theoretically demonstrate the phase profile of a sampled ultrathin metasurface for reflected wave focusing and the numerical way to realize it in Sec. 4.2. Then, the results of the ultrathin acoustic metasurface in Sec. 4.3.1 and the labyrinthine metasurface in Sec. 4.3.2, are sufficiently investigated and analyzed to acquire their corresponding acoustic focusing and confinement properties and performances. The phase deviations and reflection coefficients of the labyrinthine and Helmholtz-like elements caused by the thermoviscous effects are numerically explored and carefully compared in Sec.

4.3.3. We then conclude and outlook this chapter in Sec. 4.4.

4.2 Method and Design

Based on the mechanism of local resonance, Helmholtz-like elements are selected as candidates to shift the phase fronts of the reflected waves. For locally resonant elements, the phase of reflected wave varies drastically around the resonant frequency. Therefore, a small and successive modification in the geometry of

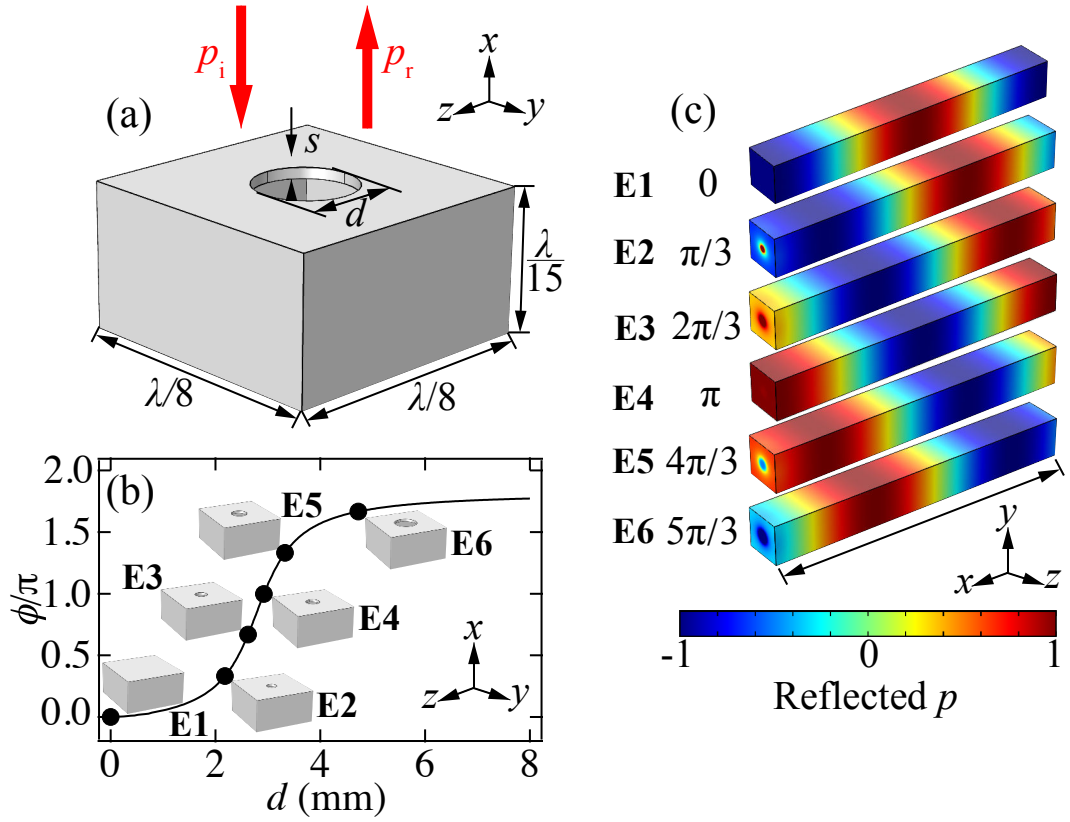

Figure 4.1 – Locally resonant phase-shift elements. (a) Sketch of a typical Helmholtz-like element with a thickness of $\lambda/15$. (b) Reflected phase shift curve as function of the neck diameter d and the six elements with certain diameters selected for individual phase shift. (c) Normalized reflected sound pressure field shifted by the six Helmholtz-like elements to cover 0 - 2π range.

the Helmholtz-like element can continuously and completely tune the phase shift to 2π range. A sampled Helmholtz-like element structure with neck diameter

d and length s for reflected wave manipulation is illustrated in Fig. 4.1(a), and the incident and reflected waves are working in vertical direction x. In order to obtain a succinct wavelength, the work frequency is selected as 3430 Hz for all the numerical simulations and theoretical calculations in this chapter. The sound velocity in air is 343 m/s and thus the wavelength is $\lambda = 0.1$ m. The length and width of the elements are fixed to be 0.0125 m ($\lambda/8$) to maintain a constant phase shift resolution in yz-plane. The work frequency of interest can be readily tuned through rescaling the geometries of the elements. In view of the larger thermoviscous effects on thinner Helmholtz-like elements illustrated in Fig. 4.2(b), the thickness of all the elements is optimally set to be $\lambda/15$ to minimize the thermoviscous dissipation and to ensure the ultrathin property of the resulting metasurface, simultaneously.

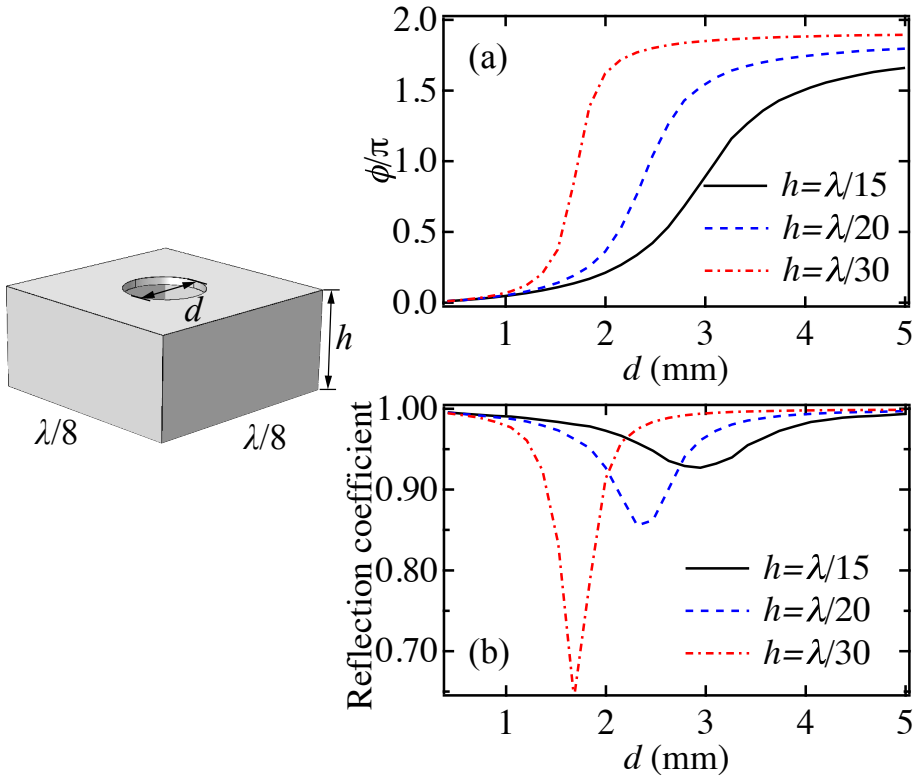

Figure 4.2 – Phase shift and reflection coefficient of a Helmholtz-like element with varying geometries. Phase shift (a) and reflection coefficient (b) curves of Helmholtz-like elements with various thicknesses and diameters.

As can be seen in Fig. 4.2, the thickness of the element can further go down to $\lambda/30$ with sacrificing a portion of acoustic reflections, while maintaining the capability of 2π phase shift. The thicknesses s of the neck length and other walls of all the elements are equally set as 0.5 mm ($\lambda/200$). Therefore, the neck diameter d is the singular parameter readily adjustable for the reflected phase shift control, which simplifies the element fabrication and facilitate its practical application. As illustrated in Fig. 4.1(b), the reflected phase shift evolution curve (see the back line) towards the neck diameter d continuously and monotonically covers 0 to 2π range. Six elements (E1-E6) with various neck diameters shown in Fig. 4.1(b) as solid black squares are selected to evenly and completely discretize the 2π phase shift with a resolution of $\pi/3$. The phase shift performances of all the six selected Helmholtz-like elements are numerically investigated and sequentially demonstrated in Fig. 4.1(c). As shown in the latter, the incident acoustic waves are impinging from the right ends, and the volumetric reflected acoustic fields with one wavelength (0.1 m) formed by the elements illustrated in the left side are sequentially arrayed for better phase shift demonstration. In Fig. 4.1(c), the selected Helmholtz-like elements gradually and completely shift the phase of the reflected waves from 0 to 2π range with a resolution of $\pi/3$ as designed.

The concept for acoustic energy confinement is to control and focus the reflected acoustic waves to any desired spatial position. Both numerical and theoretical methods are applied for the reflected wave confinement. A general schematic diagram of the theoretical design for acoustic energy confinement and its numerical realization by a metasurface composed of Helmholtz-like elements is illustrated in Fig. 4.3(a). According to the generalized Snell's law, the phase distribution $\phi(y,z)$ at $x = 0$ plane required for reflected wave focusing at any designed focusing position $(x_\mathrm{f}, y_\mathrm{f}, z_\mathrm{f})$ under plane wave incidence from the right $(+x)$ direction can be expressed as,

$$\phi(y,z) = k\left[\sqrt{x_\mathrm{f}^2 + (y-y_\mathrm{f})^2 + (z-z_\mathrm{f})^2} - x_\mathrm{f}\right] \tag{4.1}$$

where k is the wave number. The reflected acoustic wave focusing and energy confinement can be theoretically achieved through modifying the acoustic boundary

impedance Z_s at $x = 0$ plane with the phase distribution $\phi(y,z)$ acquired in Eq. 4.1,

$$Z_s = -i\rho_0 c_0 \cot[\phi(y,z)/2] \tag{4.2}$$

where $\rho_0 c_0$ is the acoustic impedance in air.

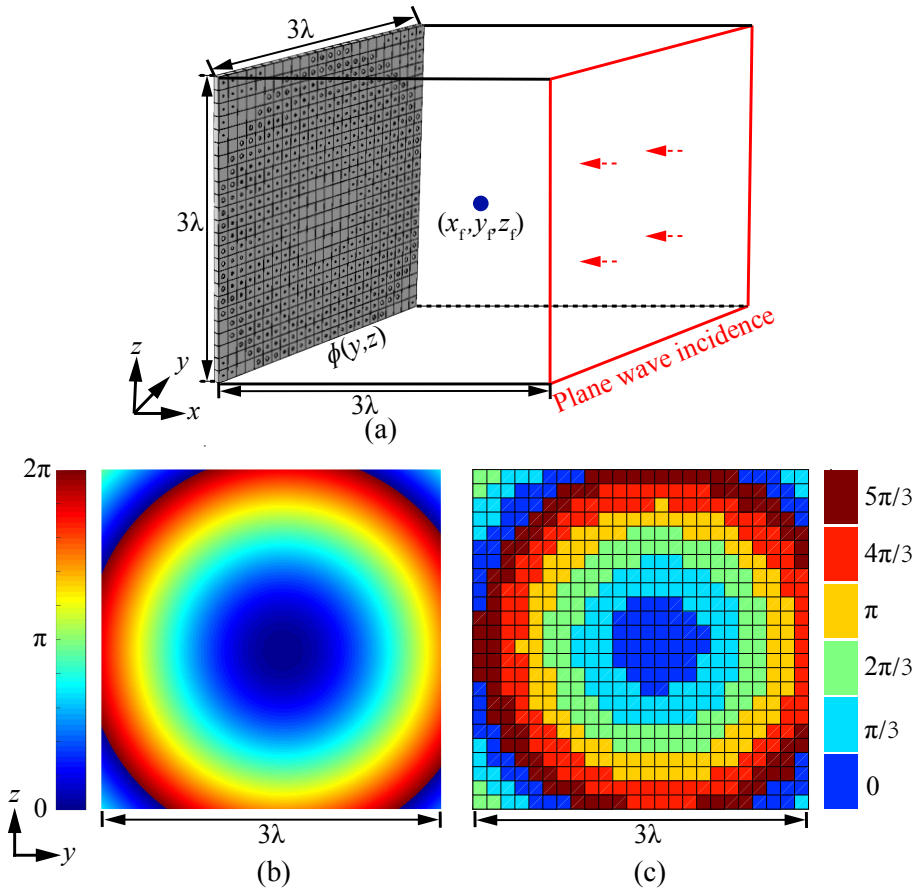

Figure 4.3 – Numerical metasurface constructed by Helmholtz-like elements and theoretical phase designs. (a) Schematic demonstration of theoretically designed $\phi(y,z)$ and metasurface-based acoustic energy confinement system constructed by the six kinds of Helmholtz-like elements for acoustic focusing at arbitrarily designed position (x_f, y_f, z_f) under plane wave incidence from the right $(+x)$ direction. The theoretical (b) and the numerically discretized (c) phase mappings in the zy-plane for a specific focusing position (0.09 m, 0.16 m, 0.14 m).

In the numerical design, a metasurface placed in zy-plane shown in Fig. 4.3(a) with a length/width of 3λ and a thickness of $\lambda/15$ is constructed by 24×24 Helmholtz-like elements. It is worth noting that the geometrical sizes of the metasurface can be readily scalable to meet different application requirements. In Fig. 4.3(a), plane waves impinging from the right ($+x$) direction are reflected and focused at the designed position (x_f, y_f, z_f).

An exemplary focusing position is arbitrarily selected as (0.09 m, 0.16 m, 0.14 m) or $(0.9\lambda, 1.6\lambda, 1.4\lambda)$. The theoretically designed phase distribution of the reflected waves in the $x = 0$ plane for the acoustic focusing and confinement at the selected position is illustrated in Fig. 4.3(b), and the phase profile continuously shifts within the range of 0 to 2π. In Fig. 4.3(c), the theoretical phase distribution shown in Fig. 4.3(b) is equally discretized with a resolution of $\pi/3$, which can be numerically represented by the six kinds of Helmholtz elements shown in Fig. 4.1. Since the size of the designed phase plane is 3λ×3λ and the width of the Helmholtz-like elements is $\lambda/8$, and thus 24×24 elements are applied to construct the metasurface.

4.3 Results and Discussion

Commercial finite element analysis (FEA) software COMSOL Multiphysics™ Version 5.3a is used to analyze and simulate the metasurfaces composed of the Helmholtz-like and the labyrinthine elements, and their thermoviscous properties in this chapter. Pressure acoustics module is applied to simulate the elements in Fig. 4.1, Fig. 4.2 and the metasurface systems. The sides without metasurfaces are set as perfectly matched layers (PML), and hard boundary condition is applied for all the air-solid interfaces. The modules of thermoviscous acoustics, pressure acoustics, and solid mechanics are utilized to investigate the airborne thermoviscous effects of these two types of element cells. In order to acquire the acoustic focusing properties and compare the performances of these two metasurfaces, acoustic intensity fields and the effects of thermovicous dissipations on labyrinthine and Helmholtz-like elements are investigated and analyzed.

4.3.1 Ultrathin metasurface constructed by Helmholtz-like elements

As the input parameter, the focusing position (x_f, y_f, z_f) is arbitrarily set as (0.09 m, 0.16 m, 0.14 m) or (0.9λ, 1.6λ, 1.4λ). The incident pressure p_{in} is set as 1 Pa. In this case, the theoretically and numerically acquired results from the metasurface system and the theoretical design in Fig. 4.3 are demonstrated in Fig. 4.4.

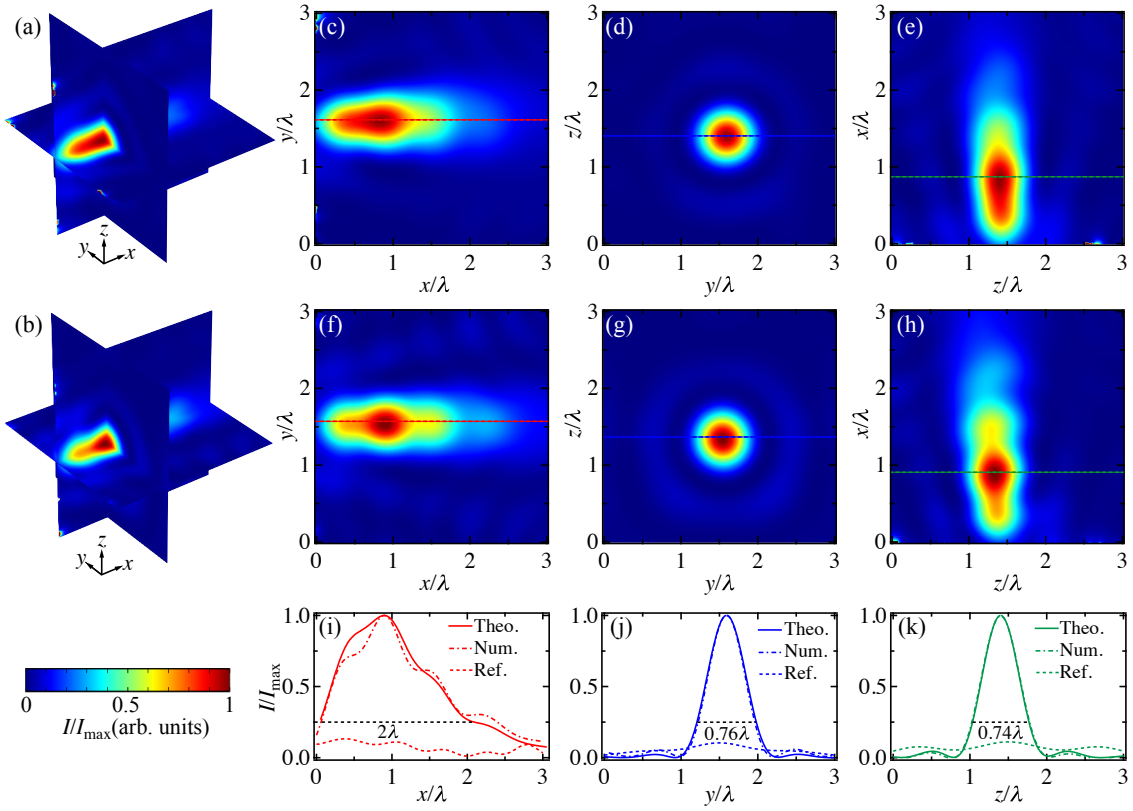

Figure 4.4 – Theoretical and numerical focusing results. Normalized theoretical (a) and numerical (b) reflected sound-intensity field slices along $x = 0.9\lambda, y = 1.6\lambda$ and $z = 1.4\lambda$. (c)-(e) are the theoretical sound reflected intensity fields of the yx, zy and xz planes, respectively. (f)-(h) are the theoretical sound reflected intensity fields of the yx, zy and xz planes, respectively. (i)-(k) are the theoretical, numerical and referenced intensity curves along the three cross-section lines shown in (c)-(h), respectively.

The theoretical result illustrated in Fig. 4.4(a) is acquired through the phase

shift analysis in the corresponding boundary, and the numerical result shown in Fig. 4.4(b) is obtained through the simulation of the interaction of metasurface structure and incident waves. The overviews of the theoretical and numerical reflected sound intensity I along the slices $x = 0.9\lambda, y = 1.6\lambda$ and $z = 1.4\lambda$ are normalized to the maximum value I_{max} and demonstrated in Figs. 4.4(a) and 4.4(b), respectively.

The detailed theoretically and numerically acquired intensity distributions of the slices are illustrated in Figs. 4.4(c)-4.4(e) and 4.4(f)-4.4(h), respectively. In the case of theoretical design with boundary impedance for desired phase distribution at $x = 0$ plane, perfect focusing patterns along these three planes are observed in Figs. 4.4(c)-4.4(e). Even though there are some small fluctuations caused by the phase discontinuity in the numerical results, obvious focusing spots can be readily observed in Figs. 4.4(f)-4.4(h). In order to quantitatively examine and analyze the performance for the designs, the normalized theoretically and numerically confined sound intensities along the cross-section lines of each two slices are plotted and compared with those under the free-field incidence (reference) in Figs. 4.4(i)-4.4(k). The theoretical, numerical and referenced intensity curves are plotted as solid, dash-dotted and dashed lines, and the colors red, blue and green stand for the results in yx, zy and xz planes, respectively. Numerical and theoretical results reach a good consensus in spite of a small deviation due to the phase discretization in numerical simulation. The sizes of the focus in three dimensions are calculated with 3-dB attenuation of sound pressure $|p|$, that is, 1/4 of the intensity. The focused spot sizes acquired theoretically along the lines in x, y and z directions are about 2λ, 0.76λ and 0.74λ, respectively. The full width at half maximum (FWHM) obtained by Helmholtz metasurface and theoretical design is around 0.75 λ, which demonstrates satisfactory focusing quality. Moreover, the confined sound intensities in the focusing region are around 10 times of the referenced values. These results validate that the incident plane waves manipulated by the theoretical boundary and the corresponding metasurface wall are well focused in the designed focusing position (0.09 m, 0.16 m, 0.14 m).

In addition to the single-sided metasurface, the configuration can be also realized in the two-sided case. As illustrated in Fig. 4.5(a), the plane waves are

impinging from $+x$ and $+y$ directions, and the focusing position is arbitrarily set at (x_f, y_f, z_f). The two-sided metasurface can be constructed by achieving the phase distributions in the $y = 0$ and $x = 0$ planes for the designed focusing with Helmholtz-like phase-shift elements shown in Fig. 4.1.

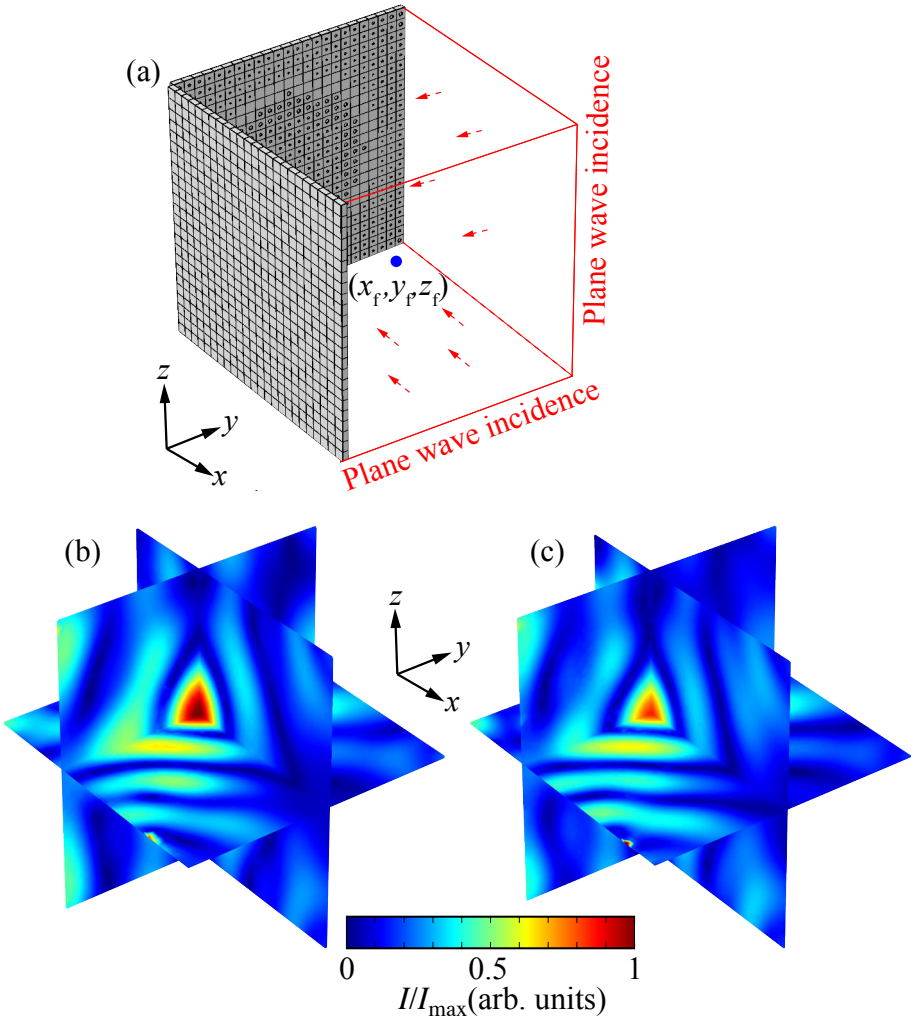

Figure 4.5 – Two-sided 3D metasurface and results. (a) Schematic demonstration of a two-sided 3D metsurface constructed by the six kinds of Helmholtz-like elements for acoustic focusing at arbitrarily designed position (x_f, y_f, z_f) under plane wave incidence from $+x$ and $+y$ directions. The theoretical (b) and the numerical (c) results for a specific focusing position (0.15 m, 0.2 m, 0.15 m).

The reflected intensity fields normalized to the maximum value along the slices $x = 0.15$ m, $y = 0.2$ m, $z = 0.15$ m achieved by theoretical impedance design

in the boundaries $y = 0$ and $x = 0$ planes and by the two-sided metasurface composed of Helmholtz elements are demonstrated in Fig. 4.5(b) and 4.5(c), respectively. Both theoretical and numerical results agree well with each other and show strong focusing at the designed position (0.15 m, 0.2 m, 0.15 m). The validation of two-sided 3D metasurface for sound confinement further prove its practical AEH in various spaces. The maximum confined sound intensity is around three times of that acquired by the single metasurface configuration. In addition to capturing more impinging sound waves, the coupling effect of the two metasurface walls and and the multiple reflections in between could explain the stronger focusing performance.

4.3.2 Comparison of two acoustic metasurface designs

Acoustic metasurfaces composed of the coiling-up-space labyrinthine elements for acoustic focusing and energy confinement are sufficiently investigated in 2D fields. The design is extended to 3D case here and the results are compared with those acquired with the metasurface composed of Helmholtz-like elements.

A typical 3D labyrinthine element structure for reflected wave manipulation is illustrated in Fig. 4.6(a), and the incident and reflected waves are working in direction x. The rigid identical bars with length l, width $\lambda/8$ and thickness w from the upper (y-direction) and lower (-y-direction) boundaries are arrayed in parallel with an equal gap g to form a meandering air channel for sufficient wave delay. The labyrinthine element shown in Fig. 4.6(a) is configured in (m, n) = (3, 2), where m and n denote the number of bars from the upper and lower plates (thickness h), respectively. The length, width and height of the eight selected elements are fixed to be 0.0125 m ($\lambda/8$) to maintain the phase shift resolution in yz-plane and sub-wavelength property. The width (w) of the bars is set as 1 mm ($\lambda/100$), and the thickness h of the upper and lower plates for the four (m, n) configurations is set within the range (0.5 mm, 5 mm) or ($\lambda/200$, $\lambda/20$). Through varying the number of the bars, the phase shift curves of four groups of labyrinthine configurations, viz., (3, 2) solid black line, (2, 2) blue dash line, (2, 1) green dash-dot line and (1, 1) red dash-dot-dot line, as function of h are demonstrated in Fig. 4.6(b). As shown in Fig. 4.6(b), these four curves can

readily cover 2π phase shift. In order to minimize the thermoviscous effect, eight labyrinthine elements (open squares and cubes) with minimum bars are optimally selected from the curves to discretely cover 2π phase shift with a resolution of $\pi/4$ in Fig. 4.6(b).

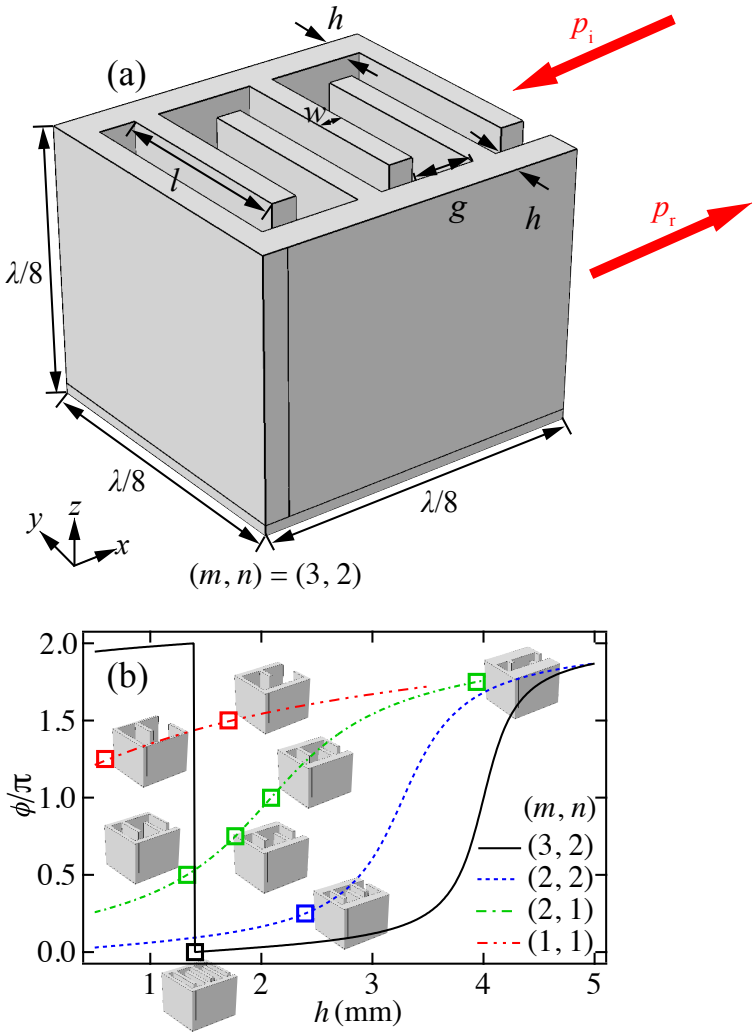

Figure 4.6 – Three-dimensional labyrinthine elements and their phase shifts. (a) Schematic of an exemplary labyrinthine element with (m, n)=(3, 2) and thickness $\lambda/8$. (b) Phase shift profiles of four categories of element configurations and the selected eight elements for phase discretization.

In order to facilitate the comparison, the system design in Fig. 4.7(a) and the phase distribution designed for the focusing at $(0.9\lambda, 1.6\lambda, 1.4\lambda)$ in Fig. 4.7(b)

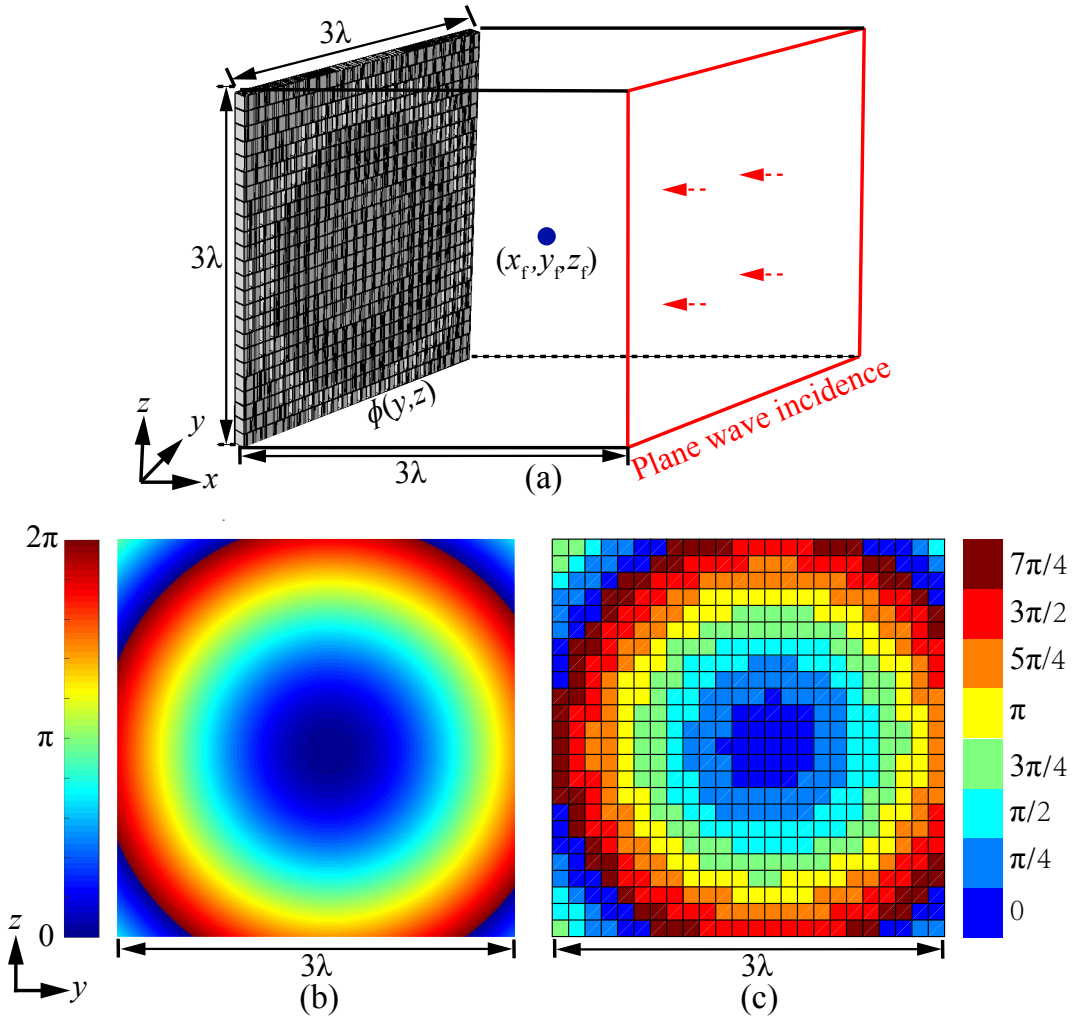

Figure 4.7 – Metasurface constructed by labyrinthine elements and theoretical designs. (a) Schematic demonstration of theoretically designed $\phi(y,z)$ and metasurface-based acoustic energy confinement system constructed by the eight kinds of labyrinthine elements for acoustic focusing at arbitrarily designed position (x_f, y_f, z_f) under plane wave incidence from the right $(+x)$ direction. The theoretical (b) and the numerically discretized (c) phase mappings in the zy-plane for a specific focusing position (0.09 m, 0.16 m, 0.14 m).

are set the same as those in Figs. 4.3(a) and 4.3(b) to focus and confine acoustic waves with the metasurface constructed by the labyrinthine elements shown in Fig. 4.6(b). The input sound pressure of the plane waves and other boundary conditions are set the same as applied in Fig. 4.3(a). Distinct from metasurface

constructed by Helmholtz-like elements in Fig. 4.3(c) with six discretized phases, eight labyrinthine elements with a phase-shift resolution of $\pi/4$ in Fig. 4.6(c) are applied to construct the metasurface shown in Fig. 4.7(a).

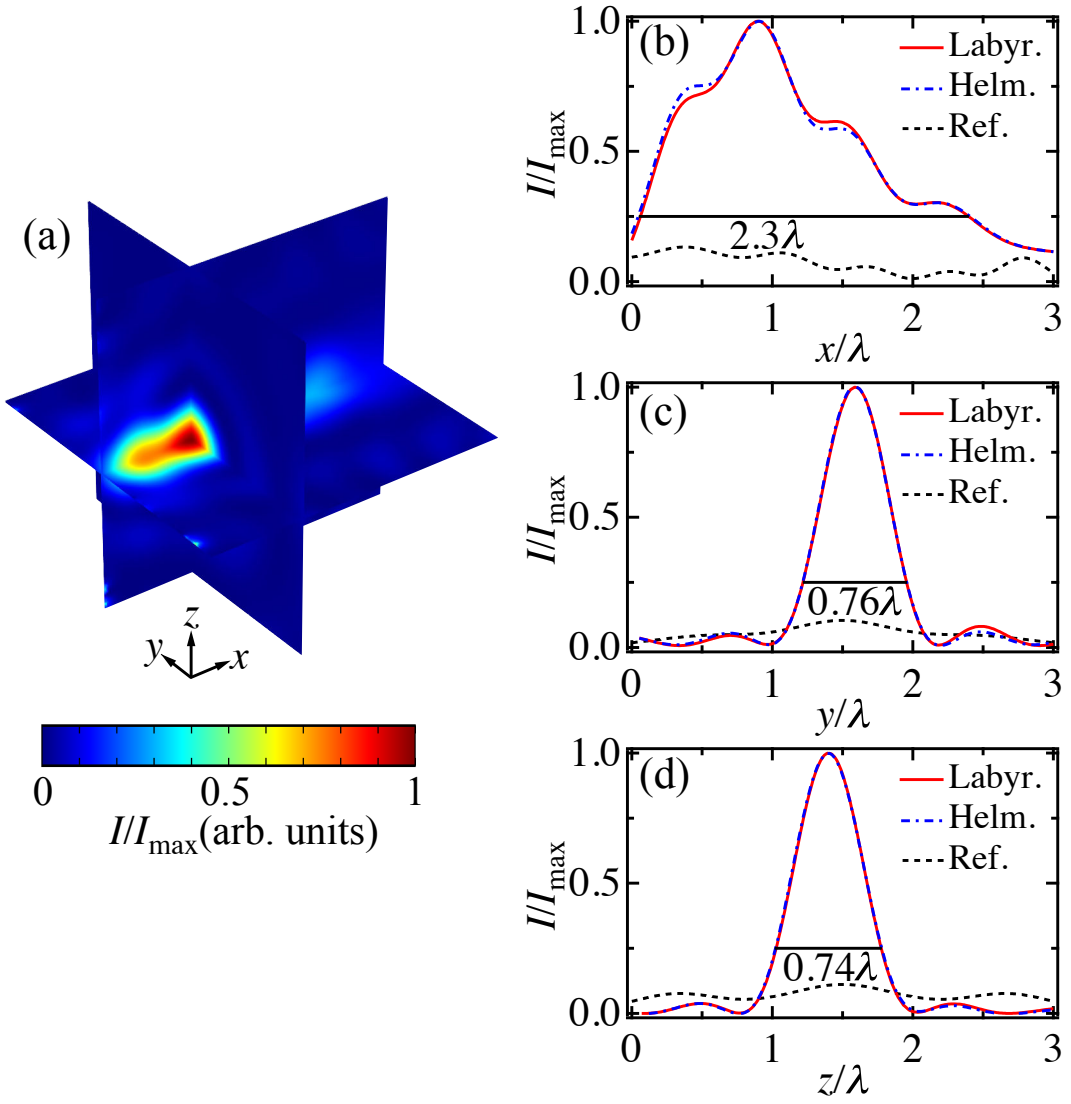

Figure 4.8 – Performance comparison of labyrinthine and Helmholtz metasurfaces. (a) Normalized reflected acoustic intensity field slices along $x = 0.9\lambda, y = 1.6\lambda$ and $z = 1.4\lambda$ achieved by the metasurface composed of labyrinthine elements. (b)-(d) are the intensity curves of the cross-lines of each two slices.

The overview of the reflected sound intensity fields along the slices of $x = 0.9\lambda, y = 1.6\lambda$ and $z = 1.4\lambda$ is normalized to the same maximum value and

illustrated in Fig. 4.8(a). As shown in Figs. 4.8(b)-4.8(d), the normalized sound intensity distributions along the cross-section lines of each two slices obtained by the metasurfaces composed of the labyrinthine elements are compared with those under the metasurface constructed by the Helmholtz-like elements and the free-field boundary (reference) situations. In Figs. 4.8(b)-4.8(d), the sound intensity curves (red solid lines) acquired by the labyrinthine metasurface match well with those (blue dash-dot line) obtained by the Helmholtz-like metasurface, and both results are much larger than the referenced ones (black dashed line) at the designed focusing position. As can be seen in Fig. 4.8, both metasurfaces can well realize the acoustic focusing and energy confinement as desired, and the focused spot sizes acquired by these two metasurface designs along the lines in x, y and z directions are about 2.3λ, 0.76λ and 0.74λ, respectively.

4.3.3 Thermoviscous effects

The thickness of the Helmholtz-like elements can be further reduced without greatly impairing their 2π phase shift capability, and the labyrinthine elements in phase shift group (3, 2) shown in Fig. 4.6(b) alone can completely cover 2π phase shift. However, in real situations, the thickness of the Helmholtz-like elements and the number of bars of the labyrinthine elements should be optimized to minimize potential airborne thermoviscous effects, thus ensuring high acoustic reflection, low acoustic loss and exact phase shift. The modules of Thermoviscous Acoustics, Pressure Acoustics, and Solid Mechanics of the commercial finite element software COMSOL Multiphysics™ Version 5.3a are utilized to systematically and numerically investigate the airborne thermoviscous effects of these two type of element cells.

More specifically, for Helmholtz-like elements, as illustrated in Fig. 4.1 and compared with labyrinthine element situation, phase shift resolution is reduced from $\pi/4$ to $\pi/3$ by selecting fewer number of Helmholtz-like elements, i.e. six, to minimize the airborne absorption caused by the local resonance. The discretized phase distributions with resolution of $\pi/4$ and $\pi/3$ to construct the metasurfaces with Helmholtz-like elements for the same focusing position (0.09 m, 0.16 m, 0.14 m) are provided in Fig. 4.9(a) and 4.9(b), respectively. The

reflected intensity fields along the slices of $x = 0.9\lambda, y = 1.6\lambda$ and $z = 1.4\lambda$ under these two cases are normalized to the maximum value. Comparing Fig. 4.9(d) with 4.9(c), the focusing intensity achieved by the metasurface with decreased phase resolution ($\pi/3$) is higher than that with a resolution of $\pi/4$.

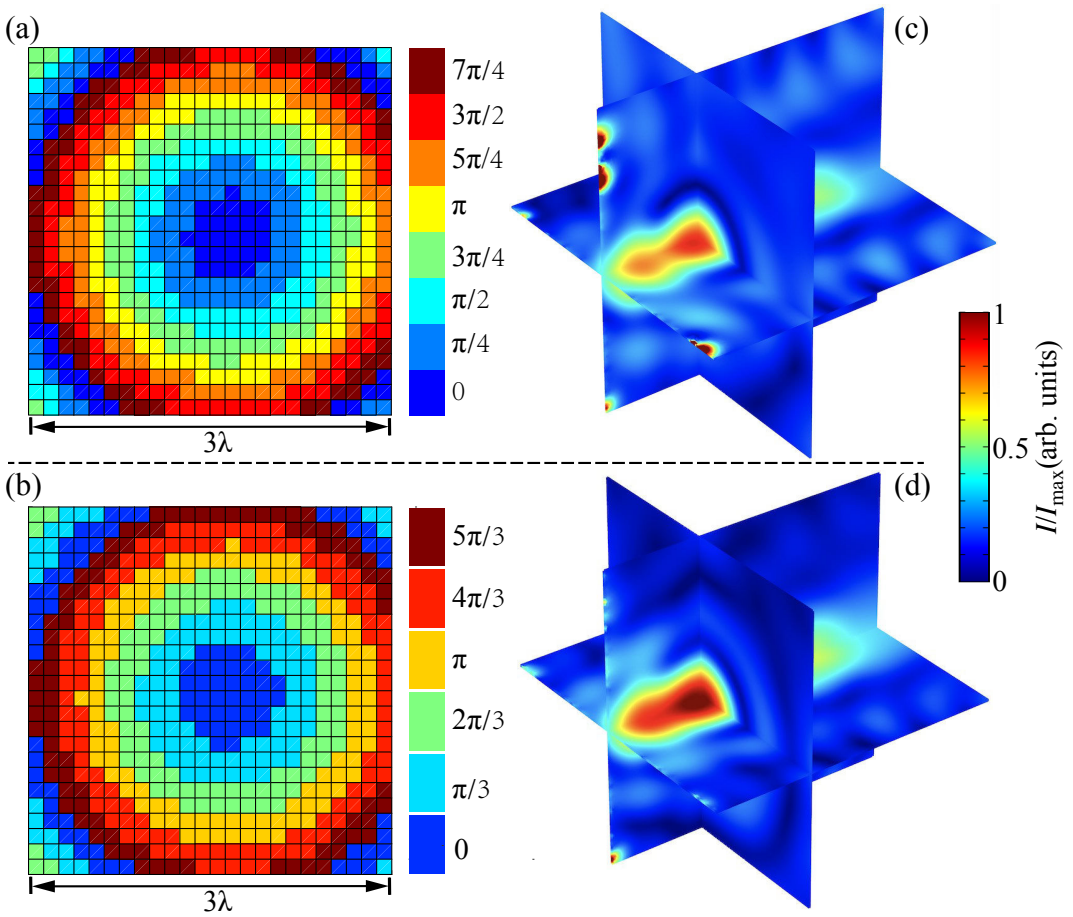

Figure 4.9 – Performances of two Helmholtz metasurfaces with phase-shift resolutions of $\pi/4$ and $\pi/3$. Numerically discretized phase mappings with steps of (a) $\pi/4$ and (b) $\pi/3$ in the zy-plane for a specific focusing position (0.09 m, 0.16 m, 0.14 m). Normalized reflected acoustic intensity field slices along $x = 0.9\lambda, y = 1.6\lambda$ and $z = 1.4\lambda$ achieved by the metasurface composed of Helmholtz-like elements with phase shift resolution (c) $\pi/4$ and (d) $\pi/3$.

For labyrinthine elements, as shown in Fig. 4.6(b), the sound path required for phase shift should be minimized by selecting elements with fewer number of the bars inside, and the width h of the upper and lower plates of the selected

elements should be appropriately set to avoid the structure resonance. The plate thickness h and element configuration (m, n) are two crucial parameters to control the geometries of the meandering air channel inside, which directly determine the viscous property of the element and the resulting metasurface in Fig. 4.10(a). For Helmholtz-like elements, once the thickness of the element is fixed, the neck diameter d of the element is the only parameter to determine its viscous property and the corresponding metasurface in Fig. 4.10(b). Since the thermoviscous effects have a tendency to influence the phase shift and the reflection coefficient of the elements, these two parameters are sufficiently investigated for both types of the metasurface elements.

The thickness of the labyrinthine metasurface in Fig. 4.10(a) $\lambda/8$ is about two times as thick as that of the Helmholtz-like metasurface $\lambda/15$ in Fig. 4.10(b). The phase shift profiles of labyrinthine and the Helmholtz-like elements with (solid lines) and without (dash-dot lines) considering the thermoviscous effects are demonstrated in Figs. 4.10(c) and 4.10(d), respectively. The plate thickness h of the labyrinthine elements under the four configurations (3, 2), (2, 2), (2, 1) and (1, 1) is swept from 0.5 mm to 4.5 mm, and the corresponding phase-shift profiles are plotted in black, blue, green and red in Fig. 4.10(c). Eight labyrinthine elements represented by the open squares from the four groups of the phase shift profiles with certain h values shown in Fig. 4.10(c) are selected to discretely cover the 2π phase shift. The phase-shift deviation (max. 0.02π) of these elements caused by the thermoviscous effects are negligible, compared to the constant phase discretization resolution $\pi/4$. For the Helmholtz-like element situation, the solid circles on the phase profile in Fig. 4.10(d) are the six selected elements, and the phase-shift deviation influenced by thermoviscous effects seems slightly larger yet ignorable, compared to the phase-shift resolution $\pi/3$. It can be seen in Figs. 4.10(c) and 4.10(d) that the phase shift curves with and without thermoviscous effects reach a good consensus, which indicates that airborne thermal viscosity has very limited influence on the designed phase shift of each element. Therefore, the phase-shift deviation and inaccuracy caused by thermoviscous effects in real situations cannot be the main design concern and selection criteria for these two types of elements. Regarding to the metasurfaces for reflected acoustic wave focusing and energy confinement, less

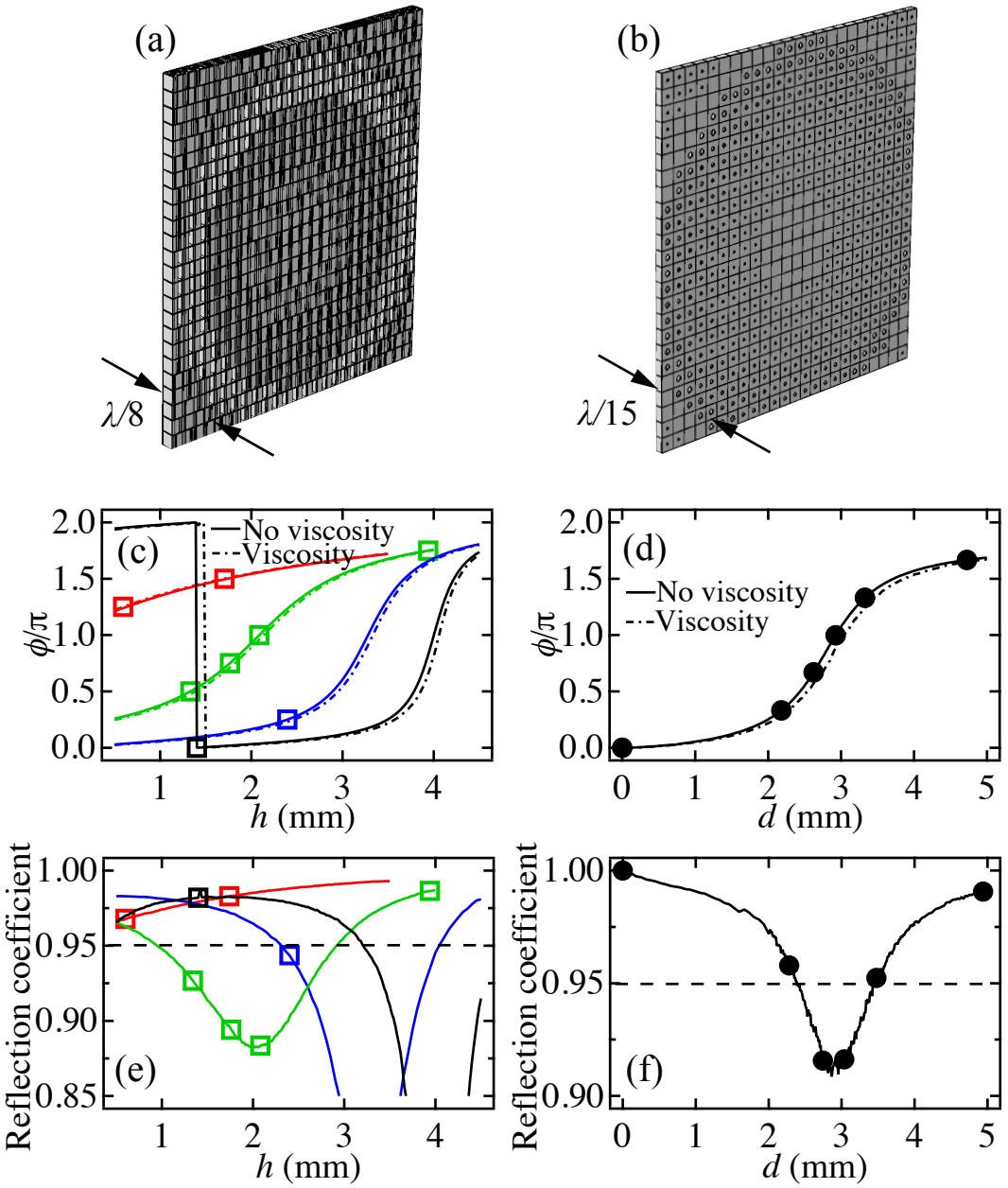

Figure 4.10 – Comparison of thermo-viscous effects on two kinds of metasurfaces. Acoustic metasurfaces composed of (a) labyrinthine and (b) Helmholtz-like elements. Phase shift profiles with and without considering thermoviscous effects for (c) labyrinthine and (d) Helmholtz-like elements. Reflection coefficient curves with and without considering thermoviscous effects for (e) labyrinthine and (f) Helmholtz-like elements. In Figs. 4.10(c) and 4.10(e). the curves of four groups of labyrinthine elements (3, 2), (2, 2), (2, 1) and (1, 1) are plotted in black, blue, green and red, respectively.

acoustic energy dissipation and high reflection are the essential design concerns in real applications.

With considering the thermoviscous effects, the reflection coefficient curves of the four groups of labyrinthine elements (3, 2), (2, 2), (2, 1) and (1, 1) are correspondingly plotted in black, blue, green and red in Fig. 4.10(e). As can be seen in Fig. 4.10(e), the groups of elements with less bars (smaller sum of m and n) possess higher reflection coefficients. The eight labyrinthine elements represented by open squares with less bars and appropriate h values are selected to greatly avoid reflection valleys caused by structure resonance and realize discrete and complete 2π phase shift required by Fig. 4.10(c), simultaneously. The average reflection coefficient of the eight labyrinthine elements is 0.95. In the case of the Helmholtz-like elements, unlike the labyrinthine design, the diameter d is the only parameter adjustable for phase-shift design once the thickness of the elements/metasurface is fixed. Therefore, it is difficult to avoid the reflection coefficient valley and strong resonant absorption in element selection. The thickness of the Helmholtz-like elements/metasurface is set to be $\lambda/15$ in a balanced manner to maintain the ultrathin feature and high reflection coefficient as well. High reflection coefficients of the elements in black line are ensured and observed in Fig. 4.10(f) with the selected thickness. On another hand, the phase shift resolution is reduced from $\pi/4$ to $\pi/3$ to further improve the reflection coefficient by selecting only six Helmholtz-like elements represented by black dots in Fig. 4.10(d) to completely cover the 2π phase shift. As shown in Fig. 4.10(f), the average reflection coefficient of the six elements is about 0.95, equal to that of the Labyrinthine.

4.4 Summary and outlook

Based on generalized Snell's law in the scope of acoustics and locally resonant mechanism, we theoretically propose a concept of acoustic focusing and energy harvesting, and numerically realize it with an ultrathin metasurface composed of Helmholtz-like elements. The confinement acoustic intensity with the ultrathin metasurface system is around ten times of that in the free plane wave field, which indicates effective acoustic focusing and energy confinement with the pro-

posed design. The 2D sub-wavelength metasurface constructed by labyrinthine elements designed with coiling-up-space concept is extended into 3D situation, and its performance in acoustic focusing and thermoviscous property are specifically investigated and compared with the those of ultrathin metasurface. Both metasurface systems can well realize the acoustic focusing and energy confinement at any desired and designed spatial position and achieve the same good performances. The innovative ultrathin metasurface consisting of the locally resonant Helmholtz-like elements evidences, however, its superiority over the labyrinthine metasurface on thinner thickness, simpler design and easier fabrication.

Because of the strong capabilities and flexibilities in acoustic focusing and energy confinement with negligible thermoviscous loss, the proposed ultrathin metasurface system based on Helmholtz-like elements should be practically and broadly applied for various related applications.

General conclusion and perspective

In this dissertation, we have theoretically and numerically proposed two kinds of AEH systems. One is based on the band gap and defect mode of the flawed planar acoustic metamaterials together with PZT patch, and the other is composed of acoustic metasurfaces based on space-coiled or locally resonant concepts and generalized Snell's law. Two 3D acoustic metasurfaces consisting of space-coiled labyrinthine elements and locally resonant Helmholtz-like elements for sound wave focusing and confinement have been compared with details.

Most relevant and up-to-date literatures on acoustic metamaterials, acoustic metasurfaces and acoustic energy harvesting have been sufficiently reviewed in Chap. 1, state of the art. More specifically, the concepts and principles of acoustic metamaterials and metasurfaces are introduced at first, and then their various wave manipulations and applications are elucidated with representative references. Moreover, AEH systems based typical acoustic resonators and AMMs were presented in the first chapter.

Acoustic energy harvesting with a planar AMM

An AEH system based on a defected planar AMM and a PZT patch has been theoretically and numerically proposed and analyzed in Chap. 2. The AEH system can be divided into mechanical part and electrical part. The mechanical part is composed of a defected array of silicone pillars deposited on a thin aluminum plate. The function is to convert impinging sound waves at defect mode frequency into elastic energy and confine it within the defected region. The electrical part consists of a PZT patch attaching to the defected region and the

output electrical load. The task is to transform the strain energy into electricity. A maximum output voltage of 1.3 V and a power density of 0.54 μW/cm^3 were obtained with an acoustic incidence of 2 Pa at the defect mode 2257.5 Hz. The sound to electrical energy conversion efficiency is about 22% from the AEH system under the local optimization. Since there exists a large band gap excluding the defect mode, the AEH system can be applied for sound insulation and noise reduction, simultaneously. Compared with the bulky AEH systems based on acoustic resonators, the planar AEH system excels in competitive power density, ultrathin feature (1/28 of the wavelength), multifunctional applications and construction simplicity. In spite of the advantages mentioned above, there are several future works or ideas worth trying to ameliorate the confinement and conversion efficiency of the AEH system. For instance, the shape, area and the size of supercell and defect configurations of the AMM can be varied and tuned to further improve the AEH efficiency from the aspect of the acoustic-structural coupling. In the aspect of the strain energy conversion, some mass could be added to the PZT patch to reduce the relative displacement to maximize the piezoelectric effect and the electrical outputs. Moreover, there is high sound transmission at the defect mode due to the strong resonant status, and there is a portion of sound energy passing through the AEH system. The AMM plate could be backed with a cavity to maximize the use of the propagating waves and further improve the quality factor. Currently, the planar AMM AEH system has been modeled and analyzed with great details from theoretical and numerical aspects, and the corresponded experimental implementation should be worthwhile.

Acoustic energy harvesting with metasurfaces

In Chap. 3, we have proposed a 2D AEH system composed of multilateral metasurfaces with a PZT bimorph cantilever by taking advantage of the fundamental concept of coiling up space and generalized Snell's law in the scope of acoustics. Multilateral metasurfaces with various sides from two to four and different geometrical configurations are theoretically and numerically investigated and validated with great details in terms of acoustic focusing and energy confinement. The results demonstrate that all the proposed multilateral metasurfaces

illustrate excellent performances in acoustic focusing and energy confinement and the maximum confined intensities of each system increase with the degree of the enclosure of the multilateral metasurfaces. The freely manipulated premier reflection and the multiple reflections that follow are coupled and corporately contribute to the acoustic focusing and energy confinement. Time domain studies of the two-sided metasurfaces have been conducted to further validate the suppositions of the coupling of the focusing waves and multiple reflections. The mappings of the acoustic intensity distribution for all the proposed multilateral metasurfaces should provide a worthwhile and practical guide for the further AEH applications. The thermo-viscous effects existing in labyrinthine elements on phase shift and reflected sound pressure were sufficiently investigated. The thermoviscous effects have very little phase variations, and the elements with optimized reflection were selected. The innovative multilateral metasurfaces with variable configurations demonstrate strong acoustic focusing capabilities and flexibilities in terms of acoustic energy confinement, which should be ideal candidates for AEH under various situations when the acoustic energy conversion aspect is handled. Therefore, we further have implemented an innovative AEH system composed of the proposed multilateral metasurfaces and a structured PZT bimorph cantilever in the final section of this chapter. The case of two-sided acoustic metasurface energy harvester was intensively studied and demonstrated. An output voltage of 4.2 V and a power of 11.7 μW are acquired with a two-sided multilateral metasurface AEH system. Compared with the output results of AEH systems constructed by various metasurface configurations, the output voltage and power increase with enclosure degrees of the AEH system. The maximum output voltage and power 52 and 407 times higher than those under the case without metasurface can be obtained with AEH system under enclosed configuration. Because of its planar feature, great flexibility, and arbitrary wave manipulations in spatial dimension over the AEH systems based on typical resonators, the proposed AEH system based on multilateral metasurfaces and a piezoelectric bimorph converter should be readily applicable for micro energy production and ideally work as power source for public or private micro/nano devices in a large variety of partially or completely enclosed space environments. Compared with the previously mentioned planar AMM

AEH system, the AEH system based on multilateral metasurfaces possesses better flexibility while larger thickness (1/8 of the wavelength). Moreover, the labyrinthine elements in each category constructing the metasurface are unique in design, which increases the fabrication complexity. Therefore, new concepts and mechanisms for simpler and thinner elements for the phase modulation of the reflected waves needed to be explored.

In Chap. 4, the 2D sub-wavelength metasurface constructed by labyrinthine elements designed with coiling-up-space concept applied in Chap. 3 has been extended into 3D situation, and a new 3D acoustic metasurface composed of Helmholtz-like elements for acoustic focusing and energy confinement, based on a different mechanism (local resonance for phase shift), has been proposed and investigated to avoid the issues resulting from space-coiling labyrinthine elements, i.e., simplify the metasurface fabrication and further reduce its thickness. Instead of using eight intricate labyrinthine elements with a thickness of $\lambda/8$, six $\lambda/15$ thick Helmholtz-like elements with a single varying geometrical parameter (width of the neck) have been applied to implement the required phase distribution profile for the focusing. The performance in acoustic focusing and the thermoviscous property of these two metasurfaces composed of labyrinthine and Helmholtz-like elements have been specifically investigated and carefully compared with each other. Both metasurface systems can well realize the acoustic focusing and energy confinement at any desired and designed spatial position with the same good performances. The innovative ultrathin metasurface consisting of the locally resonant Helmholtz-like elements evidences, however, its superiority over the labyrinthine metasurface on thinner thickness, simpler design and easier fabrication. Because of the strong capabilities and flexibilities in acoustic focusing and energy confinement with negligible thermoviscous loss, the ultrathin metasurface system based on Helmholtz-like elements should be practically and broadly applied for various related applications.

In this dissertation, we have mainly conducted the theoretical analysis and numerical simulations for almost all the created models and designs. The corresponded experimental implementations should be highly compelling and worthwhile. Currently, our proposed AEH systems based on acoustic metasurfaces have focused on the reflected wave focusing and energy scavenging, due

to the exempt consideration for impedance matching along the interface. With the emergence of AMMs with perfect impedance match and total transmission, AEH systems based on transmitted wave manipulations and confinement should be equally desirable and worth giving a try. The compelling asymmetrical, nonreciprocal or one-way wave propagating AMM designs based on the non-Hamiltonian concepts of nonlinearity or PT symmetry could be whimsically and justifiably considered for innovative AEH systems, due to their ability to confine waves into half space region (eg., acoustic diode). In addition to the air medium, acoustic and/or acoustoelastic waves or vibrations widely and abundantly exist in underwater and solid environments. Elastic or vibrational energy harvesting have been being a hot topic and widely researched. On the contrary, there is barely reported concepts or designs for underwater acoustic energy scavenging, which, however, could be the next hotspot due to plenty of foreseeable applications. Instead of solely reducing the noise with traditional absorbing materials, smart sound absorbers coupled with microelectronic devices conceived by metamaterials and metasurfaces should be highly promising for various sensing and communication applications.

Bibliography

[1] V. G. Veselago. "The electrodynamics of substances with simultaneously negative values of and μ". In: *Sov. Phys. Usp.* 10 (1968), p. 509.

[2] J. B. Pendry et al. "Extremely low frequency plasmons in metallic mesostructures". In: *Phys. Rev. Lett.* 76 (1996), p. 4773.

[3] E. Yablonovitch. "Inhibited spontaneous emission in solid-state physics and electronics". In: *Phys. Rev. Lett.* 58 (1987), p. 2059.

[4] S. John. "Strong localization of photons in certain disordered dielectric superlattices". In: *Phys. Rev. Lett.* 58 (1987), p. 2486.

[5] M. S. Kushwaha et al. "Acoustic band structure of periodic elastic composites". In: *Phys. Rev. Lett.* 71 (1993), p. 2022.

[6] S. Yang et al. "Focusing of sound in a 3D phononic crystal". In: *Phys. Rev. Lett.* 93 (2004), p. 024301.

[7] J. O. Vasseur et al. "Absolute forbidden bands and waveguiding in two-dimensional phononic crystal plates". In: *Phys. Rev. B* 77 (2008), p. 085415.

[8] J. O. Vasseur et al. "Complete acoustic band gaps in periodic fibre reinforced composite materials: the carbon/epoxy composite and some metallic systems". In: *J. Phys. Condens. Matter* 6 (1994), p. 8759.

[9] M. Torres et al. "Sonic band gaps in finite elastic media: surface states and localization phenomena in linear and point defects". In: *Phys. Rev. Lett.* 82 (1999), p. 3054.

[10] A. Khelif et al. "Transmittivity through straight and stublike waveguides in a two-dimensional phononic crystal". In: *Phys. Rev. B* 65 (2002), p. 174308.

[11] A. Khelif et al. "Transmission and dispersion relations of perfect and defect-containing waveguide structures in phononic band gap materials". In: *Phys. Rev. B* 68 (2003), p. 024302.

[12] J. V. Sánchez-Pérez et al. "Sound Attenuation by a Two-Dimensional Array of Rigid Cylinders". In: *Phys. Rev. Lett.* 80 (1998), p. 5325.

[13] A. Khelif et al. "Trapping and guiding of acoustic waves by defect modes in a full-band-gap ultrasonic crystal". In: *Phys. Rev. B* 68 (2003), p. 214301.

[14] M. Kafesaki, M. M. Sigalas, and N. Garcia. "Frequency modulation in the transmittivity of wave guides in elastic-wave band-gap materials". In: *Phys. Rev. Lett.* 85 (2000), p. 4044.

[15] A. Khelif et al. "Guiding and bending of acoustic waves in highly confined phononic crystal waveguides". In: *Appl. Phys. Lett.* 84 (2004), p. 4400.

[16] Y. Pennec et al. "Tunable filtering and demultiplexing in phononic crystals with hollow cylinders". In: *Phys. Rev. E* 69 (2004), p. 046608.

[17] Y. Pennec et al. "Acoustic channel drop tunneling in a phononic crystal". In: *Appl. Phys. Lett.* 87 (2005), p. 261912.

[18] M. M. Lu et al. "Extraordinary Acoustic Transmission through a 1D Grating with Very Narrow Apertures". In: *Phys. Rev. Lett.* 99 (2007), p. 174301.

[19] L. Feng et al. "Acoustic backward-wave negative refractions in the second band of a sonic crystal". In: *Phys. Rev. Lett.* 96 (2006), p. 014301.

[20] J. Christensen et al. "Collimation of sound assisted by acoustic surface waves". In: *Nat. Phys.* (2007), p. 851.

[21] X. Zhang and Z. Liu. "Extremal Transmission and Beating Effect of Acoustic Waves in Two-Dimensional Sonic Crystals". In: *Phys. Rev. Lett.* 101 (2008), p. 264303.

[22] D. Torrent and J. Sánchez-Dehesa. "Acoustic Analogue of Graphene: Observation of Dirac Cones in Acoustic Surface Waves". In: *Phys. Rev. Lett.* 108 (2012), p. 174301.

[23] S. Y. Yu et al. "Surface phononic graphene". In: *Nat. Mater.* 15 (2016), p. 1243.

[24] L. Lu, J. D. Joannopoulos, and M. Soljačić. "Topological photonics". In: *Nat. Photon.* 8 (2014), p. 821.

[25] M. Xiao et al. "Geometric phase and band inversion in periodic acoustic systems". In: *Nat. Phys.* 11 (2015), p. 240.

[26] Z. Yang et al. "Topological Acoustics". In: *Phys. Rev. Lett.* 114 (2015), p. 114301.

[27] C. He et al. "Acoustic topological insulator and robust one-way sound transport". In: *Nat. Phys.* 12 (2016), p. 1124.

[28] A. Khelif, A. Adibi, et al. *Phononic Crystals*. 2015, p. 23.

[29] T. Still et al. "Simultaneous Occurrence of Structure-Directed and Particle-Resonance-Induced Phononic Gaps in Colloidal Films". In: *Phys. Rev. Lett.* 100 (2008), p. 194301.

[30] Z. Liu et al. "Locally Resonant Sonic Materials". In: *Science* 289 (2000), p. 1734.

[31] M. Oudich et al. "A sonic band gap based on the locally resonant phononic plates with stubs". In: *New J. Phys.* 12 (2010), p. 083049.

[32] M. Oudich, M. B. Assouar, and Z. L. Hou. "Propagation of acoustic waves and waveguiding in a two-dimensional locally resonant phononic crystal plate". In: *Appl. Phys. Lett.* 97 (2010), p. 193503.

[33] M. Oudich et al. "Experimental evidence of locally resonant sonic band gap in two-dimensional phononic stubbed plates". In: *Phys. Rev. B* 84 (2011), p. 165136.

[34] S. A. Cummer, J. Christensen, and A. Alù. "Controlling sound with acoustic metamaterials". In: *Nat. Rev. Mater.* 1 (2016), p. 16001.

[35] G. Ma and P. Sheng. "Acoustic metamaterials: From local resonances to broad horizons". In: *Sci. Adv.* 2 (2016), e1501595.

[36] H. Ge et al. "Breaking the Barriers: Advances in Acoustic Functional Materials". In: *Nat. Sci. Rev.* (2017).

[37] P. M. Morse and K. U. Ingard. *Theoretical acoustics*. Princeton university press, 1968.

[38] Z. Liang and J. Li. "Extreme acoustic metamaterial by coiling up space". In: *Phys. Rev. Lett.* 108 (2012), p. 114301.

[39] J. Li and C. T. Chan. "Double-negative acoustic metamaterial". In: *Phys. Rev. E* 70 (2004), p. 055602.

[40] M. Oudich et al. "Negative effective mass density of acoustic metamaterial plate decorated with low frequency resonant pillars". In: *J. Appl. Phys.* 116 (2014), p. 184504.

[41] Z. Yang et al. "Membrane-Type Acoustic Metamaterial with Negative Dynamic Mass". In: *Phys. Rev. Lett.* 101 (2008), p. 204301.

[42] S. H. Lee et al. "Acoustic metamaterial with negative density". In: *Phys. Lett. A* 373 (2009), p. 4464.

[43] N. Sui et al. "A lightweight yet sound-proof honeycomb acoustic metamaterial". In: *Appl. Phys. Lett.* 106 (2015), p. 171905.

[44] N. Fang et al. "Ultrasonic metamaterials with negative modulus". In: *Nat. Mater.* 5 (2006), p. 452.

[45] S. H. Lee et al. "Composite Acoustic Medium with Simultaneously Negative Density and Modulus". In: *Phys. Rev. Lett.* 104 (2010), p. 054301.

[46] M. R. Haberman and M. D. Guild. "Acoustic metamaterials". In: *Phys. Today* 69 (2016), p. 42.

[47] Y. Xie et al. "Measurement of a Broadband Negative Index with Space-Coiling Acoustic Metamaterials". In: *Phys. Rev. Lett.* 110 (2013), p. 175501.

[48] S. Zhang, C. Xia, and N. Fang. "Broadband Acoustic Cloak for Ultrasound Waves". In: *Phys. Rev. Lett.* 106 (2011), p. 024301.

[49] B. I. Popa, L. Zigoneanu, and S. A. Cummer. "Experimental Acoustic Ground Cloak in Air". In: *Phys. Rev. Lett.* 106 (2011), p. 253901.

[50] L. Zigoneanu, B. I. Popa, and S. A. Cummer. "Three-dimensional broadband omnidirectional acoustic ground cloak". In: *Nat. Mater.* 13 (2014), p. 352.

[51] X. Zhu et al. "$\mathcal{PT}$-Symmetric Acoustics". In: *Phys. Rev. X* 4 (2014), p. 031042.

[52] R. Fleury, D. Sounas, and A. Alù. "An invisible acoustic sensor based on parity-time symmetry". In: *Nat. Commun.* 6 (2015), p. 5905.

[53] C. Shi et al. "Accessing the exceptional points of parity-time symmetric acoustics". In: *Nat. Commun.* 7 (2016), p. 11110.

[54] R. Fleury et al. "Sound Isolation and Giant Linear Nonreciprocity in a Compact Acoustic Circulator". In: *Science* 343 (2014), p. 516.

[55] G. Ma et al. "Acoustic metasurface with hybrid resonances". In: *Nat. Mater.* 13 (2014), p. 873.

[56] Y. F. Zhu et al. "Ultrathin Acoustic Metasurface-Based Schroeder Diffuser". In: *Phys. Rev. X* 7 (2017), p. 021034.

[57] A. N. Norris. "Acoustic cloaking theory". In: *Proc. R. Soc. London A*. Vol. 464. 2008, p. 2411.

[58] A. N. Norris. "Acoustic metafluids". In: *J. Acoust. Soc. Am.* 125 (2009), p. 839.

[59] C. N. Layman et al. "Highly Anisotropic Elements for Acoustic Pentamode Applications". In: *Phys. Rev. Lett.* 111 (2013), p. 024302.

[60] Y. Chen et al. "Broadband solid cloak for underwater acoustics". In: *Phys. Rev. B* 95 (2017), p. 180104.

[61] W. Kan et al. "Acoustic illusion near boundaries of arbitrary curved geometry". In: *Sci. Rep.* 3 (2013), p. 1427.

[62] R. Zhu et al. "Bifunctional acoustic metamaterial lens designed with coordinate transformation". In: *Appl. Phys. Lett.* 110 (2017), p. 113503.

[63] B. Liang et al. "An acoustic rectifier". In: *Nat. Mater.* 9 (2010), p. 989.

[64] B. I. Popa and S. A. Cummer. "Non-reciprocal and highly nonlinear active acoustic metamaterials". In: *Nat. Commun.* 5 (2014), p. 3398.

[65] E. F. Kuester et al. "Averaged transition conditions for electromagnetic fields at a metafilm". In: *IEEE Trans. Antennas Propag.* 51 (2003), p. 2641.

[66] C. L. Holloway et al. "Reflection and transmission properties of a metafilm: With an application to a controllable surface composed of resonant particles". In: *IEEE Trans. Electromag. Compat.* 47 (2005), p. 853.

[67] C. L. Holloway et al. "An overview of the theory and applications of metasurfaces: The two-dimensional equivalents of metamaterials". In: *IEEE Antennas Propag. Mag.* 54 (2012), p. 10.

[68] N. Yu et al. "Light Propagation with Phase Discontinuities: Generalized Laws of Reflection and Refraction". In: *Science* 334 (2011), pp. 333–337.

[69] J. Li et al. "Systematic design and experimental demonstration of bianisotropic metasurfaces for scattering-free manipulation of acoustic wavefronts". In: *Nat. Commun.* 9 (2018), p. 1342.

[70] R. Ghaffarivardavagh et al. "Horn-like space-coiling metamaterials toward simultaneous phase and amplitude modulation". In: *Nat. Commun.* 9 (2018), p. 1349.

[71] Z. Liang and J. Li. "Extreme acoustic metamaterial by coiling up space". In: *Phys. Rev. Lett.* 108 (2012), p. 114301.

[72] Y. Li et al. "Acoustic focusing by coiling up space". In: *Appl. Phys. Lett.* 101 (2012), p. 233508.

[73] Y. Li et al. "Extraordinary acoustic transmission through ultrathin acoustic metamaterials by coiling up space". In: *Appl. Phys. Lett.* 103 (2013), p. 063509.

[74] Y. Li et al. "Experimental Realization of Full Control of Reflected Waves with Subwavelength Acoustic Metasurfaces". In: *Phys. Rev. Applied* 2 (2014), p. 064002.

[75] B. Liu et al. "All-angle Negative Reflection with An Ultrathin Acoustic Gradient Metasurface: Floquet-Bloch Modes Perspective and Experimental Verification". In: *Sci. Rep.* 7 (2017), p. 13852.

[76] C. Shen et al. "A surface impedance-based three-channel acoustic metasurface retroreflector". In: *Appl. Phys. Lett.* 112 (2018), p. 183503.

[77] Y. Li et al. "Reflected wavefront manipulation based on ultrathin planar acoustic metasurfaces". In: *Sci. Rep.* 3 (2013), p. 2546.

[78] W. Wang et al. "Subwavelength diffractive acoustics and wavefront manipulation with a reflective acoustic metasurface". In: *J. Appl. Phys.* 120 (2016), p. 195103.

[79] X. Chen et al. "Implementation of acoustic demultiplexing with membrane-type metasurface in low frequency range". In: *Appl. Phys. Lett.* 110 (2017), p. 161909.

[80] J. Zhao et al. "Manipulating acoustic wavefront by inhomogeneous impedance and steerable extraordinary reflection". In: *Sci. Rep.* 3 (2013), p. 2537.

[81] Y. F. Zhu et al. "Dispersionless manipulation of reflected acoustic wavefront by subwavelength corrugated surface". In: *Sci. Rep.* 5 (2015), p. 10966.

[82] Y. Xie et al. "Wavefront modulation and subwavelength diffractive acoustics with an acoustic metasurface". In: *Nat. Commun.* 5 (2014), p. 5553.

[83] T. Frenzel et al. "Three-dimensional labyrinthine acoustic metamaterials". In: *Appl. Phys. Lett.* 103 (2013), p. 061907.

[84] Y. Xie et al. "Tapered labyrinthine acoustic metamaterials for broadband impedance matching". In: *Appl. Phys. Lett.* 103 (2013), p. 201906.

[85] K. Tang et al. "Anomalous refraction of airborne sound through ultrathin metasurfaces". In: *Sci. Rep.* 4 (2014), p. 6517.

[86] Y. Ding et al. "A broadband acoustic metamaterial with impedance matching layer of gradient index". In: *Appl. Phys. Lett.* 110 (2017), p. 241903.

[87] Y. Li et al. "Metascreen-Based Acoustic Passive Phased Array". In: *Phys. Rev. Applied* 4 (2015), p. 024003.

[88] B. T. Hefner and P. L. Marston. "An acoustical helicoidal wave transducer with applications for the alignment of ultrasonic and underwater systems". In: *J. Acoust. Soc. Am.* 106 (1999), p. 3313.

[89] K. Melde et al. "Holograms for acoustics". In: *Nature* 537.7621 (2016), p. 518.

[90] B. Liang, B. Yuan, and J. C. Cheng. "Acoustic Diode: Rectification of Acoustic Energy Flux in One-Dimensional Systems". In: *Phys. Rev. Lett.* 103 (2009), p. 104301.

[91] X. F. Li et al. "Tunable Unidirectional Sound Propagation through a Sonic-Crystal-Based Acoustic Diode". In: *Phys. Rev. Lett.* 106 (2011), p. 084301.

[92] N. Boechler, G. Theocharis, and C. Daraio. "Bifurcation-based acoustic switching and rectification". In: *Nat. Mater.* 10 (2011), p. 665.

[93] X. Jiang et al. "Acoustic one-way metasurfaces: Asymmetric Phase Modulation of Sound by Subwavelength Layer". In: *Sci. Rep.* 6 (2016).

[94] C. Shen et al. "Asymmetric acoustic transmission through near-zero-index and gradient-index metasurfaces". In: *Appl. Phys. Lett.* 108 (2016), p. 223502.

[95] G. P. Ward et al. "Boundary-Layer Effects on Acoustic Transmission Through Narrow Slit Cavities". In: *Phys. Rev. Lett.* 115 (2015), p. 044302.

[96] J. Christensen et al. "Parity-Time Synthetic Phononic Media". In: *Phys. Rev. Lett.* 116 (20 2016), p. 207601.

[97] K. Ding et al. "Emergence, Coalescence, and Topological Properties of Multiple Exceptional Points and Their Experimental Realization". In: *Phys. Rev. X* 6 (2016), p. 021007.

[98] Y. Li et al. "Tunable Asymmetric Transmission via Lossy Acoustic Metasurfaces". In: *Phys. Rev. Lett.* 119 (2017), p. 035501.

[99] X. Jiang et al. "Convert Acoustic Resonances to Orbital Angular Momentum". In: *Phys. Rev. Lett.* 117 (2016), p. 034301.

[100] J. L. Thomas and R. Marchiano. "Pseudo Angular Momentum and Topological Charge Conservation for Nonlinear Acoustical Vortices". In: *Phys. Rev. Lett.* 91 (2003), p. 244302.

[101] D. Baresch, J. L. Thomas, and R. Marchiano. "Observation of a Single-Beam Gradient Force Acoustical Trap for Elastic Particles: Acoustical Tweezers". In: *Phys. Rev. Lett.* 116 (2016), p. 024301.

[102] A. Riaud et al. "Anisotropic Swirling Surface Acoustic Waves from Inverse Filtering for On-Chip Generation of Acoustic Vortices". In: *Phys. Rev. Applied* 4 (2015), p. 034004.

[103] R. Wunenburger, J. I. V. Lozano, and E. Brasselet. "Acoustic orbital angular momentum transfer to matter by chiral scattering". In: *New J. Phys.* 17 (2015), p. 103022.

[104] Y. Hertzberg and G. Navon. "Bypassing absorbing objects in focused ultrasound using computer generated holographic technique". In: *Med. Phys.* 38 (2011), p. 6407.

[105] A. Marzo et al. "Holographic acoustic elements for manipulation of levitated objects". In: *Nat. Commun.* 6 (2015), p. 8661.

[106] J. P. Arenas and M. J. Crocker. "Recent trends in porous sound-absorbing materials". In: *J. Sound Vib.* 44 (2010), p. 12.

[107] D. Y. Maa. "Potential of microperforated panel absorber". In: *J. Acoust. Soc. Am.* 104.5 (1998), p. 2861.

[108] Y. Li and B. M. Assouar. "Acoustic metasurface-based perfect absorber with deep subwavelength thickness". In: *Appl. Phys. Lett.* 108 (2016), p. 063502.

[109] J. J. Park et al. "Giant acoustic concentration by extraordinary transmission in zero-mass metamaterials". In: *Phys. Rev. lett.* 110 (2013), p. 244302.

[110] X. Cai et al. "Ultrathin low-frequency sound absorbing panels based on coplanar spiral tubes or coplanar Helmholtz resonators". In: *Appl. Phys. Lett.* 105 (2014), p. 121901.

[111] S. P. Beeby, M. J. Tudor, and N. M. White. "Energy harvesting vibration sources for microsystems applications". In: *Meas. Sci. Technol.* 17 (2006), R175.

[112] R. D. Schaller and V. I. Klimov. "High efficiency carrier multiplication in PbSe nanocrystals: implications for solar energy conversion". In: *Phys. Rev. Lett.* 92 (2004), p. 186601.

[113] R. R. King et al. "40% efficient metamorphic GaInP/ GaInAs/ Ge multijunction solar cells". In: *Appl. Phys. Lett.* 90 (2007), p. 183516.

[114] A. Sharma et al. "Review on thermal energy storage with phase change materials and applications". In: *Renew. Sustain. Energ. Rev.* 13 (2009), p. 318.

[115] D. Pant et al. "A review of the substrates used in microbial fuel cells (MFCs) for sustainable energy production". In: *Bioresource Technol.* 101 (2010), p. 1533.

[116] R. L. Harne and K. W. Wang. "A review of the recent research on vibration energy harvesting via bistable systems". In: *Smart Mater. Struct.* 22 (2013), p. 023001.

[117] S. Rafique. *Piezoelectric Vibration Energy Harvesting: Modeling & Experiments*. Springer, 2017.

[118] S. B. Horowitz et al. "A MEMS acoustic energy harvester". In: *J. Micromech. Microeng.* 16 (2006), S174.

[119] B. Li, J. H. You, and Y. J. Kim. "Low frequency acoustic energy harvesting using PZT piezoelectric plates in a straight tube resonator". In: *Smart Mater. Struct.* 22 (2013), p. 055013.

[120] F. Liu et al. "Acoustic energy harvesting using an electromechanical Helmholtz resonator". In: *J. Acoust. Soc. Am.* 123 (2008), p. 1983.

[121] S. Noh, H. Lee, and B. Choi. "A study on the acoustic energy harvesting with Helmholtz resonator and piezoelectric cantilevers". In: *Int. J. Precis. Eng. and Manuf.* 14 (2013), p. 1629.

[122] Izhar and U. K. Farid. "Three degree of freedom acoustic energy harvester using improved Helmholtz resonator". In: *Int. J. Precis. Eng. Manuf.* 19 (2018), p. 143.

[123] C. H. Sohn and J. H. Park. "A comparative study on acoustic damping induced by half-wave, quarter-wave, and Helmholtz resonators". In: *Aerosp. Sci. Technol.* 15 (2011), p. 606.

[124] B. Li et al. "Harvesting low-frequency acoustic energy using quarter-wavelength straight-tube acoustic resonator". In: *Appl. Acoust.* 74 (2013), p. 1271.

[125] W. C. Wang et al. "Acoustic energy harvesting by piezoelectric curved beams in the cavity of a sonic crystal". In: *Smart Mater. Struct.* 19 (2010), p. 045016.

[126] L. Y. Wu, L. W. Chen, and C. M. Liu. "Acoustic energy harvesting using resonant cavity of a sonic crystal". In: *Appl. Phys. Lett.* 95 (2009), p. 013506.

[127] M. Carrara et al. "Metamaterial-inspired structures and concepts for elastoacoustic wave energy harvesting". In: *Smart Mater. Struct.* 22 (2013), p. 065004.

[128] H. Lv et al. "Vibration energy harvesting using a phononic crystal with point defect states". In: *Appl. Phys. Lett.* 102 (2013), p. 034103.

[129] S. Tol, F. L. Degertekin, and A. Erturk. "Phononic crystal Luneburg lens for omnidirectional elastic wave focusing and energy harvesting". In: *Appl. Phys. Lett.* 111 (2017), p. 013503.

[130] K. H. Sun et al. "Sound energy harvesting using a doubly coiled-up acoustic metamaterial cavity". In: *Smart Mater. Struct.* 26 (2017), p. 075011.

[131] B. Parida, S. Iniyan, and R. Goic. "A review of solar photovoltaic technologies". In: *Renew. Sust. Energ. Rev.* 15 (2011), p. 1625.

[132] T. Burton et al. *Wind energy handbook*. 2011.

[133] A. Cuadras, M. Gasulla, and V. Ferrari. "Thermal energy harvesting through pyroelectricity". In: *Sens. Actuators A: Phys.* 158 (2010), p. 132.

[134] B. J. Hansen et al. "Hybrid nanogenerator for concurrently harvesting biomechanical and biochemical energy". In: *ACS Nano* 4 (2010), p. 3647.

[135] F. U. Khan and Izhar. "State of the art in acoustic energy harvesting". In: *J. Micromech. Microeng.* 25 (2015), p. 023001.

[136] B. Li et al. "Harvesting low-frequency acoustic energy using quarter-wavelength straight-tube acoustic resonator". In: *Appl. Acoust.* 74 (2013), p. 1271.

[137] M. Badreddine Assouar et al. "Broadband plate-type acoustic metamaterial for low-frequency sound attenuation". In: *Appl. Phys. Lett.* 101 (2012), p. 173505.

[138] S. Gonella, A. C. To, and W. K. Liu. "Interplay between phononic bandgaps and piezoelectric microstructures for energy harvesting". In: *J. Mechan. Phys. Solids* 57 (2009), p. 621.

[139] M. Oudich, X. Zhou, and M. Badreddine Assouar. "General analytical approach for sound transmission loss analysis through a thick metamaterial plate". In: *J. Appl. Phys.* 116 (2014), p. 193509.

[140] S. Qi et al. "Acoustic energy harvesting based on a planar acoustic metamaterial". In: *Appl. Phys. Lett.* 108 (2016), p. 263501.

[141] M. Oudich and Y. Li. "Tunable sub-wavelength acoustic energy harvesting with a metamaterial plate". In: *J. Phys. D: Appl. Phys.* 50 (2017), p. 315104.

[142] L. Cremer and M. Heckl. *Structure-borne sound: structural vibrations and sound radiation at audio frequencies*. Springer Science & Business Media, 2013.

[143] S. Roundy and P. K. Wright. "A piezoelectric vibration based generator for wireless electronics". In: *Smart Mater. Struct.* 13 (2004), pp. 1131–1142.

[144] V. J. Ovejas and A. Cuadras. "Multimodal piezoelectric wind energy harvesters". In: *Smart Mater. Struct.* 20 (2011), p. 085030.

[145] B. J. Hansen et al. "Hybrid nanogenerator for concurrently harvesting biomechanical and biochemical energy". In: *ACS Nano* 4 (2010), p. 3647.

[146] J. Christensen and F. J. Garcia de Abajo. "Anisotropic metamaterials for full control of acoustic waves". In: *Phys. Rev. Lett.* 108 (2012), p. 124301.

[147] J. Li et al. "Experimental demonstration of an acoustic magnifying hyperlens". In: *Nat. Mater.* 8 (2009), p. 931.

[148] J. Zhu et al. "A holey-structured metamaterial for acoustic deep-subwavelength imaging". In: *Nat. Phys.* 7 (2011), p. 52.

[149] M. H. Lu et al. "Extraordinary acoustic transmission through a 1D grating with very narrow apertures". In: *Phys. Rev. Lett.* 99 (2007), p. 174301.

[150] Z. He et al. "Acoustic transmission enhancement through a periodically structured stiff plate without any opening". In: *Phys. Rev. Lett.* 105 (2010), p. 074301.

[151] J. Mei et al. "Dark acoustic metamaterials as super absorbers for low-frequency sound". In: *Nat. Commun.* 3 (2012), p. 756.

[152] K. Tang et al. "Anomalous refraction of airborne sound through ultrathin metasurfaces". In: *Sci. Rep.* 4 (2014), p. 6517.

[153] W. Wang et al. "Design and demonstration of broadband thin planar diffractive acoustic lenses". In: *Appl. Phys. Lett.* 105 (2014), p. 101904.

[154] Y. Li, S. Qi, and M. B. Assouar. "Theory of metascreen-based acoustic passive phased array". In: *New J. Phys.* 18 (2016), p. 043024.

[155] Y. Li and M. B. Assouar. "Three-dimensional collimated self-accelerating beam through acoustic metascreen". In: *Sci. Rep.* 5 (2015), p. 17612.

[156] C. Shen et al. "Anisotropic Complementary Acoustic Metamaterial for Canceling out Aberrating Layers". In: *Phys. Rev. X* 4 (2014), p. 041033.

[157] M. Farhat et al. "Frequency-selective surface acoustic invisibility for three-dimensional immersed objects". In: *Phys. Rev. B* 86 (2012), p. 174303.

[158] H. Esfahlani et al. "Acoustic carpet cloak based on an ultrathin metasurface". In: *Phys. Rev. B* 94 (2016), p. 014302.

[159] C. Faure et al. "Experiments on metasurface carpet cloaking for audible acoustics". In: *Appl. Phys. Lett.* 108 (2016), p. 064103.

[160] R. Kashyap, T. R. Lenka, and S. Baishya. "A model for doubly clamped piezoelectric energy harvesters with segmented electrodes". In: *IEEE Electron Device Lett.* 36 (2015), p. 1369.

[161] A. Erturk and D. J. Inman. "An experimentally validated bimorph cantilever model for piezoelectric energy harvesting from base excitations". In: *Smart Mater. Struct.* 18 (2009), p. 025009.

[162] J. Ajitsaria et al. "Modeling and analysis of a bimorph piezoelectric cantilever beam for voltage generation". In: *Smart Mater. struct.* 16 (2007), p. 447.

[163] M. Fatemi and J. F. Greenleaf. "Ultrasound-stimulated vibro-acoustic spectrography". In: *Science* 280 (1998), p. 82.

[164] J. de Rosny and M. Fink. "Overcoming the diffraction limit in wave physics using a time-reversal mirror and a novel acoustic sink". In: *Phys. Rev. Lett.* 89 (2002), p. 124301.

[165] E. Betzig and J. K. Trautman. "Near-field optics: microscopy, spectroscopy, and surface modification beyond the diffraction limit". In: *Science* 257 (1992), pp. 189–195.

[166] J. B. Pendry. "Negative refraction makes a perfect lens". In: *Phys. Rev. Lett.* 85 (2000), p. 3966.

[167] N. Fang et al. "Sub-diffraction-limited optical imaging with a silver superlens". In: *Science* 308 (2005), pp. 534–537.

[168] X. Zhou, B. Assouar, and M. Oudich. "Acoustic superfocusing by solid phononic crystals". In: *Appl. Phys. Lett.* 105 (2014), p. 233506.

[169] Z. Liu et al. "Far-field optical hyperlens magnifying sub-diffraction-limited objects". In: *science* 315 (2007), pp. 1686–1686.

[170] D. Lu and Z. Liu. "Hyperlenses and metalenses for far-field super-resolution imaging". In: *Nat. Commun.* 3 (2012), p. 1205.

[171] K. Bertoldi et al. "Flexible mechanical metamaterials". In: *Nat. Rev. Mater.* 2 (2017), p. 17066.

[172] J. H. Oh et al. "Elastic Metamaterial Insulator for Broadband Low-Frequency Flexural Vibration Shielding". In: *Phys. Rev. Applied* 8 (2017), p. 054034.

[173] R. Zhu et al. "Negative refraction of elastic waves at the deep-subwavelength scale in a single-phase metamaterial". In: *Nat. Commun.* 5 (2014), p. 5510.

[174] M. Moleron, M. Serra-Garcia, and C. Daraio. "Acoustic Fresnel lenses with extraordinary transmission". In: *Appl. Phys. Lett.* 105 (2014), p. 114109.

[175] Y. Cheng et al. "Ultra-sparse metasurface for high reflection of low-frequency sound based on artificial Mie resonances". In: *Nat. Mater.* 14 (2015), p. 1013.

[176] Y. Li et al. "Unidirectional acoustic transmission through a prism with near-zero refractive index". In: *Appl. Phys. Lett.* 103 (2013), p. 053505.

[177] R. Al Jahdali and Y. Wu. "High transmission acoustic focusing by impedance-matched acoustic meta-surfaces". In: *Appl. Phys. Lett.* 108 (2016), p. 031902.

[178] S. Qi, Y. Li, and B. Assouar. "Acoustic Focusing and Energy Confinement Based on Multilateral Metasurfaces". In: *Phys. Rev. Applied* 7 (2017), p. 054006.

[179] S. Qi and B. Assouar. "Acoustic energy harvesting based on multilateral metasurfaces". In: *Appl. Phys. Lett.* 111 (2017), p. 243506.

[180] B. Xie et al. "Coding acoustic metasurfaces". In: *Adv. Mater.* 29 (2017).

[181] S. Qi and B Assouar. "Ultrathin acoustic metasurfaces for reflective wave focusing". In: *J. Appl. Phys.* 123 (2018), p. 234501.

Autobiography

My name is Shuibao (Steven) Qi, and I was born in Feb. 1986 in Hubei, China. I commenced my academic career as a master student in Sep. 2009 at Nanjing University, where my research topic was ultrasound cavitation and sonoluminescence. I got my Mater's degree in Jun. 2012, and after that I entered into industries. Three years's later, I quitted my job in China and went to France to pursue my PhD degree. From Oct. 2015 to present, my research directions and interest have involved acoustic metamaterials and metasurfaces for wave manipulations and energy harvesting. The acquired research results during my PhD career in the form of papers, conferences and posters are listed below.

Publications

Journal paper

1. Shuibao Qi, and Badreddine Assouar. " Ultrathin Acoustic Metasurfaces for Reflective Wave Focusing." *J. Appl. Phys.*, 123 (2018): 234501
2. Shuibao Qi, and Badreddine Assouar. "Acoustic energy harvesting based on multilateral metasurfaces." *Appl. Phys. Lett.*, 111 (2017): 243506.
3. Shuibao Qi, Yong Li, and Badreddine Assouar. "Acoustic Focusing and Energy Confinement Based on Multilateral Metasurfaces." *Phys. Rev. Applied*, 7 (2017): 054006. Highlighted by Physics Buzz.
4. Shuibao Qi, Badreddine Assouar and Weizhong Chen. "Effects of bovine serum albumin on a single cavitation bubble." *Ultrason. Sonochem.*, 38 (2017): 473.
5. Shuibao Qi, Mourad Oudich, Yong Li, and Badreddine Assouar. "Acoustic energy harvesting based on a planar acoustic metamaterial." *Appl. Phys. Lett.*, 108 (2016): 263501.
6. Oh Joo Hwan, Shuibao Qi, Yoon Young Kim, and Badreddine Assouar. "Elastic Metamaterial Insulator for Broadband Low-Frequency Flexural

Vibration Shielding." *Phys. Rev. Applied*, 5 (2017): 054034.

7. Li Yong, Shuibao Qi, and Badreddine Assouar. "Theory of metascreen-based acoustic passive phased array." *N. J. Phys.*, 18 (2016): 043024.

Conference proceedings

1. Shuibao Qi, Yong Li, and Badreddine Assouar. "Acoustic Energy Harvesting with Acoustic Metamaterials and Metasurfaces" *PHONONICS 2017*: 4th International Conference on Phononic Crystals/Metamaterials, Phonon Transport/Coupling and Topological Phononics, 171 (2017).

2. Badreddine Assouar and Shuibao Qi. "Acoustic Metasurfaces for Energy Harvesting." *Bulletin of the American Physical Society* (2018).

3. Badreddine Assouar, Shuibao Qi, and Yong Li. "Acoustic metamaterials and metasurfaces: a transformative approach for phononic insulators and energy harvesting." *Quantum Sensing and Nano Electronics and Photonics XIV*, 10111 (2017):101112B. International Society for Optics and Photonics.

Oral presentations

1. Badreddine Assouar, Shuibao Qi, and Yong Li. "Metamaterials and Metasurfaces for Acoustic Energy Harvesting", *IUTAM Symposium on Acoustic/elastic Metamaterials, Their Design and Applications.* Beijing, China (2018). (Invited)

2. Badreddine Assouar, Shuibao Qi, and Yong Li. "Acoustic metamaterials and metasurfaces: a transformative approach for phononic insulators and energy harvesting." *SPIE Photonics West* San Francisco, USA (2017). (Invited)

3. Badreddine Assouar, Shuibao Qi, Yong Li, and Joo Hwan Oh. "Acoustic Energy Harvesting Based on Metamaterials and Metasurface." *META 2017*, Incheon, South Korea (2017). (Invited)

4. Badreddine Assouar, Yong Li, Shuibao Qi, and Joo Hwan Oh. "Acoustic metamaterials and metasurfaces for sound isolation and acoustic energy harvesting." *2017 Chinese-French Workshop on Phononic Crystals and Metamaterials*, Beijing, China (2017). (Invited)

5. Badreddine Assouar, Yong Li, and Shuibao Qi. "Metamaterials for Vibration/Sound Isolation and Energy Harvesting." *International Workshop on Elastic Metamaterials*, Seoul, South Korea (2016). (Invited)

Appendix A

Additional documents

A.1 Equivalent circuit parameters

	Electrical	**Mechanical**	**Acoustical**
Effort	Voltage, V	Force, F	Pressure, P
Flow	Current	Velocity	Volume velocity
	$I = \mathrm{d}q/\mathrm{d}t$	$v = \mathrm{d}x/\mathrm{d}t$	$Q = \Delta V_{\mathrm{v}}/\mathrm{d}t$
Power	$W_{\mathrm{e}} = VI$	$W_{\mathrm{m}} = Fv$	$W_{\mathrm{a}} = PQ$
Impedance	$Z_{\mathrm{e}} = V/I$	$Z_{\mathrm{m}} = F/v$	$Z_a = P/Q$
Compliance	Capacitance	Mechanical compliance	Acoustic compliance
	$C_{\mathrm{e}} = \int I\mathrm{d}t/V = q/V$	$C_{\mathrm{m}} = \int v\mathrm{d}t/F = 1/k$	$C_{\mathrm{a}} = \int Q\mathrm{d}t/P = \Delta V_{\mathrm{v}}/P$
Resistance	Resistance	Damping	Acoustic resistance
	$R_{\mathrm{e}} = \mathrm{Re}(V/I)$	$d = \mathrm{Re}(F/v)$	$R_{\mathrm{a}} = \mathrm{Re}(P/Q)$
Kinetic energy	Inductance (H)	Mass (kg)	Acoustic mass ($\mathrm{kg/m^4}$)
Potential energy	Capacitance (F)	Compliance (m/N)	Acoustic compliance ($\mathrm{m^3/Pa}$)
Dissipation	Resistance (Ω)	Damping (m·s)	Acoustic resistance ($\mathrm{m^4{\cdot}s}$)

Table A.1 – Equivalent circuit parameters[37].

A.2 Electrical power outputs of various AEH systems

Type	Device sizes (cm^3)	SPL(dB)	Frequency (kHz)	Power(W)	Power density (W/cm^3)
PE[a]	2.445	149	13.57	6×10^{-12}	2.94×10^{-12}
	-	100	24	11×10^{-12}	-
	735.7	100	1.36	7.5×10^{-6}	10.2×10^{-9}
	-	100	16.7	140×10^{-12}	-
	2.47	161	2.64	30×10^{-3}	14.48×10^{-3}
	-	100	4.92	52.8×10^{-12}	-
	-	100	4.92	42.5×10^{-12}	-
	-	100	4.92	82.8×10^{-12}	-
	-	110	6.28	0.68×10^{-12}	-
	1500	110	0.146	2.2×10^{-6}	1.5×10^{-9}
	840	110	0.199	12.69×10^{-3}	15.12×10^{-6}
	900	100	0.242	55×10^{-3}	61.11×10^{-9}
	0.0055	100	3.5	1.69×10^{-9}	3.6×10^{-10}
	47.15	45	4.2	40×10^{-9}	8.48×10^{-10}
	3972	100	0.201	1.43×10^{-3}	0.36×10^{-6}
EM[b]	14.73	125	0.143	1.96×10^{-3}	1.336×10^{-4}
	7.86	120	0.144	1.5×10^{-3}	1.91×10^{-3}

Table A.2 – Comparison of the reported AEH systems[135].

[a] Piezoelectrical methods.
[b] Electromagnetic methods.

A.3 Arbitrary sound focusing with metasurfaces

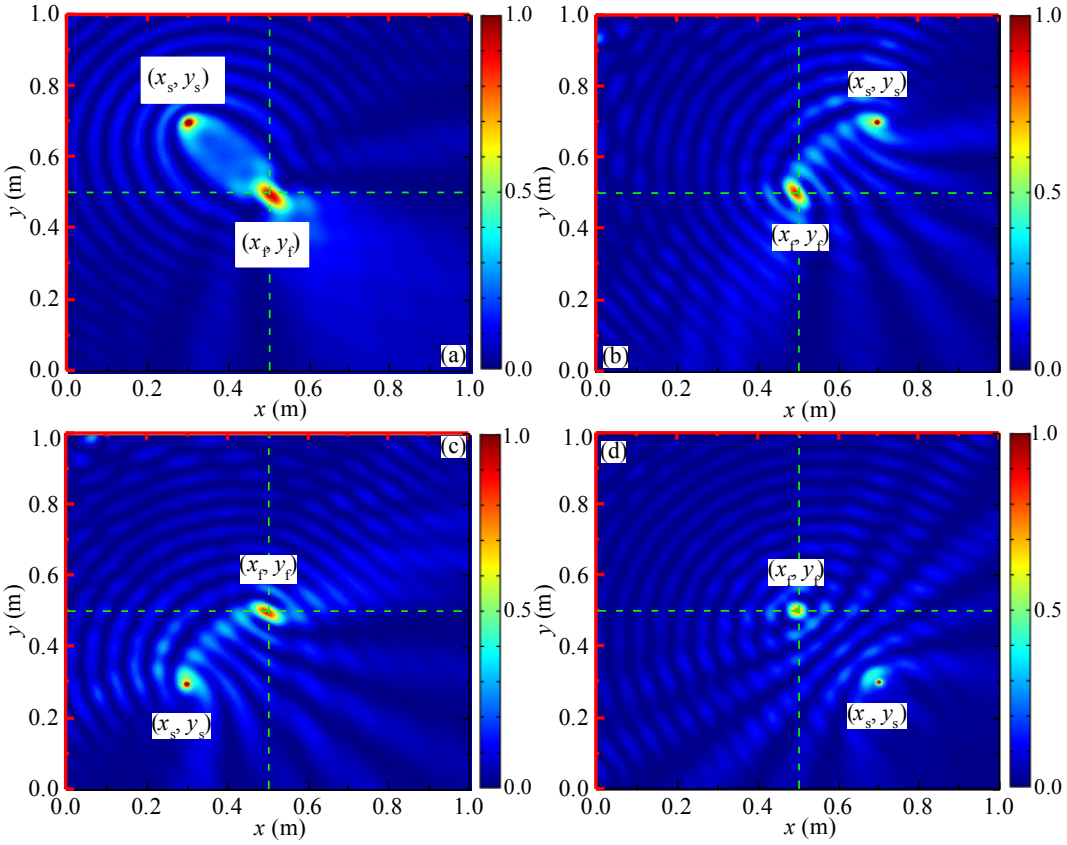

Figure A.1 – Reflected intensity fields under four various source positions. The focusing position is centered at (0.5 m, 0.5 m), and four source positions (a)-(d) are set at (0.3 m, 0.7 m), (0.7 m, 0.7 m), (0.3 m, 0.3 m) and (0.7 m, 0.3 m), respectively.

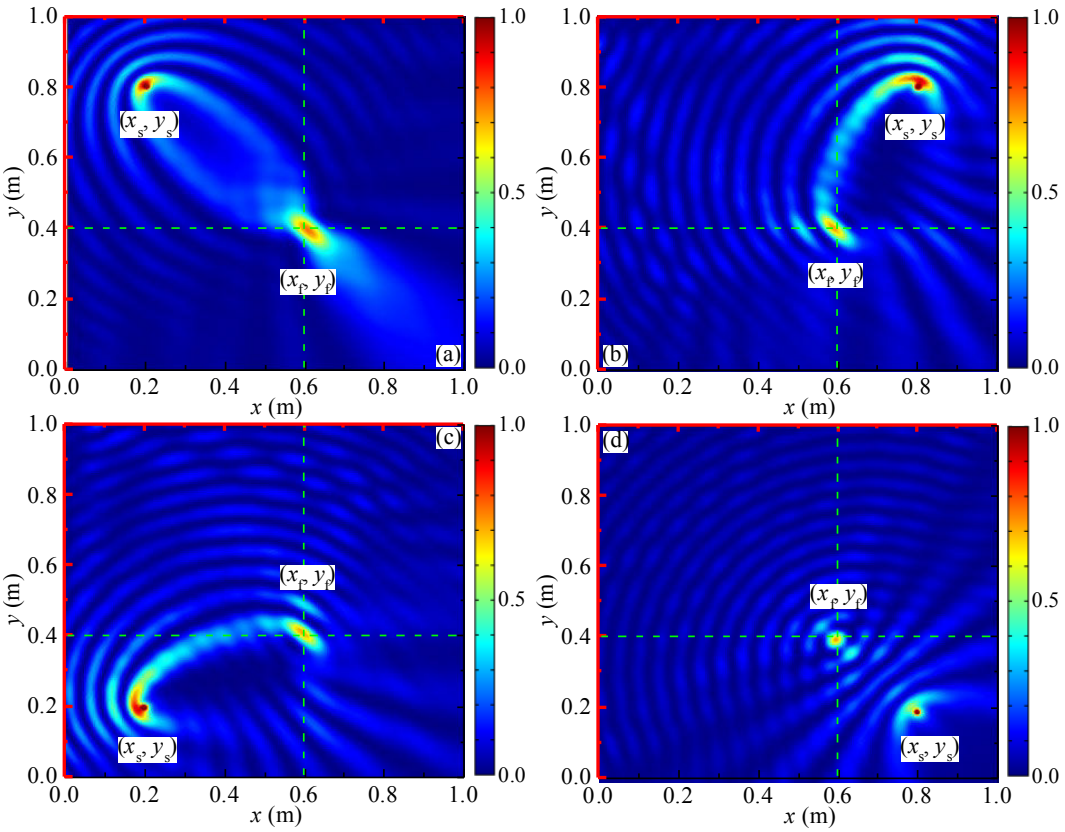

Figure A.2 – Reflected intensity fields under another four various source positions. The focusing position is centered at (0.5 m, 0.5 m), and four source positions (a)-(d) are set at (0.2 m, 0.8 m), (0.8 m, 0.2 m), (0.2 m, 0.2 m) and (0.8 m, 0.2 m), respectively.

A.4 Sound attenuation and absorption from viscosity and thermal conduction

The well-known nonlinear Navier-Stokes equation could be applied to describe the viscosity effect in sound attenuation[37]:

$$\rho\left[\frac{\partial \mathbf{u}}{\partial t} + (\mathbf{u}\cdot\nabla)\mathbf{u}\right] = -\nabla p + (\frac{4}{3}\eta + \eta_B)\nabla(\nabla\cdot\mathbf{u}) - \eta\nabla\times\nabla\times\mathbf{u}, \tag{A.1}$$

where η and η_{B} are the shear and bulk viscosity coefficients, respectively, and the term $\eta\nabla\times\nabla\times\mathbf{u}$ represents dissipation of acoustic energy caused by turbulence, laminar flow, vorticity, etc. Consider the adiabatic process and linear situation, the lossy wave equation yields the following form:

$$\left(1+\tau_{\mathrm{s}}\frac{\partial}{\partial t}\nabla^2 p\right)=\frac{1}{c^2}\frac{\partial^2 p}{\partial t^2} \tag{A.2}$$
$$\tau_s=\left(\frac{4}{3}\eta+\eta_B\right)\Big/\rho c^2$$

where $c=(\sqrt{\partial P/\partial\rho})_{ad}$ is the thermodynamic speed of sound, and τ_s is a relaxation time. For a monofrequency motion, the absorption coefficient α_{s} and phase velocity c_{p} give:

$$\alpha_{\mathrm{s}}=\frac{\omega}{c}\frac{1}{\sqrt{2}}\left[\frac{\sqrt{1+(\omega\tau_{\mathrm{s}})^2}-1}{1+(\omega\tau_{\mathrm{s}})^2}\right]^{1/2} \tag{A.3}$$
$$c_{\mathrm{p}}=\frac{\omega}{k}=c\sqrt{2}\left[\frac{1+(\omega\tau_{\mathrm{s}})^2-1}{\sqrt{1+(\omega\tau_{\mathrm{s}})^2}+1}\right]$$

Consider plane wave in $+x$ direction, the pressure can be expressed as,

$$\mathbf{p}=p_0e^{j(\omega t)}=p_0e^{-\alpha_s x}e^{j(\omega t-kx)} \tag{A.4}$$

The concept of complex sound speed should be applied to elucidate the absorption mechanisms. Combine the linearized Euler's equation and continuity equation, we can get a lossy Helmholtz equation with a damping term as below,

$$\nabla^2\mathbf{p}+\mathbf{k}^2\mathbf{p}=0 \tag{A.5}$$
$$\mathbf{k}=k-j\alpha=\omega/c$$
$$\mathbf{p}=p_0e^{\alpha x}e^{j(\omega t-kx)}$$

The specific acoustic impedance of the wave can be expressed as,

$$\mathbf{z}=\mathbf{p}/\mathbf{u}=\rho_0c_p/(1-j\alpha/k) \tag{A.6}$$

In addition to the viscosity effect, the thermal conduction is another mechanism for sound absorption. The change in thermal energy can be related with the change in temperature as

$$\frac{\Delta q}{\Delta t} = c_p \rho_0 \frac{\partial T}{\partial t} \tag{A.7}$$

where c_p is the specific heat at constant pressure and Δq is the gain in thermal energy of a unit volume of gas. The diffusion process for temperature can be written as

$$\frac{\partial T}{\partial t} = \frac{\kappa}{c_p \rho_0} \nabla^2 T \tag{A.8}$$

where κ is the thermal conductivity. Considering the fluid loss, we can obtain

$$\nabla^2 T = \frac{1}{T} \nabla T \cdot \nabla T + T \nabla \cdot \left(\frac{1}{T} \nabla T \right) \tag{A.9}$$

The time-averaged acoustic energy density variation can be expressed as

$$\frac{\mathrm{d}q}{\mathrm{d}t} = -\frac{1}{V} \left\langle \int_V \frac{\Delta q}{\Delta t} \mathrm{d}V \right\rangle_t = -\frac{\kappa}{T_{eq}} \frac{1}{V} \left\langle \int_V \nabla T \cdot \nabla T \mathrm{d}V \right\rangle_t \tag{A.10}$$

The absorption coefficient can be obtained from $\mathrm{d}q/\mathrm{d}t/q = -2\alpha_\kappa c$, and we have $q = p^2/2\rho_0 c^2$. With these terms, we could get the absorption of the thermal conduction as below

$$\alpha_\kappa = \frac{\omega^2}{2\rho_0 c^3} \frac{(\gamma - 1)\kappa}{c_p} \tag{A.11}$$

The amount of absorption depends on the deviation between adiabatic and isothermal conditions, i.e., $(\gamma - 1)$ as shown in Eq. A.11. Through considering thermal conduction and viscosity, sound attenuation and absorption in unideal fluids could be theoretically predicted by these equations.

Appendix B

MATLAB programmes

Listing B.1 – MATLAB code for the mapping of focusing area.

```
clear; clc; tic;

model = mphopen('COMSOL_filename'); % Open the COMSOL model.

n=1;
m=0;
x_f=linspace(0.1,0.9,100); % Scan of focusing coordinate x
y_f=linspace(0.1,0.9,100); % Scan of focusing coordinate y
Data=[];
 for i=1:length(x_f)
     for j=1:length(y_f)
         m=m+1;
       fprintf('Solving_for_P_point/Total_Point_%d/%d...\n',
       m,length(x_f)*length(y_f));
       model.param.set('x_f', y_f(i));
       model.param.set('y_f', y_f(j));
       model.sol('sol1').runAll;

coord = [x_f(i); y_f(j)]; % Scan of the focusing area.
p(n) = mphinterp(model,'p','coord',coord);
Data=[Data; x_f(i), y_f(j), p(n)];
n=n+1;
      end
 end
Data_real=real(Data);
```

```
Data_imag=imag(Data(:,3));
Data_Total=[Data_real Data_imag];

Amplitude=abs(Data); % The magnitude of the sound pressure.

save('Filename1.dat', 'Amplitude', '-ascii');
save('Filename2.dat','Data_Total','-ascii');
X = reshape(Amplitude(:,1)*Amplitude(:,1),[],length(x_f));
Y = reshape(Amplitude(:,2)*Amplitude(:,2),[],length(x_f));
Z = reshape(Amplitude(:,3)*Amplitude(:,3),[],length(x_f));
Fig_Intensity=surface(X,Y,Z);
```

Listing B.2 – Theoretical 3D phase distributions

```
clear all
clc
lbd=343/3430;
f=3430;
k=2*pi*f/343;
%  y=[lbd/8:lbd/8:0.3];
%  z=[lbd/8:lbd/8:0.3];
[y,z] = meshgrid(lbd/8:lbd/8:0.3);
flx=0.1;
fly=0.16;
flz=0.14;
phi=mod(k*(sqrt((fly-y).^2+flx.^2+(z-flz).^2)-flx)/2/pi,1);
% y(:,1)=lbd/8,lbd/8,... z(:,1)=lbd/8,lbd/4,...
% phi(y,z)
%
% for m=1:24
%     for n=1:24
%     if phi(m,n)>=11/12||phi(m,n)<1/12
%               phi(m,n)=1;
%     elseif phi(m,n)>=1/12&&phi(m,n)<1/4
%               phi(m,n)=2;
%     elseif phi(m,n)>=1/4&&phi(m,n)<5/12
%               phi(m,n)=3;
%     elseif phi(m,n)>=5/12&&phi(m,n)<7/12
%         phi(m,n)=4;
%     elseif phi(m,n)>=7/12&&phi(m,n)<3/4
%         phi(m,n)=5;
%     elseif phi(m,n)>=3/4&&phi(m,n)<11/12
```

```
%          phi(m,n)=6;
%      end
%
%      end
% end

for m=1:24
    for n=1:24
    if phi(m,n)>=1.875/2||phi(m,n)<0.0625
              phi(m,n)=1;
    elseif phi(m,n)>=0.0625&&phi(m,n)<0.1875
              phi(m,n)=2;
    elseif phi(m,n)>=0.1875&&phi(m,n)<0.625/2
              phi(m,n)=3;
    elseif phi(m,n)>=0.625/2&&phi(m,n)<0.875/2
        phi(m,n)=4;
    elseif phi(m,n)>=0.875/2&&phi(m,n)<1.125/2
        phi(m,n)=5;
    elseif phi(m,n)>=1.125/2&&phi(m,n)<1.375/2
        phi(m,n)=6;
    elseif phi(m,n)>=1.375/2&&phi(m,n)<1.625/2
        phi(m,n)=7;
    elseif phi(m,n)>=1.625/2&&phi(m,n)<1.875/2
        phi(m,n)=8;
    end

    end
end
figure
M=surface(y,z,phi);
set(M,'edgecolor','none')
save('Phi_yz.txt','phi','-ascii');
save('y.txt','y','-ascii');
% X=reshape(Amplitude(:,1),[],length(flx));
% Y=reshape(Amplitude(:,2),[],length(flx));
% Z=reshape(Amplitude(:,3),[],length(flx));
```

Acoustic Metamaterials and Metasurfaces for Energy Harvesting

Abstract

Phononic crystals (PCs) and acoustic metamaterials (AMMs), well-known as artificially engineered materials, demonstrate anomalous properties and fascinating capabilities in various kinds of wave manipulations, which have breached the classical barriers and significantly broaden the horizon of the whole acoustics field. As a novel category of AMMs, acoustic metasurfaces share the functionalities of AMMs in exotic yet compelling wave tailoring. Inspired by these extraordinary capabilities, innovative concepts of scavenging acoustic energy with AMMs are primarily conceived and sufficiently explored in this thesis. Generally, a planar AMM acoustic energy harvesting (AEH) system and acoustic metasurfaces AEH systems are theoretically and numerically proposed and analyzed in this dissertation. At first, taking advantage of the properties of band gap and wave localization of defect mode, the AEH system based on planar AMM composed of a defected AMM and a structured piezoelectric material has been proposed and sufficiently analyzed. Secondly, subwavelength ($\lambda/8$) and ultrathin ($\lambda/15$) metasurfaces with various lateral configurations, composed of labyrinthine and Helmholtz-like elements, respectively, are designed and analyzed to effectively realize the acoustic focusing and AEH. This thesis provides new paradigms of AEH with AMMs and acoustic metasurfaces, which would contribute to the industries of micro electronic devices and noise abatement as well.

Keywords: acoustic metamaterial, energy harvesting, acoustic waves, piezoelectric materials, acoustic metasurfaces

---

Métamatériaux et Métasurfaces Acoustiques pour la Collecte d'Energie

Résumé

Artificiels structurés, présentent des propriétés inédites et des aptitudes uniques pour la manipulation d'ondes en général. L'avènement de ces nouveaux matériaux a permis de dépasser les limites classiques dans tout le domaine de l'acoustique-physique, et d'élargir l'horizon des recherches fondamentales. Plus récemment, une nouvelle classe de structures artificielles, les métasurfaces acoustiques, présentant une valeur ajoutée par rapport aux métamatériaux, avec des avantages en termes de flexibilité, de finesse et de légèreté de structures, a émergé. Inspirés par ces propriétés et fonctionnalités sans précédent, des concepts innovants pour la collecte d'énergie acoustique avec ces deux types de structures artificielles ont été réalisés dans le cadre de cette thèse. Tout d'abord, nous avons développé un concept à base d'un métamatériau en plaque en se basant sur le de l'approche de bande interdite et des modes de défaut permis par le mécanisme de Bragg. Dans la deuxième partie de cette thèse, des métasurfaces d'épaisseur sublongueur d'onde et ultra-minces composées d'unités labyrinthiques ou de résonateurs de Helmholtz ont été conçues et étudiées pour s'atteler à la focalisation et au confinement de l'énergie acoustique. Cette thèse propose un nouveau paradigme de collecte d'énergie des ondes acoustiques à base des métamatériaux et métasurfaces. La collecte de cette énergie acoustique renouvelable, très abondante et actuellement perdue, pourrait particulièrement être utile pour l'industrie de l'aéronautique, de l'automobile, du spatial, de l'urbanisme.

Mots clés : métamatériaux acoustique, la collecte d'energie, ondes acoustiques, matériaux piézoélectriques, métasurfaces acoustiques

---

Institut Jean Lamour
Campus Artem, 2 allée André Guinier – BP: 50840 – 54011, Nancy Cedex – France

Résumé

Les métamatériaux acoustiques, connus depuis une quinzaine d'années comme matériaux artificiels structurés, présentent des propriétés inédites et des aptitudes uniques pour la manipulation d'ondes en général.

L'avènement de ces nouveaux matériaux a permis de dépasser les limites classiques dans tout le domaine de l'acoustique-physique, et d'élargir l'horizon des recherches fondamentales et appliquées à la frontière émergente entre de la recherche et l'innovation.

Plus récemment, une nouvelle classe de structures artificielles, les métasurfaces acoustiques, présentant une valeur ajoutée par rapport aux métamatériaux, avec des avantages en termes de flexibilité, de finesse et de légèreté de structures, a émergé.

Ces métasurfaces présentent de propriétés encore plus avantageuses en termes de manipulation contrôlée de la propagation d'ondes et d'applications nouvelles associées. Inspirés par ces propriétés et fonctionnalités sans précédent, des concepts innovants pour la collecte d'énergie acoustique avec ces deux types de structures

artificielles ont été réalisés dans le cadre de cette thèse.

Tout d'abord, nous avons développé un concept à base d'un métamatériau en plaque en se basant sur le de l'approche de bande interdite et des modes de défaut permis par le mécanisme de Bragg.

Un système de collecte d'énergie composé d'un métamatériau présentant un défaut de structure muni d'un matériau piézoélectrique structuré a été étudié et discuté. Le système proposé présente l'avantage de produire une densité de puissance élevée, d'voir un dimensionnement

réduit à des fréquences relativement basses, de simplicité de fabrication, et peut dans certains cas simultanément opérer comme barrière acoustique et collecteur d'énergie.

Dans la deuxième partie de cette thèse, des métasurfaces d'épaisseur sub-longueur d'onde et ultra-minces composées d'unités labyrinthiques (concept d'enroulement d'espace) ou de résonateurs de Helmholtz ont été conçues et étudiées pour s'atteler à la focalisation et au confinement de l'énergie acoustique.

Les études et analyses théoriques et numériques ont permis de valider la

pertinence de ces concepts et approches à base de métasurfaces, et de démontrer le grand potentiel de ces structures artificielles ultra-minces pour la focalisation, le confinement et la collecte d'énergie acoustique.

Cette thèse propose un nouveau paradigme de collecte d'énergie des ondes acoustiques (le son, le bruit …) à base des métamatériaux et métasurfaces. La collecte de cette énergie acoustique renouvelable, très abondante et actuellement perdue, pourrait particulièrement être utile pour l'industrie de l'aéronautique, de l'automobile, du spatial, de l'urbanisme …